Ultracold Atom-Atom Scattering with R-Matrix Methods

Tom Rivlin

A dissertation submitted in partial fulfillment
of the requirements for the degree of
Doctor of Philosophy
of
University College London.

Department of Physics & Astronomy
University College London

December 19, 2019

I, Tom Rivlin, confirm that the work presented in this thesis is my own. Where information has been derived from other sources, I confirm that this has been indicated in the work.

Complete list of publications

1. **T. Rivlin** and L. Lodi and S. N. Yurchenko and J. Tennyson and R. J. Le Roy (2015); ExoMol molecular line lists–X. The spectrum of sodium hydride, MNRAS. 451, 634-638, 10.1093/mnras/stv979
2. J. Tennyson and S. N. Yurchenko and Al-A. F. Refaie and E. J. Barton and K. L. Chubb and P. A. Coles and S. Diamantopoulou and M. N. Gorman and C. Hill and A. Z. Lam and others (2016); The ExoMol database: molecular line lists for exoplanet and other hot atmospheres, J. Mol. Spectrosc. 327, 73-94, 10.1016/j.jms.2016.05.002
3. J. Tennyson and L. K. McKemmish and **T. Rivlin** (2016); Low temperature chemistry using the R-matrix method, Faraday Discuss. 195, 31-48, 10.1039/c6fd00110f
4. R. L. Coates and A. Kuhai and L. Z. J. Turlej and **T. Rivlin** and L. K. McKemmish (2017); Phys FilmMakers: teaching science students how to make YouTube-style videos, European Journal of Physics. 39, 015706, 10.1088/1361-6404/aa93bc
5. C. Sousa-Silva and L. K. McKemmish and K. L. Chubb and M. N. Gorman and J. S. Baker and E. J. Barton and **T. Rivlin** and J. Tennyson (2018); Original Research By Young Twinkle Students (ORBYTS): when can students start performing original research?, Phys. Educ. 53, 015020, 10.1088/1361-6552/aa8f2a/meta
6. **T. Rivlin** and L. K. McKemmish and J. Tennyson (2019); Low-Temperature Scattering with the R-Matrix Method: The Morse Potential. In: Deshmukh P., Krishnakumar E., Fritzsche S., Krishnamurthy M., Majumder S. (eds) Quantum Collisions and Confinement of Atomic and Molecular Species, and Photons. Springer Proceedings in Physics, vol 230. Springer, Singapore, 10.1007/978-981-13-9969-5_25
7. **T. Rivlin** and L. K. McKemmish and K. E. Spinlove and J. Tennyson (2019); Low-temperature scattering with the R-matrix method: argon-argon scattering, Mol. Phys. 117(21), 3158-3170, 10.1080/00268976.2019.1615143

List of associated publications

Chapter 1, Chapter 2, Chapter 3:

- J. Tennyson and L. K. McKemmish and **T. Rivlin** (2016); Low temperature chemistry using the R-matrix method, Faraday Discuss. 195, 31-48, 10.1039/c6fd00110f
- **T. Rivlin** and L. K. McKemmish and J. Tennyson (2019); Low-Temperature Scattering with the R-Matrix Method: The Morse Potential. In: Deshmukh P., Krishnakumar E., Fritzsche S., Krishnamurthy M., Majumder S. (eds) Quantum Collisions and Confinement of Atomic and Molecular Species, and Photons. Springer Proceedings in Physics, vol 230. Springer, Singapore, 10.1007/978-981-13-9969-5_25
- **T. Rivlin** and L. K. McKemmish and K. E. Spinlove and J. Tennyson (2019); Low-temperature scattering with the R-matrix method: argon-argon scattering, Mol. Phys. 117(21), 3158-3170, 10.1080/00268976.2019.1615143

Chapter 4:

- **T. Rivlin** and L. K. McKemmish and J. Tennyson (2019); Low-Temperature Scattering with the R-Matrix Method: The Morse Potential. In: Deshmukh P., Krishnakumar E., Fritzsche S., Krishnamurthy M., Majumder S. (eds) Quantum Collisions and Confinement of Atomic and Molecular Species, and Photons. Springer Proceedings in Physics, vol 230. Springer, Singapore, 10.1007/978-981-13-9969-5_25

Chapter 5:

- **T. Rivlin** and L. K. McKemmish and K. E. Spinlove and J. Tennyson (2019); Low-temperature scattering with the R-matrix method: argon-argon scattering, Mol. Phys. 117(21), 3158-3170, 10.1080/00268976.2019.1615143

Abstract

Novel experimental methods have allowed for the routine production of ultracold (sub-Kelvin) atoms and small molecules. This has facilitated the study of chemical reactions involving only a small number of partial waves, allowing for unprecedented control over ultracold chemical reactions.

This thesis describes work towards a new set of theories, based on Wigner's R-matrix methodology, which are adapted for so-called heavy particle scattering, and in particular atom-atom scattering. From these new theories a new set of methods are constructed to accurately simulate scattering observables such as scattering lengths, cross-sections, and resonances for atom-atom scattering events at ultracold temperatures by producing high resolution plots of these observables.

The methods utilise software built for high-accuracy diatomic spectra, such as DUO, to provide molecular eigenenergies and wavefunctions of the bound system at short internuclear distances (in a region known as the inner region), only requiring as input a matrix of diatomic internuclear potential energy curves and couplings. These methods then act as 'harnesses', allowing this information to be used to perform an R-matrix propagation at long internuclear distances (in a region known as the outer region) using R-matrix propagation codes such as PFARM. The result of this propagation is then used to produce the aforementioned scattering observables.

In this work these new R-matrix methods are applied to the case of a particle scattering off a Morse potential, to elastic argon-argon collisions, and to the intra-multiplet mixing of oxygen when impacted by helium. This work also serves as a basis for the future simulation of more complex scattering events, such as atom-diatom collisions and higher polyatomic collisions.

Impact Statement

This research is the beginning of a new, long-term project, focused on the scattering of atoms and molecules at ultracold temperatures. Because this project has only recently begun, practical applications of the research are still only a long-term goal. The work presented here can be thought of as 'blue skies' research; whilst lacking in direct non-academic applications, future studies will rely on it.

This thesis has laid the groundwork for others to study more complex interactions using the methods developed here. In particular, two grants have already been awarded to researchers working on extensions of the code written for this work. Whilst this work focused on the one-dimensional problem of atom-atom collisions, two postdoctoral researchers have begun work on the next stage of the project since this work began: they have been developing the methodology required to produce results for the three-dimensional atom-diatom collision process.

The atom-diatom case is notable because by studying atom-diatom interactions, it is possible to study reactions where the species of molecule involved in the interaction can change. This represents a new contribution to the study of the physics of chemicals. Once the atom-diatom project is completed, not only will it be possible to explore reaction dynamics, but it will be possible to explore precise state-to-state reaction dynamics with high resolution and accuracy.

The work on atom-diatom reactions would not have been possible without the research presented here. There were unexpected mathematical, numerical, and physics-related issues that were discovered, and this work solved many of them in anticipation of the upcoming research on more complex systems.

Once the work on atom-diatom scattering is complete, it is possible to imagine that a general molecule-molecule scattering code could be constructed using these methods, and that this method will be effective at ultracold temperatures. This could be useful for the future study of more complex Bose-Einstein condensates, and for research into efficient and usable qubit designs in the field of quantum computing, where the low temperatures, small systems, and high accuracy that this project promises are all required.

Acknowledgements

I want to extend my thanks to a number of people who helped me with this thesis.

Professor Jonathan Tennyson was the best supervisor a student could ask for: patient, warm, always giving me time when I needed it, and of course infinitely knowledgeable. I cannot thank him enough for everything.

Also at UCL are two other people I worked very closely with: Dr. Laura McKemmish and Dr. Eryn Spinlove. Both of them helped me immensely with this work, and they deserve recognition for the brilliant academics they both are. The fact that they are also both great friends is just an added bonus.

There were many pieces of software created by other academics which I used in this work, and I am very grateful to the creators of those codes for the help they gave me. UCL's Professor Sergey Yurchenko was always available to answer any questions I had about his code whilst I made modifications to it. Peter Bingham, similarly, was very helpful in explaining how to use his code. And Dr. Martin Plummer not only helped me to use and modify his code, but also made many modifications to it himself at my request, and answered many of my queries about it, all of which I am very grateful for.

Many other academics also deserve recognition for the help they've given me in this work, including my second supervisor, Professor Simon Arridge, along with Professor David Manolopoulos, and the late, great Professor Robert J. Le Roy.

This project would also not have been possible without my wonderful colleagues in the ExoMol group, who were always there for a coffee (or something stronger) when I needed it. In particular I'd like to acknowledge and thank Barry, Victoria, and Tom, and my office mates Emil, Bridgette, and Tony, but of course all the people I've worked with at UCL, including the Chalkdust team and my kung fu friends, have been a pleasure to be around. Seriously, folks, thank you so much for making the last four years so fun.

My parents have been immensely supportive of my work, and I'm so grateful to them for just about everything. Mum, dad, I know you're both very proud of me and I appreciate that.

There are too many friends to give thanks to them all here, so to round things off I'll just list a few who are very special to me and whose names begin with A: my brother Adam, along with Amy, Angus, and Annina. Thank you and everyone else so, so much for everything.

Contents

List of Figures

List of Tables

Chapter 1

Introduction

1.1 Ultracold Physics and Chemistry

Cold and ultracold atoms and molecules have never been more accessible to working physicists [1], thanks to a variety of experimental techniques which make them easier than ever to produce [1, 2, 3], trap [4], and study [5, 6].

Laser cooling remains a cornerstone of the field of ultracold physics for the cooling of atoms, ions, and molecules [7, 8], and one of the most common ways to bring particles to ultracold temperatures. The 1997 Nobel Prize for its discovery also emphasised one particular type of laser cooling called ‘Sisyphus cooling’ [9, 10, 11], due to the way the atoms being cooled would be forced to roll up a potential ‘hill’ to drain it of kinetic energy, only to be pushed to the bottom of the hill to start the cycle again.

A variety of other cooling techniques exist, too. For instance, sympathetic cooling is a technique which allows one to cool particles by placing them in contact with other, already cooled particles. The utility of the method is due to the possibility of using one type of particle that is relatively simple to cool using standard laboratory techniques to cool down other particles that are more difficult to cool [12, 13, 14, 15].

Atoms and molecules that can be cooled can more easily be contained and trapped. The most common form of trapping involves different types of magnetic confinement [10, 4], which use magnetic fields, sometimes rotating magnetic fields, as barriers to prevent the particles escaping.

There are a number of reasons why these ultracold systems are useful to physicists and chemists. When in these ultracold states, the interactions between atoms and molecules can involve a very small number of quantum states, or possibly only a single state. To quote Stuhl *et al.* [1], this is "perhaps the most elementary study possible of scattering and reaction dynamics."

One consequence of these developments is that it is now possible to control invidual molecules (especially diatomic molecules) with high precision [16, 1], and, as a consequence, study in unprecedented detail the fundamentals of chemical reactions. Some examples of ultracold collisions and interactions that have been studied include two polar molecules in a one-dimensional harmonic trap, ultracold atoms colliding with trapped ions, and Coulomb crystals, which provide translationally cold, localised ions that can collide with molecules [17, 18, 19, 20, 21, 22, 23].

The possibility of controlling reactions with such a small number of states [24, 25] could pave the way to precise control of reaction rates [26] and improved efficiency of chemical reaction processes. This is due to the unique properties atoms and molecules have when cooled down to ultracold temperatures, but it is also due to the fact that there are fewer states the reactants can be in, making reactions easier to account for. Again quoting Stuhl *et al.* [1]: "colder is cleaner."

For a given system, the exact temperature that can be defined as 'ultracold' can vary, but it is usually when the scattering particles interact with a mutual scattering energy of the order of 10^{-6} to 10^{0} Kelvin. It is worth noting that the coldest naturally occurring places in the universe – parts of interstellar space – have temperatures of a few Kelvin [24].

In ultracold scattering, the particles themselves may have relatively high energy, but interesting ultracold phenomena are still observed when the translational kinetic energy between the particles is at an ultracold level. For example, merged molecular beam experiments involve molecules travelling alongside each other at speeds which are supersonic in the lab frame, but are only hundreds of millikelvin when measured relative to each other [27].

But even when just considering cooled and trapped particles, ultracold temperatures are increasingly easy to reach for a variety of physical systems in the modern physics lab, and many interesting experiments have been done on these types of system [24, 8, 6, 28].

The implications of this new paradigm are subtle but far-reaching. The ability to observe reactive scattering between small atoms and molecules in precisely defined states with minimal thermal noise is, in a sense, one of the most powerful tests possible of the fundamentals of the field of chemistry [1]. The vision of being able to perform a chemical reaction and precisely control the start and end quantum states of all the atoms involved is becoming increasingly possible in many circumstances [24].

As such, this emerging field of research is in need of a robust theoretical framework to assist with these experimental endeavours [24]. This work is designed to contribute to that need by providing a method for generating high-accuracy scattering observables for collisions involving two atoms, including low-energy cross-sections (excluding differential cross-sections) for both elastic and inelastic [19] collisions, and low-temperature observables such as scattering lengths and effective ranges.

The algorithm introduced in this work, known as **RmatReact**, is based on the R-matrix method, which is widely applied to electron-atom and electron-molecule collisions [29, 30], and which has here been adapted to the calculation of scattering observables in the atom-atom case.

These scattering observables describe non-reactive scattering processes: processes in which the chemical configuration of the reactants cannot be changed by the interaction. For the atom-atom collisions being studied here, it is only possible for the two atoms to have their quantum numbers (their ‘levels’ or ‘channels’) altered by the process. This work does not consider the possibility that the atoms remain bound after the collision, or that one or both atoms are ionised.

This work serves as an exploratory study in anticipation of more complex reactions, including atom-diatom collisions and beyond. In these cases, it will be

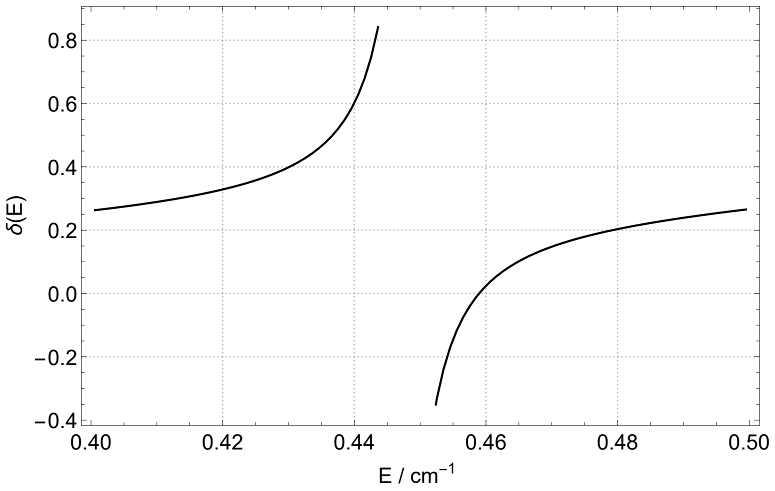

Figure 1.1: A typical plot of a resonance in the eigenphase $\delta(E)$ as a function of energy E (these quantities will be defined in Chapter 2).

possible to study [31] reactions of the type

$$A + BC \to AB + C. \tag{1.1}$$

This is known as *reactive scattering*, and it is arguably the simplest possible chemical reaction, right at the border between physics and chemistry. Eventually, it is hoped that it will be possible to study ultracold collisions between two polyatoms, each with an arbitrary number of atoms.

The key feature of ultracold collisions which make them useful for controlling reactions is the presence of resonances. These are features of the cross-section which arise in conjunction with a variety of physical phenomena, such as the presence of quasibound states with non-trivial lifetimes, or the coupling of closed channels with open ones. Resonances can affect the dynamics and scattering observables of the system at certain energies in quantifiable ways [32, 33]. These resonances tend to only be distinguishable at very low temperatures [34]. When they appear in plots of scattering observables such as the cross-section, resonances have a number of characteristic functional forms, such as the Breit-Wigner form [35, 30, 36], as seen in Figure 1.1, and the Fano profile [37]. This is discussed more in Section 2.1.4.

Figure 1.1 represents a resonance profile that could belong to a shape resonance. The profile appears discontinuous but is not – its supposed discontinuity is an artefact of the fact that the vertical axis is measured in radians between $-\frac{\pi}{2}$ and $\frac{\pi}{2}$ and the resonance increases the value of the quantity $\delta(E)$ by π.

These resonances are associated with quasibound energy levels, which are higher in energy than the asymptotic energy of an electronic state (see Figure 1.3), but lower in energy than the peak of the centrifugal barrier when $J > 0$ (not featured in Figure 1.3, which is a $J = 0$ state). As a consequence, particles occupying these energy levels can tunnel through the centrifugal barrier, and thus have finite lifetimes as bound states, hence the name ‘quasibound’. Similarly, shape resonances are so-called because they arise due to the shape of the effective electronic PEC for $J > 0$. These types of resonance appear in elastic and inelastic scattering cross-sections.

Other types of resonances also exist, such as Feshbach resonances [32, 33] (sometimes called Fano-Feshbach resonances [24]). These types of resonance are common in more complex systems, such as open-shell atoms interacting with other open-shell atoms. They can appear in systems like the ones studied here when a closed channel interferes with an open channel if those channels are still coupled by potential terms, and they can appear in elastic and inelastic cross-sections for open channels – those that lie below the scattering energy.

As with shape resonances, the physical origin of a Feshbach resonance is a quasibound state with a finite lifetime. In the case of Feshbach resonances, the state in question is one belonging to a closed channel. If a scattering event occurs with a scattering energy E relative to the threshold for one channel, but below the threshold for another channel, then under normal circumstances, the higher channel is considered closed and does not participate in the reaction. However, if the higher, closed channel supports a bound state with an energy close to the value of E, and if a coupling exists between the open and closed channels, then it is possible for mixing, even strong mixing, to occur between the open and closed channels [32].

This mixing results in the reactant being trapped in a quasibound state, which can be thought of as the state the reactant would have ended up in if the reaction ended with the two reactants being bound and if it could access the closed channel. The quasibound state leads to a corresponding resonance in scattering observables. Besides appearing in features in the eigenphase and cross-section, the scattering length is known to be large when affected by the resonance [32].

Of particular interest to this work are systems with deep potential wells which can support many bound states, where there may be many opportunities for novel physics to be uncovered [38]. One example of this is the RbCs system – a rubidium atom scattering off a caesium atom [39]. Systems such as this one are significant because it is likely that they support a large number of Feshbach resonances, but it is also worth noting that molecules in general can support many more Feshbach resonances than atoms can due to the large number of bound ro-vibrational states they have [34].

In fact, it has been shown that that ultracold atomic collisions can have an overwhelmingly large density of resonances when measured as a function of scattering energy [34]. A similar phenomenon has been observed in a hot system: the well-known, near-dissociation H_3^+ spectrum [40, 41, 42, 43].

In Mayle *et al.* [34], the density of resonances in the systems they simulated, which included RbCs colliding with RbCs, were so large that a statistical approach to the study of the resonances was appropriate, including the use of a density of states parameter. If one is not taking a statistical approach to the large density of resonances in these simulations as Mayle *et al.* did, then it is clear that a highly fine-grained approach to resonance finding is needed.

Manipulation of these resonances, especially Feshbach resonances, via electric and magnetic fields [20] is also a rich area of research. This is because it is possible to adjust the location of Feshbach energy levels using magnetic fields, making them more accessible for a larger number of systems [32, 24]. Taking advantage of resonance structure is just one example of the many ways that the manipulation of magnetic fields can be used in ultracold physics [44].

These techniques have already been used to help form ultracold molecules such as the aforementioned RbCs [17]. They offer some of the best opportunities available for quantum control and steering in these systems. Resonances are required for efficient magnetoassociation, but overlapping Feshbach resonances can cause complications in experiments that utilise them [45], meaning that a better understanding of these dense resonances is required.

The control these methods offer has already led to the experimental verification of novel physical effects [46, 47, 48, 49, 50, 51, 52, 53, 54, 55], including the strange Efimov trimers. This is an unusual quantum phenomenon with a 'Borromean'-like property where three identical bosons can bind together to form a trimer, even when each individual pair of particles has too weak a mutual interaction to bind to each other. A fascinating universal scaling law results from these systems, where increasing the length scale by a constant factor approximately equal to e^{π} results in two new Efimov states being found with approximately $e^{\pm\pi}$ times more binding energy – a process which can be repeated infinitely many times to produce infinitely many states.

Finally, a discussion of interesting quantum phenomena at cold temperatures would not be complete without mentioning the famous Bose-Einstein Condensate (BEC). As with laser cooling, ever since its Nobel Prize-winning discovery [56], it has been a field of research unto itself. BECs are typically formed at nanokelvin temperatures – even colder than the ones being considered here. At these temperatures the quantum system being studied can only be in one state: the ground state, and it has an assortment of strange, purely quantum properties as a result.

The connection between BECs and this work is that simulations of BECs rely on the scattering length, which this work is well-suited to producing [32, 57]. A better understanding of the scattering properties of ultracold systems may be useful for simulations and experiments involving the construction and manipulation of BECs.

1.2 Simulating Ultracold Systems

Theoretical studies of ultracold collisions require a different theoretical framework to room temperature or even cold collisions. In those cases, it is often preferable to use time-dependent methods, which explicitly model interactions occuring forwards in time via the time-dependent Schrödinger equation, and here literature around the theoretical methodology is fairly robust [58]. Part of the reason why these methods are known to fail at ultracold temperatures is that they are less able to handle resonances. Resonant states have finite lifetimes which are long relative to the interaction time, even though these ultracold collisions tend to themselves be slow on molecular time-scales, and which can be missed by a method that integrates over a finite amount of time.

By contrast, time-independent methods have no such difficulties, as they treat the problem with no time variable by solving the time-independent Schrödinger equation. Examples of such methods include the method proposed in this work, and a wide variety of coupled-channel methods, including Hutson's MOLSCAT method [59], and different hyperspherical methods [60, 61, 62], including those presented by Kendrick [63] and by Launay *et al.* [64].

All of these methods also tend to work more effectively with these ultracold systems due to the fact that they rely on a partial wave expansion. A partial wave expansion is a method by which a wavefunction with full 3D coordinate dependence is presented as a sum over 1D radial wavefunctions multiplied by angular terms [65, 66]. The sum is over individual 'partial waves', each of which has a different symmetry and set of quantum numbers. The concept is introduced rigorously in Chapter 2. At lower energies, fewer states, or partial waves, are energetically accessible, and hence fewer terms in the partial wave expansion are required to obtain accurate results.

The particular time-independent method proposed in this work is based on R-matrix methods. These methods are established standards for electron-atom and electron-molecule collisions at 'low temperatures' – so-called light particle scattering [30, 67, 29, 68] – where the energy is below the ionisation threshold of 10^5 K. This is, of course, much higher than the ultracold temperatures considered here, and so it is not guaranteed that the method will succeed in this temperature regime. The type of R-matrix algorithm proposed in this work has only been tested with atom-atom or atom-molecule collisions – so-called heavy particle scattering – in one exploratory study [69] (see Section 1.5).

The R-matrix method is similar in spirit to the multichannel quantum defect theory (MQDT) which has been extensively used to study ultracold atom-atom [70, 71, 72, 73], and atom-molecule collisions [74, 75, 76]. Both methods perform a short range calculation once and re-use the results of that calculation over a range of energies, and both methods consider the problem in two regions to leverage the difference in length and energy scales between the two regions. In fact, the treatment of the outer region in the two methods can be very similar. Furthermore, both methods can be used to simultaneously obtain information about the bound and scattering states of a system.

However, while MQDT approximates a full solution of the close-coupling equations by using quantum defects which only have a weak dependence on the collision energy, the R-matrix method aims to provide an exact solution to the close-coupling problem based on an inner region with no energy dependence.

1.3 Yes, but what exactly is an R-matrix?

The R-matrix in its original form was invented by Eugene Wigner and Leonard Eisenbud in the 1940s as an entirely quantum mechanical method for solving nuclear scattering problems [77, 78]. The method and its descendants are still used for nuclear problems today [79]. The initial impetus for the development of the method was the issue in nuclear scattering theory of not having a robust theory of the sources of potential energy in atomic nuclei. Without a good ansatz for the form these potential energy curves took, it was difficult to model interactions along these curves.

As such, the R-matrix method developed around the idea of *partitioning* space into an inner and outer region along the reaction coordinate(s), as outlined in Figure 1.2. The two regions could then be treated with different levels of approximation to obtain the scattering observables with the desired accuracy [30]. The two levels of approximation were both still within a quantum mechanical framework, with no

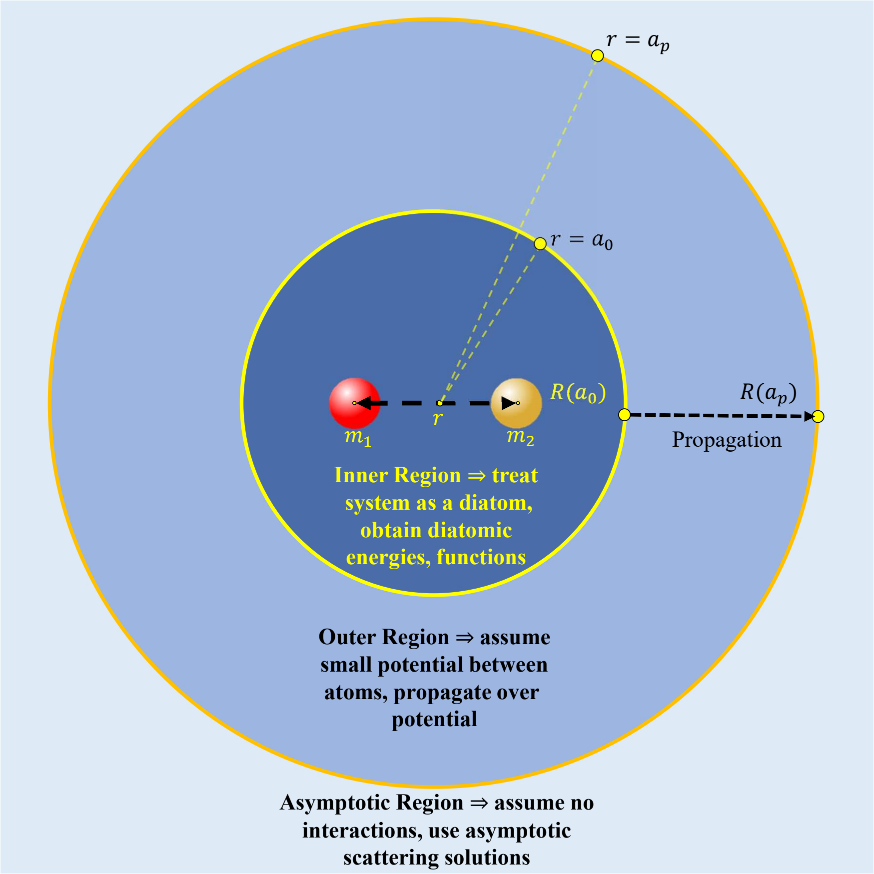

Figure 1.2: A schematic demonstrating how space is partitioned by the R-matrix method in the 1D, atom-atom collision being studied here. $R(r)$ is the single-channel R-matrix at distance r.

semiclassical approximations being made. This original approach can be thought of as a ‘Phenomenological’ R-Matrix Method, as it only involved simple approximations of the short-range physics that were not based on well-understood theory.

The concepts that arose from this partitioning method were then adapted to apply to other scattering problems. Here modern R-matrix theory is presented as applied to the one-dimensional case of two atoms colliding – the sole focus of this work – to illustrate the principle.

The inner region can be defined as the space in which the two nuclei of the atoms are within a certain internuclear separation of each other, $r \leq a_0$, as illustrated in Figure 1.2. Within the inner region, the two atoms are treated as a bound diatomic system in a specific electronic state via the Born-Oppenheimer approximation [80], which will have a form similar to that of Figure 1.3, and they are analysed in a

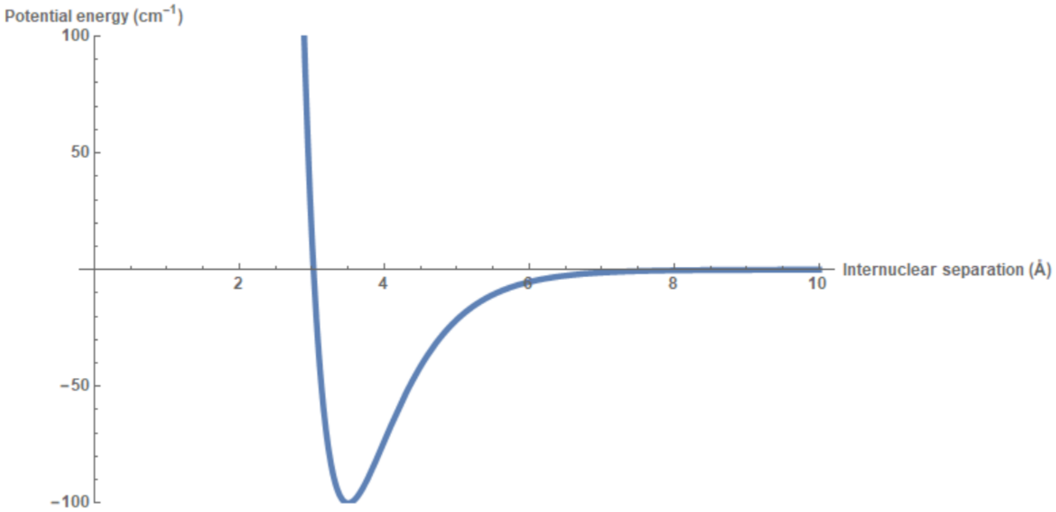

Figure 1.3: The typical form of the potential energy curve for a diatomic molecule with no centrifugal barrier along the coordinate of internuclear separation.

fully quantum mechanical framework, with the full complexity of their interactions considered, by solving the time-independent Schrödinger equation within a finite region for the bound system.

The result of this is a set of eigenenergies, E_i, and eigenfunctions, $\chi_i(r)$, describing the diatomic system in the inner region, with molecular quantum numbers describing energy levels and electronic states. This information is all used to construct the object known as the R-matrix on the boundary between the inner and outer regions. It is only at the construction of the R-matrix that the scattering energy is inserted into the problem.

In the outer region, by contrast, it is generally assumed that the long-range form of the potential between the two atoms is given by a polynomial in r^{-1}. This work does, however, deviate from this assumption by introducing an exponentially decaying outer-region potential for some calculations, and later chapters will discuss the implications of this. In either case, it is also assumed that a partial wave expansion of the appropriate functions with a small number of terms is sufficient to obtain accurate results.

The results of the inner region calculations combined with the scattering energy, in the form of the R-matrix, are used to construct the outer region problem. This problem is then solved by *propagating* the R-matrix from the boundary to some asymptotic distance by constructing an iteration equation over the space using the potential between the atoms.

The R-matrix on the boundary is the connection between the inner and outer regions because it can be defined in two ways: it can be defined both as the log-derivative of the asymptotic channel functions of the two scattering atoms in the outer region, and in terms of a sum over bound, diatomic, inner region wavefunctions and eigenenergies. For a single channel (elastic) scattering event involving only one partial wave, the two definitions take the form [30]:

$$\psi(a_0,E) = a_0 R(a_0,E) \left. \frac{d\psi(r,E)}{dr} \right|_{r=a_0}, \tag{1.2}$$

$$R(a_0,E) = \frac{\hbar^2}{2\mu a_0} \sum_{k=0}^{N} \frac{|\chi_k(a_0)|^2}{E_k - E}, \tag{1.3}$$

where $\psi(r,E)$ is the total scattering wavefunction for two atoms a distance r apart which are scattering off each other with relative energy E, a_0 is the position of the boundary between the inner and outer regions, μ is the reduced mass of the two atoms, the counting index k (not to be confused with the scattering wavenumber k, defined in the next chapter) counts over all of the bound and continuum states of the finite inner region diatomic system (up to some number, N), and $\chi_k(r)$ and E_k are the kth eigenfunction and eigenenergy of the inner region diatomic system respectively.

The two definitions essentially take the form of a log-derivative of a quantity associated with the outer region (Equation 1.2) and a sum (Equation 1.3) over quantities associated with the inner region. The equivalence of these two definitions [30] allows one to use information about the bound diatomic system to derive properties of the scattering event. This means one can avoid having to solve the two-body Schrödinger equation over all space.

The R-matrix formalism is naturally suited to the type of problem being studied here. There are fundamental differences between the short-range and long-range behaviours of the atoms as they interact: at short range the interaction is complex, and it merits a high-level of approximation to capture all of the physics involved. At long-range the interactions are simpler, yet a larger range of distances must be considered for the physics of the long-range interactions to be fully captured.

Treating the two regions differently is therefore sensible – little extra accuracy is to be gained by treating the long-range effects with the same level of approximation as the short-range ones, and a potentially very large increase in computational efficiency can be obtained from the way the long-range is handled by the R-matrix method.

1.4 This Work

As Equation 1.3 shows, construction of an accurate R-matrix is dependent on highly accurate solutions to the time-independent Schrödinger equation over a finite region for the inner region portion of the method. In order to obtain these solutions, nuclear motion programs designed for high resolution spectroscopy are utilised. Because this work relies on high-accuracy potential energy curves to describe the short-range physics of the scattering problem, it can be thought of as the 'Calculable' R-Matrix Method, in contrast to the Phenomenological version originally introduced by Wigner and Eisenbud.

It is not immediately apparent why a work dedicated to obtaining scattering observables for atom-atom interactions would need to dedicate so much effort to solving the Schrödinger equation for diatomic molecules, but that is exactly the case. In *A scattering theory of diatomic molecules: General formalism using the channel state representation* [81], F. H. Mies says that a "complete theory of diatomic molecules should be indistinguishable from a complete theory of atom-atom scattering." In the spirit of this idea, the next chapter will explain in more detail the connections between the two physical systems from a theoretical perspective.

There has been much progress in the field of accurate solutions to the Schrödinger equation for bound multi-atom systems over the years. For instance in water, which has a deep well and many bound states, there are high-accuracy line lists up to and beyond dissociation [82, 83, 84]. There have also been spectroscopic observations of resonances in water [84, 85].

The main focus for RmatReact so far has been on DUO [86], which is a code designed to obtain high-accuracy spectra for diatomic molecules, and in particular open-shell, coupled-state molecules [87]. Some of the work in this thesis was also completed using the similar but less general diatomic code LEVEL [88]. It is anticipated that similar codes for polyatomics, such as DVR3D [89], WAVR4 [90], and TROVE [91, 92] will be used for the equivalent scattering calculations in larger systems. For this work, DUO was modified to use a different basis set with boundary conditions more suited to this work, and to solve the surface term problem which arises in calculations of solutions to the Schrödinger equation over a finite region, as discussed in Chapter 3.

The outputs of the 'inner region' codes such as DUO were then input into a 'harness' code which constructed the R-matrix for a given set of scattering energies, and passed that R-matrix on to an 'outer region' code.

In the outer region, two different types of R-matrix propagation have been used in this work. In the single channel case, a simple propagator based on the work of Light and Walker [93] was implemented directly into the harness code, and the scattering observables obtained directly from that propagator. In the multichannel case, a version of an R-matrix propagation code for electron-atom collisions, PFARM (also known as PRMAT) [94], was used to propagate the R-matrix and produce the scattering observables.

PFARM is the parallelised version of the older code FARM: the Flexible Atomic R-Matrix package [95]. In this work, PFARM was modified to account for the differences between electron-atom scattering and atom-atom scattering. The scattering observables themselves were calculated using the harness code, and with the software reskit where appropriate.

The method presented here was tested against three different systems. First it was compared to analytic scattering results from the elastic scattering of a particle off a Morse potential. Next, it was used to obtain scattering lengths, effective ranges, and cross-sections of argon elastically scattering off argon at ultracold temperatures, with the intention of searching for shape resonances, and of using the results to shed light on an outstanding issue concerning the bound states of the Ar_2 dimer. Finally, inelastic scattering was introduced to explore cross-sections for intramultiplet mixing in oxygen due to ultracold interactions with helium atoms, and a selection rule governing these transitions was studied.

1.5 Other Works

With the exception of a single proof-of-principle study by Bocchetta and Gerratt [69], the methods developed here have not been applied to so-called heavy particle scattering before. There are also several significant differences between the study of Bocchetta and Gerratt and the method employed in this work. This is discussed in more detail in Chapter 3.

Bocchetta and Gerratt's work is unique because when heavy particle scattering is usually simulated using R-matrix methods, an alternate R-matrix method is used. This alternate method only uses the outer-region propagation part of the method [96, 93, 97]. As such, one can refer to these methods as Propagator-Based R-Matrix Methods, in contrast to the Calculable methods used here and by Bocchetta and Gerratt, and to the Phenomenological methods used by the progenitors of R-matrix theory.

In Propagator-Based methods, the boundary between the two regions is set to be close to zero internuclear separation. Since there is a large repulsive barrier in a typical diatomic potential energy curve – the classically forbidden region, as displayed in Figure 1.3 – this will mean that the diatomic wavefunctions, and by extension the R-matrix, will be close to zero, and so it is assumed to be zero. This R-matrix is then propagated from the boundary, through the outer region, over the potential energy curve to the asymptotic region.

This makes this technique especially useful for heavy-particle scattering, where there often is little resonance structure in the scattering observables, and thus not a large need to produce fine-grained plots of observables as a function of energy. Propagator-Based techniques have the advantage that they avoid the need for diagonalisation in the inner region. Since diagonalisation is usually an expensive process, any method which avoids the need for it has many built-in advantages.

It is anticipated, however, that the Calculable R-matrix methods presented in this work will be an improvement on the Propagator-Based studies for the systems being considered here, both in terms of computational expense and in the accuracy of the simulation. This is due to one key aspect of the algorithm. Specifically, Propagator-Based methods must repeat the entire calculation for every different scattering energy value one wishes to sample. Therefore they do not leverage the efficiency of variational nuclear motion programs at solving the Schrödinger equation at short range.

This is especially problematic if the potential is rapidly varying, as with, for instance the deep potential wells studied here. In those cases, the various propagator methods will need a large number of iterations in order to achieve accuracy. Having a large inner region alleviates this problem by handling most of the complicated physics of the close-range interactions in one diagonalisation (or a small number of diagonalisations) – the entire inner-region must only be calculated once, independent of scattering energy, and then the results can be re-used for any scattering energy.

This allows one to construct fine-grained plots of scattering observables such as the cross-section as a function of the scattering energy, allowing one to more easily detect resonant behaviour from these observables.

Other similar, non-R-matrix methods do exist to study the systems being studied here. Already mentioned is Hutson's MOLSCAT [59]. This uses coupled-channel methods to obtain cross-sections and other assorted scattering observables, including low-energy ones such as the scattering length and effective range, which this work places an emphasis on, too.

MOLSCAT's coupled-channel methods have much in common with the R-matrix methods discussed here: both are time-independent, both involve coupling potential energy curves together, both use partial wave expansions, both involve matching wavefunctions to asymptotic boundary conditions, and both involve propagating a quantity identified as a log-derivative of a wavefunction over an internuclear coordinate. Indeed, it is possible to use R-matrix propagation methods such as that due to Light and Walker in MOLSCAT, along with a number of other propagation methods.

One important difference between R-matrix methods and the coupled-channel methods of MOLSCAT is the presence of the scattering energy-independent inner region in the former (though as previously stated not all R-matrix methods use an inner region). In coupled-channel methods, by contrast, the entire calculation must be repeated for each scattering energy being considered, often at great computational expense.

It is worth noting that coupled-channel methods can be used to solve the types of problems presented in this thesis, and indeed MOLSCAT has been used to solve ultracold atom-atom and atom-diatom problems before [98, 99, 100]. Whilst this project treads well-established grounds, future versions of RmatReact are anticipated to be able to solve previously unsolved problems in the theory and simulation of ultracold molecular collisions.

For instance, another important difference between R-matrix and coupled-channel theory will be more apparent in future work on RmatReact, in that no matter the dimensionality of the system being studied, MOLSCAT only ever propagates over a single radial coordinate, and treats all other coordinates in the problem separately. This will not be the case in the atom-diatom versions of RmatReact in development (or indeed in versions of RmatReact for even larger systems). In fact, the chemistry that will be simulated in later RmatReact projects will even require coordinate transformations [31].

As with coupled-channel methods, the previously mentioned MQDT methods also have an ‘inner region’ of sorts, although propagation is still performed in the inner region in MQDT. These methods are based on the concept of parameterising a set of energy levels using only a small number of parameters (in an analogous way to how scattering lengths parameterise ultra-low-energy scattering, as discussed in Chater 2 [101]). Whilst they were originally developed empirically for approximating the energy levels of alkali metal atoms as deviations from hydrogenic energy levels [102, 103], they have since been expanded to account for other potentials arising in other systems.

The original alkali atom paramaterisation was possible because the short-range and long-range physics of the outer electron's interaction with the inner core of the atom was separable due to the way the electrons effectively 'shielded' the charge of the nucleus from view [101]. The spirit of this short-range versus long-range distinction still persists in the method today. MQDT methods remain semi-empirical – the parameters, or *defects*, can be obtained empirically [102] or analytically [76], with the extension to multichannel cases meaning that couplings between potentials are included, too.

Finally, the Calculable R-Matrix Method employed in this work is especially well-suited to the problems arising in the study of systems with deep potential wells. This is due to the fact that the inner-region needs to be solved only once. Deep potential wells tend to have a very large number of vibrational energy levels below dissociation (related to the large number of Feshbach resonances they support, as discussed above), and in particular they have complicated short-range physics involving many partial waves at small distances.

The consequence of this is that a large basis set is needed to account for all of these states in the diagonalisation process. Because the Calculable approach performs this diagonalisation only once (and can discard high-lying states from the R-matrix sum, as discussed further in Chapter 3), it has efficiency advantages when compared to Propagator-Based R-Matrix methods, and other methods discussed in this section such as MQDT and hyperspherical approaches.

1.6 The Structure of this Thesis

- Chapter 2 introduces scattering theory and observables, in the single- and multichannel cases. There is also a discussion of the key theoretical results underpinning the R-matrix method, and some of the more specific theories utilised in this work. The two R-matrix definitions are explored in more detail.

Propagator methods are discussed, followed by a discussion of asymptotic expansions. Chapter 2 ends with a derivation of the analytic expression for the scattering observables for a particle scattering off a Morse potential.

- Chapter 3 explores the methods and algorithms employed in this work. A complete description of the entire RmatReact method used here is presented. There is a large discussion on the subject of Gaussian quadratures of various kinds, and variational basis representations and discrete variable representations are introduced and discussed. There is a section featuring a discussion of the numerical and computational issues that were encountered in the implementation of the RmatReact method.

- Chapter 4 presents results for scattering off a Morse potential, and comparisons to analytic results. This chapter is largely adapted from the paper Rivlin *et al.* (2019a) [104].

- Chapter 5 presents results for the ultracold elastic scattering of argon atoms off other argon atoms. The chapter is largely adapted from the paper Rivlin *et al.* (2019b) [105]. There is one additional section in this chapter concerning S-matrix poles which was not present in the original paper.

- Chapter 6 presents the theory for intramultiplet mixing in oxygen due to ultracold inelastic scattering with oxygen atoms, and presents preliminary results comparing cross-sections generated here with results from literature sources.

- Chapter 7 presents conclusions from the current work, descriptions of some ongoing work on the RmatReact method, and discussions of the potential future avenues the research featured here could take.

Chapter 2

Theory

In this chapter the quantum theory necessary to describe two atoms colliding over a set of mutual potential energy surfaces will be developed, in order to obtain scattering observables such as cross-sections. The R-matrix theory method for obtaining these scattering observables will then be presented. Theory will also be presented for analytic scattering, specifically over the Morse oscillator potential energy curve [106].

2.1 Scattering Theory

Before explaining R-matrix theory specifically, it is necessary to discuss quantum scattering in general.

Note that while many of the derivations in this chapter and the next one are standard (much of it is taken from P. G. Burke's *R-Matrix Theory of Atomic Collisions* [30]), it is usually given in atomic units (where it is assumed that $\hbar = m_e = e = 1$), since the R-matrix theory developed from it is most often applied to electron-atom/molecule collisions. [30, 29]. This means that the reduced mass terms which appear in diatomic physics equations are missing. In this work they must be included explicitly.

Burke's textbook also makes the assumption that the reaction occurs in the rest frame of the larger reactant, in his case the atom or molecule, as opposed to the electron. This is a reasonable assumption for the systems considered in that work. However, since in this work the reactants are more similar in mass (in some cases equal in mass), a different reference frame may be needed to describe the reactions.

In this work, all reactions are considered in body-fixed coordinates. The implications of using body-fixed coordinates versus using space-fixed coordinates include modifications to the kinetic operator in some Hamiltonians [107] to include (e.g.) Coriolis coupling terms [108]. The definition of the scattering energy does not change. In both cases it is defined relative to the centre-of-mass energy of the reactants. It is intended in the future for the RmatReact method to be adapted to both body-fixed and space-fixed coordinates, in order to facilitate the study of, for instance, external magnetic fields interacting with the reactants.

2.1.1 Single Channel Scattering Theory

Before analysing the full scattering theory, where energy can be exchanged and quantum numbers can be altered by the collision event, the theory necessary to describe elastic scattering will be presented. This is single channel scattering.

As always, one begins with the Schrödinger equation. If no energy is exchanged or quantum numbers changed during the interaction, and time is not being considered, then the equation for a pair of atoms interacting over a mutual potential energy surface is:

$$\hat{H}\Psi(\mathbf{r}) = E\Psi(\mathbf{r}), \tag{2.1}$$

where E is the scattering energy in the frame one is analysing the system in measured relative to some zero of energy, $\hat{H}$ is the Hamiltonian of the system, and $\Psi(\mathbf{r})$ is the wavefunction of the scattered atom in the spherical polar coordinates $\mathbf{r} = (r, \theta, \phi)$.

If the atoms interact over a mutual, single-dimension potential energy surface (known as a potential energy curve or PEC) $V(\mathbf{r})$, then the Hamiltonian has the form:

$$\hat{H} = \frac{-\hbar^2}{2\mu}\nabla^2 + V(\mathbf{r}), \tag{2.2}$$

with $\mathbf{r}$ representing all three coordinates, and where μ is the reduced mass of the system of two masses m_1 and m_2:

$$\mu = \frac{m_1 m_2}{m_1 + m_2}. \tag{2.3}$$

In this derivation the system is effectively being treated as a featureless particle scattering off a potential well, with no consideration for the structure of that particle or potential (assuming there are no degeneracy factors) – if it cannot exchange quantum numbers then it may as well have none.

It is possible to separate the wavefunction into angular and radial parts through a partial wave expansion that separates the total wavefunction into different components with different symmetries. In the single-channel case derived here, the symmetries are given by different total angular momentum quantum numbers, such that:

$$\Psi(\mathbf{r}) = \sum_{J=0}^{\infty} B_J(k) \frac{\psi^J(r)}{r} P_J(\cos\theta), \tag{2.4}$$

where J is the quantum number representing the total angular momentum of the two atoms, $\psi^J(r)$ is the radial part of the total wavefunction $\Psi(\mathbf{r})$, r is the internuclear separation coordinate, $B_J(k)$ are expansion coefficients, $P_J(x)$ are Legendre polynomials, and k is the scattering wavenumber, which is related to the scattering energy by the equation

$$k = \frac{\sqrt{2\mu E}}{\hbar}, \tag{2.5}$$

and when multiplied by $\hbar$ gives the linear momentum.

This derivation assumes cylindrical symmetry such that integrating the ϕ variable out of the $\mathbf{r}$ vector gives a constant 2π factor that can be incorporated into the normalisation.

The partial wave expansion is useful because it allows a three-dimensional problem to be reduced to a one-dimensional one, in the case where the PEC is central. In this partial wave expansion, the angular components of the wavefunction $\Psi(\mathbf{r})$ are accounted for by the sum over different values of angular momentum – each term in the sum is a separate partial wave.

The (reduced) radial wavefunction for a given total angular momentum J,

$\psi^J(r)$, obeys its own radial Schrödinger equation, which has the form:

$$\hat{H}^J \psi^J = E \psi^J, \tag{2.6}$$

where

$$\hat{H}^J = \frac{-\hbar^2}{2\mu} \frac{d^2}{dr^2} + \frac{\hbar^2 J(J+1)}{2\mu r^2} + V(r). \tag{2.7}$$

Solving the radial Schrödinger equation to obtain the scattering wavefunction $\psi^J(r)$ will allow one to obtain the scattering observables such a the cross-sections for given values of J. By summing over the scattering observables for a given J, one can obtain the scattering observables for the full 3D equation. A brief discussion of the full 3D scattering observables is given in Section 2.1.3.

In order to obtain the scattering wavefunction, one must impose two boundary conditions. Most commonly, one chooses one boundary condition at zero distance, and one at asymptotic distances. In the $J = 0$ case for the systems considered in this work, these boundary conditions have the form

$$\psi^0(r = 0) = 0 \tag{2.8}$$

$$\psi^0(r \to \infty) = \sin(kr)\cos\left(\delta^0(k)\right) + \cos(kr)\sin\left(\delta^0(k)\right) \tag{2.9}$$

$$= \sin(kr) + \cos(kr)\tan\left(\delta^0(k)\right). \tag{2.10}$$

Equations 2.9 and 2.10 are equivalent – the boundary condition is the same in both cases. The former makes it more clear that there are no physical poles in the asymptotic form of $\psi^0(r)$, whilst the latter makes derivations of scattering quantities more straightforward.

These boundary conditions can be interpreted as saying that it is assumed that at zero distance, the wavefunction has no amplitude, and at infinite distance, the wavefunction has the form of a free particle, only modified by the $\tan\left(\delta^0(k)\right)$ term. Because this manifests only as a shift in phase relative to that of a free particle, the term $\delta^0(k)$ is known as the *phase shift*.

The $r = 0$ boundary condition is straightforward to justify from a physics perspective for the problem described in this work: any realistic diatomic potential energy curve plotted along the radial coordinate will have a large repulsive barrier close to $r = 0$, caused by classical effect of Coulomb repulsion between the electrons combined with the quantum effect of Pauli exchange repulsion between the electrons.

The repulsive barrier rises indefinitely at distances close to $r = 0$ (ignoring the effects of nuclei overlapping at extremely small values of r), and thus the wavefunction amplitude exponentially decreases as it approaches $r = 0$, making the assumption that $\psi^0(r = 0) = 0$ a robust one.

For $J > 0$, the $r = 0$ boundary condition remains the same, and the sine and cosine terms in the asymptotic boundary condition are replaced by modified spherical Bessel functions of the first and second kind (the latter of which are known as Neumann functions) [109]:

$$\psi^J(r \to \infty) = s_J(kr) + c_J(kr)\tan\left(\delta^J(k)\right), \tag{2.11}$$

where for spherical Bessel function $j_\nu(x)$ and spherical Neumann function $n_\nu(x)$,

$$s_\nu(x) = x j_\nu(x) \tag{2.12}$$

$$c_\nu(x) = -x n_\nu(x). \tag{2.13}$$

More sophisticated boundary conditions are also employed for certain calculations later in the project, known as asymptotic expansions. These are discussed in Section 2.2.3.

The problem of finding the scattering wavefunctions $\psi^J(r)$ in order to obtain the scattering observables is (indirectly) the principle issue of this thesis, for which the R-matrix method (to be introduced in Section 2.2) will be utilised.

2.1.2 Multichannel Scattering Theory

Whilst the total energy E_{tot} is conserved, it is possible for different energies to be transferred in an interaction. If the interaction causes energy to be exchanged between the atoms, or for the quantum numbers of the atoms to be changed, then multiple coupled potential energy curves must be involved in the interaction.

If the system can transition between potential energy curves, there must be a coupling term between the PECs. There must also be a theory describing how these interactions occur, which must be able to produce scattering observables such as the cross-section of the transition between levels. This theory is introduced here.

Much of this theory is analogous to the single-channel case. The full Schrödinger equation for the system will involve a Hamiltonian which contains every PEC and PEC coupling, and which acts on each of the 3D wavefunctions $\Psi_i(\mathbf{r})$ for a given channel i which is located an energy E_i above some zero in energy (usually the lowest channel's energy) [110]:

$$\left(\frac{d^2}{dr^2}+k_i^2\right)\Psi_i(\mathbf{r})=\frac{2\mu}{\hbar^2}\sum_{i'}V_{ii'}(\mathbf{r})\Psi_{i'}, \tag{2.14}$$

where the diagonal elements of $V_{ii'}$ correspond to PECs for a given set of quantum numbers, and the off-diagonal elements represent couplings between those PECs. k_i, the scattering wavenumber (squared) associated with the ith channel, is defined by

$$k_i^2=\frac{2\mu}{\hbar^2}(E_{\text{tot}}-E_i), \tag{2.15}$$

where E_{tot} is the total energy in the frame being considered.

The scattering energy can be defined relative to any channel. There is a total energy of a reactant, E_{tot}, which is the sum of the scattering energy E and the energy E_i of the channel it is scattering off. This quantity is conserved, and when one changes which channel the scattering energy is defined relative to, one changes the scattering energy alongside it such that the total energy is conserved. Even if the channel which is being scattered off is high in energy, the scattering can still be considered ‘ultracold’ if it is only a very small amount of energy higher than the channel's energy – the translational energy of the system is still ultracold.

J is the total angular momentum of the system, and τ is the parity. These are the two globally conserved quantum numbers (no problems were considered in this work that broke either of those two symmetries), and along with the total energy E_{tot} they are the only conserved quantities.

The partial wave expansion which is analogous to Equation 2.4 now involves expanding a wavefunction labelled by η as a sum over many quantum numbers. This sum includes infinite values of total angular momentum J, two values of parity τ, infinite values of orbital angular momentum ℓ (assuming space-fixed coordinates), and N_c channels of non-conserved quantum numbers, which are described by the functions $\Phi_{i\ell}^{J\tau}$:

$$\Psi_\eta(\mathbf{r}) = \sum_{J=0}^{\infty} \sum_{\tau} \sum_{\ell=0}^{\infty} \sum_{i=1}^{N_c} A_{i\eta\ell}^{J\tau} \frac{\psi_{i\eta\ell}^{J\tau}(r)}{r} P_\ell(\cos\theta) \Phi_{i\ell}^{J\tau}, \tag{2.16}$$

where the coefficients $A_{i\eta}^{J\tau}$ are determined by matching to plane wave solutions of the equation at asymptotic distances [110]. Note that if the energy level of channel i is degenerate, then the N_j degenerate channels at that energy must be summed over too. Also note that in body-fixed coordinates, the ℓ quantum number is replaced with a different angular momentum quantum number, such as j (see Chapter 6.

Each different set of quantum numbers $\{J\tau\}$ corresponds to a different symmetry, which are condensed into one label Γ for convenience henceforth. Each channel with quantum numbers i corresponds to a different electronic state with a different PEC.

As in the single channel case, by expanding the full 3D wave function in this way, the angular coordinates are captured in the symmetries corresponding to the angular momentum quantum numbers. The remaining radial wave function $\psi_{i\eta}^{\Gamma}(r)$ is the solution to a radial Schrödinger equation.

To account for the transitioning between electronic states, it is useful to represent the radial wave function as a vector, so that for a system with N_c channels,

$$\boldsymbol{\psi}_\eta^\Gamma(r) = \begin{pmatrix} \psi_{1\eta}^\Gamma(r) \\ \psi_{2\eta}^\Gamma(r) \\ \vdots \\ \psi_{N_c\eta}^\Gamma(r) \end{pmatrix}. \tag{2.17}$$

This vector can be thought of as one column of a general matrix $\boldsymbol{\psi}^{\Gamma}$ with the number of columns equal to the number of scattering solutions η of the full reduced radial Schrödinger equation for a given symmetry Γ.

As such, within a given symmetry Γ there will be a Hamiltonian matrix $\hat{\boldsymbol{H}}^{\Gamma}$, with each element corresponding to an element of the potential matrix $\boldsymbol{V}(r)$ (with a kinetic term, too). For a given scattering solution η, the Schrödinger equation for a given symmetry is turned into a matrix eigenvalue equation of the form:

$$\hat{\boldsymbol{H}}^{\Gamma}\boldsymbol{\psi}^{\Gamma}_{i\eta}(r) = E_{\text{tot}}\boldsymbol{\psi}^{\Gamma}_{i\eta}(r). \tag{2.18}$$

Another way of writing this equation is in the form

$$\left(\frac{d^2}{dr^2} + k_i^2\right)\psi^{\Gamma}_{i\eta}(r) = \frac{2\mu}{\hbar^2}\sum_{i'} V^{\Gamma}_{ii'}(r)\psi^{\Gamma}_{i'\eta}(r), \tag{2.19}$$

where $V^{\Gamma}_{ii'}(r)$ includes angular momentum terms such that

$$\mathbf{V}^{\Gamma} = \mathbf{V} + \frac{\hbar^2\mathbf{R}}{2\mu r^2}, \tag{2.20}$$

where $\mathbf{R}$ is the rotational angular momentum matrix expressed as the difference between the total angular momentum $\mathbf{J}$ and the total internal angular momentum of the system $\mathbf{j}$ such that $\mathbf{R} = \mathbf{J} - \mathbf{j}$ [86] (this is equivalent to the quantum number ℓ discussed above).

The multichannel case also has equivalent boundary conditions to Equations 2.8, 2.10, and 2.11. The boundary conditions are

$$\psi^{\Gamma}_{i\eta}(r=0) = 0 \tag{2.21}$$

$$\psi^{\Gamma}_{i\eta}(r \to \infty) = k_i^{-\frac{1}{2}}\left(\sin(k_i r) + \sum_{i'} K^{\Gamma}_{ii'}\cos(k_{i'} r)\right), \tag{2.22}$$

where $K^{\Gamma}_{ii'}$ is dimensionless number, an element of a quantity known as the K-matrix, which will be discussed more in Section 2.1.3.2 and Section 2.2.3.2, where further discussion of the boundary conditions will also be presented.

2.1.3 Scattering Observables

2.1.3.1 Single Channel Scattering Observables

The $\tan\left(\delta^{\Gamma}(k)\right)$ term in Equation 2.11 is the single-channel definition of the K-matrix, $K^{\Gamma}(k)$, which is an important quantity in scattering theory. The argument of the tangent function, $\delta^{\Gamma}(k)$, is called the phase shift or the *eigenphase*, and is an important quantity in its own right.

Loosely speaking, the K-matrix and the quantity known as the eigenphase, which is measured in radians, can be thought of as measures of the extent to which an otherwise free particle's wavefunction is modified by interaction with a potential. If the potential is zero, then the eigenphase is zero, and the asymptotic wavefunction is that of a free particle. For non-zero potentials, the influence of that potential is measured through its impact on the value of the eigenphase.

Although the K-matrix is not a measurable quantity itself, all scattering observables can be derived directly from it. The outputs of the R-matrix-based algorithms described in this work will be K-matrices for various collision processes, and the scattering observables derived from them.

In the single channel case, the eigenphase and K-matrix are simply scalar functions of scattering energy. The K-matrix itself (confusingly called the reactance, or R-matrix by some authors [110]) is defined as the term which multiplies the cosine in Equation 2.11.

Similarly, in the single channel case the quantities known as the scattering, or S-matrix, and the transition, or T-matrix are given in terms of the K-matrix by

$$S^{\Gamma}(k) = \frac{1 + iK^{\Gamma}(k)}{1 - iK^{\Gamma}(k)} \tag{2.23}$$

$$T^{\Gamma}(k) = S^{\Gamma}(k) - 1. \tag{2.24}$$

Note that some authors define the T-matrix to be the negative of the value presented here. In the single-channel case only, the S-matrix can also be defined as

$$S^{\Gamma} = \exp\left(2i\delta^{\Gamma}(k)\right). \tag{2.25}$$

And further note that some authors define this without the 2 in the exponent, which also changes the first definition given here.

One physical interpretation of the S-matrix stems from the fact that it can also be defined in the $r \to \infty$ limit as the negative of the ratio of the coefficients of the outgoing free particle component of the asymptotic radial wavefunction to the incoming free particle component [30, 111], when considering a general free particle solution to a wave equation, as in the asymptotic boundary conditions of the scattering Schrödinger equation.

This can be seen from an alternate way of expressing the boundary conditions in Equations 2.10 and 2.11, which arises from the definition in Equation 2.23:

$$\psi^{\Gamma}(r \to \infty) = \exp\left(-i\theta^{\Gamma}\right) - \exp\left(i\theta^{\Gamma}\right)S^{\Gamma}(k), \tag{2.26}$$

where $S^{\Gamma}(k)$ is the S-matrix and $\theta^{\Gamma} = kr - \frac{1}{2}J\pi$.

Like the eigenphase, The S-matrix and T-matrix can also be interpreted as measuring the deviation of the scattering wavefunction from the case of zero potential. Specifically, if there is no potential, then $S^{\Gamma}(k) = 1$ and $T^{\Gamma}(k) = 0$.

Whilst these various matrices are useful for characterising scattering events, they are not strictly speaking observable quantities. Arguably the most important scattering observable is the total cross-section of the interaction, which, for the partial wave expansion outlined in this work, can be expressed entirely in terms of the K-matrix.

The integral cross-section, measured in units of length squared, is given by integrating the differential cross-section over all solid angle $\Omega = (\theta, \phi)$:

$$\sigma_{\text{int}} = \iint \frac{d\sigma}{d\Omega} \sin\theta d\Omega. \tag{2.27}$$

The integral cross section can be interpreted physically as a measure of the probability of any interaction at all occurring between the scattering atoms. It is the effective surface area of the interaction space, and larger cross sections imply larger probabilities of interactions occurring.

The derivative $\frac{d\sigma}{d\Omega}$ in the integral in Equation 2.27 is the differential cross section, which is the cross-section per unit solid angle. This can be interpreted as a measure of the probability of the scattering event occurring for a given solid angle. The integral cross section is then simply the sum of all of the differential cross sections at all possible solid angles. Differential and integral cross-sections are not considered in this work.

Cross sections are a useful measure for many reasons. One reason relevant to this work is that when plotted as a function of collision energy E, then the resonances discussed in the previous chapter become easy to identify, as they impact the cross section significantly around the energies they occur at. Indeed, one of the main advantages of the R-matrix method to be discussed in the next chapter is that it facilitates inexpensive, fast computations of events at multiple scattering energies, which allows one to produce very high resolution plots of $\sigma_{\text{tot}}(k)$ to easily identify resonances.

Another reason cross sections are an important scattering observable is the relative ease with which they can be measured by experimentalists. Quoting cross sections is standard practice for most scattering experiments, allowing for benchmarking between these results and experimental ones.

If one wishes to remove considerations of the angular coordinates from the calculations, then the total cross-section can be defined from the partial wave expansion. In the single-channel case, this expansion has the form:

$$\sigma_{\text{tot}}(k) = \sum_{J=0}^{\infty} \frac{4\pi}{k^2} g_J \sin^2(\delta^J(k)), \tag{2.28}$$

where g_J is the degeneracy factor for the partial wave with angular momentum J. For a simple particle scattering off a potential, then g_J is given by $(2J+1)$. If there are other quantum numbers to be considered in the scattering, such as nuclear spin, then the g_J term may include other components.

The summand of Equation 2.28 is defined as $\sigma^J(k)$, the partial wave cross section for a given value of J. This can be interpreted as a measure of the probability of the atoms interacting for a given value of J.

Another pair of useful scattering observables can be derived from a polynomial expansion of the eigenphase in the low energy limit. In the single channel case, at low energy, when $J = 0$, one can write the following expansion:

$$k \cot\left(\delta^0(k)\right) = -\frac{1}{A} + \frac{1}{2} r_{\text{eff}} k^2 + O(k^4). \tag{2.29}$$

The two parameters in the expansion, A and r_{eff}, are known respectively as the scattering length and the effective range. It is possible to define a similar expansion for non-zero values of J, but in this work only the $J = 0$ expansion was considered.

There are alternate ways of defining both the scattering length and the effective range. Equation 2.29 suggests that the scattering length can also be defined as the low energy limit

$$\lim_{k \to 0} k \cot\left(\delta^0(k)\right) = -\frac{1}{A}. \tag{2.30}$$

The physical interpretation of the scattering length is as the length scale which governs the physics of the interaction at low energy. For instance, at sufficiently low energies, the cross section of an interaction can be given as simply the square of the scattering length:

$$\lim_{k \to 0} \sigma_{\text{tot}}(k) = 4\pi A^2. \tag{2.31}$$

The effective range is named as such [112, 113] because it can be interpreted as a quantity which represents the length range over which, at low energies, the effects of the potential can be felt by the scattering atoms – the effective range of the potential. This interpretation becomes more clear when considering another way of defining the effective range:

If one defines the wavefunction associated with the solution of Equation 2.6 for a PEC V at $J = 0$ and $E = 0$ to be $\psi_{(0,V)}(r)$, then one can also define a wavefunction $\psi_{(0,0)}(r)$ to be the solution to the same equation, only with $V = 0$. In such a case, then the effective range can be defined as

$$r_{\text{eff}} = 2 \int_0^\infty \left(\psi^2_{(0,0)}(r) - \psi^2_{(0,V)}(r) \right) dr. \tag{2.32}$$

In other words, the effective range is a more sophisticated comparison between the zero-energy scattering wavefunction when there is no potential present, versus when there is a potential present (as compared to the interpretations of the eigenphase, S-matrix and T-matrix outlined above) [112, 113].

This is because the effective range takes the form of an integral over all space of the squared difference between the two functions. The result of the integral is a length quantity that describes how the wavefunction is changed by the presence of the potential, when at zero scattering energy. The larger the value of r_{eff}, the more substantial the effect of the potential is at low energy, and hence the larger its range of effect.

In practice, in this work both the scattering length and effective range were obtained by calculating the eigenphase at low values of k. By plotting $k\cot\delta^0(k)$ against k^2, and using linear fitting features in software such as ORIGIN (OriginLab, Northhampton, MA) to obtain the slope and intercept of the plot, the values of A and r_{eff} could be derived directly.

The scattering length and effective range are useful as, like with the cross section, they are quantities which experimental researchers can provide values for, which is useful for benchmarking purposes. As mentioned in Chapter 1, one example of this is in simulations of Bose-Einstein Condensates (BECs), where they are the contribution from atomic physics to these simulations [32, 57].

2.1.3.2 Multichannel Scattering Observables

In the multichannel case, the relationship between the K-matrix and the eigenphase is not as straightforward as the former simply being the tangent of the latter, and the scattering observables take on more complex forms.

The quantity $K^J(k)$ is replaced by a matrix $\mathbf{K}^\Gamma(k)$, which has dimensions $N_a \times N_a$ for a problem with N_a open target states, or channels. The K-matrix does not run over closed channels: any states which are higher in energy than the scattering energy at infinite distance are not accessible for scattering off, and thus there are no allowed transitions between open and closed channels. As in Section 2.1.2, Γ corresponds to the list of conserved quantum numbers, which is referred to as a single *symmetry*. k is still the scattering wavenumber. The scattering observables can still be obtained from this quantity, which is defined and discussed in Section 2.2.3.2. Note that the K-matrix is symmetric, as are all matrices derived from it.

The new relationship between the K-matrix and the eigenphase is as follows: first the matrix $\mathbf{A}$ is introduced, which is the matrix of normalised eigenvectors of the matrix $\mathbf{K}$ (where the symmetry label and dependence on k are not explicitly stated for any of the matrices introduced in the following discussion). Thus the diagonal matrix of eigenvalues of $\mathbf{K}$ can be written as

$$\tan(\mathbf{\Delta}) = \mathbf{A}^{\mathrm{T}}\mathbf{K}\mathbf{A}, \tag{2.33}$$

where $\mathbf{A}^T$ is the transpose of $\mathbf{A}$.

By writing the matrix $\mathbf{\Delta}$ as

$$\tan(\mathbf{\Delta}) = \begin{pmatrix} \tan(\delta_1) & 0 & \dots & 0 \\ 0 & \tan(\delta_2) & \dots & \vdots \\ \vdots & \vdots & \ddots & \\ 0 & 0 & \dots & \tan(\delta_N) \end{pmatrix}, \tag{2.34}$$

it is possible to identify the arctangent of the ith element on the diagonal, $\delta_i(k)$, with the eigenphase introduced previously. In this case, $\delta_i(k)$ is the *partial* eigenphase.

Another quantity, known as the eigenphase sum $\delta(k)$, is simply the sum of all N_a of these partial eigenphases:

$$\delta^{\Gamma}(k) = \sum_{i=1}^{N_a} \delta_i^{\Gamma}(k), \tag{2.35}$$

where the Γ and k labels are explicitly included. This is the quantity which can most closely be identified as the multichannel equivalent of the definition given at the beginning of Section 2.1.3.1 [29].

Other matrices which can be derived from the $\mathbf{K}$ matrix include multichannel versions of the S- and T-matrices. Defining $\mathbf{1}$ as the identity matrix, and i as the imaginary unit,

$$\mathbf{S} = (\mathbf{1} + i\mathbf{K})(\mathbf{1} - i\mathbf{K})^{-1} \tag{2.36}$$

$$\mathbf{T} = \mathbf{S} - \mathbf{1}, \tag{2.37}$$

The matrix $\mathbf{S}$ can also be diagonalised by the same matrix $\mathbf{A}$ that diagonalises $\mathbf{K}$, such that

$$\mathbf{A}^{\mathrm{T}}\mathbf{S}\mathbf{A} = \exp(2i\boldsymbol{\Delta}), \tag{2.38}$$

where the ith diagonal element of the diagonal matrix $\exp(2i\boldsymbol{\Delta})$ is $\exp(2i\delta_i)$.

The multichannel cross-section is dependent on the elements of the T-matrix for a given symmetry Γ. The total cross-section for a transition from channel i to channel i' at scattering energy E is given by [114, 110]

$$\sigma^{\mathrm{Tot}}\left(i \to i'\right)(E) = \sum_{\Gamma} g_{\Gamma}\sigma^{\Gamma}\left(i \to i'\right)(E), \tag{2.39}$$

where g_{Γ} is the total degeneracy for that symmetry, and $\sigma^{\Gamma}(i \to i')(E)$ is the partial cross-section for the transition from i to i' for a given symmetry Γ. This quantity is given by the expression

$$\sigma^{\Gamma}\left(i \to i'\right)(E) = \frac{\pi}{k_i^2}\frac{1}{g_i}|T_{ii'}^{\Gamma}(E)|^2, \tag{2.40}$$

where k_i is the wavenumber of the incoming channel i as given by Equation 2.15, g_i and $g_{i'}$ are the degeneracies of the channels i and i', and $T_{ii'}^{\Gamma}(E)$ is the element of the T-matrix which couples channel i to channel i' at energy E.

When $i \neq i'$, the principle of detailed balance suggests that, for a given scattering energy, [114, 110]

$$\sigma^{\Gamma}\left(i \to i'\right) = \frac{k_{i'}^2}{k_i^2}\frac{g_{i'}}{g_i}\sigma^{\Gamma}\left(i' \to i\right). \tag{2.41}$$

If $i = i'$, then this is an elastic scattering cross-section. If not, then it is the cross-section for the transition from one state to the other.

Here the N_j degenerate channels labelled j for each degenerate energy level i from Section 2.1.2 can be re-introduced. Doing so means one must sum over these channels to obtain the expression for $\sigma^\Gamma\left(i \to i'\right)(E)$:

$$\sigma^\Gamma\left(i \to i'\right)(E) = \frac{\pi}{k_i^2}\frac{1}{g_i}\sum_{j=1}^{N_j}\sum_{j'=1}^{N_{j'}}|T^\Gamma_{iji'j'}(E)|^2. \tag{2.42}$$

If there are any degeneracy factors arising from the additional label j then they must also be included in the sum.

The degeneracy factors g_Γ and g_i depend on the specific quantum numbers involved in the reaction. As discussed in Section 2.1.2, Γ in this work is usually composed of two quantum numbers: total angular momentum J, and parity, τ. As stated previously, g_J is usually given by $(2J+1)$, since parity adds no degeneracy to the sum:

$$g_\Gamma = (2J+1). \tag{2.43}$$

2.1.4 Resonances

Resonances are features which are present in both the single- and multichannel cases in many plots of the eigenphase and cross-section as a function of scattering energy. It is also possible to have resonances in plots of cross-sections as a function of other variables, too, such as electric field strength [115]. Resonances usually have a distinct functional form in plots of the eigenphase, as seen in Figure 1.1. As a consequence, the energy of the resonance and the inverse of its lifetime, known as its width, can be determined by fitting a function to the eigenphase. One functional form that resonances can be fitted to follows Breit and Wigner [35, 30, 36]:

$$\delta^\Gamma(E) = A_0 + A_1 E + \arctan\frac{\Gamma_\text{res}}{E - E_\text{res}}, \tag{2.44}$$

where $\delta^\Gamma(E)$ is the eigenphase for partial wave Γ at scattering energy E, Γ_res is the width of the given resonance (not to be confused with the symmetry label Γ), and E_res is the energy of the resonance. Note that this definition of Γ_res follows the convention used in, for instance, Tennyson & Noble [36], and differs by factor of two from the definition of the full width at half maximum (FWHM) of a function used in other works.

For shape resonances, the quantity Γ_{res} is also the connection between the form of the resonance and the physical properties of the associated quasibound energy level. Γ_{res} is the width of the resonance, and also the inverse of the characteristic lifetime of the level – the wider the resonance, the shorter-lived the associated level is.

The non-resonant shape of the eigenphase (the ‘background’ eigenphase) is accounted for by the two terms A_0 and A_1, where it is assumed that the width is narrow enough that the background eigenphase can be approximated by a linear function of E over its length. By fitting a generated eigenphase to a function of this form, values for Γ_{res} and E_{res} can be obtained.

Another functional form that can represent resonances is the characteristic Fano profile [37], which appears in results in Section 5, specifically Figure 5.5. These asymmetric profiles, which can indicate resonances of any type, are the consequence of interaction between the resonance and background scattering. Fano profiles are discussed further in Section 5.

2.1.5 S-matrix Poles

The S-matrix, defined in Section 2.1.3 as the exponent of the eigenphase in Equation 2.111, has a few particularly useful physical interpretations when extended to the complex plane. Here the discussion is restricted to the single-channel S-matrix.

For real values of k, the S-matrix has the straightforward interpretation of being the ratio of outgoing and incoming scattering wavefunctions, but when the single-channel S-matrix $S^J(k)$ is plotted for complex values of k over the whole complex plane, the poles which occur off the real-axis can be shown to correspond to a variety of physical features (and a handful of unphysical) of the scattering system, depending on their location within the complex plane.

This discussion is based on discussions of the properties of the S-matrix and its poles which are found in a collection of sources [116, 117, 30, 111].

There are specific rules about where S-matrix poles can occur in the complex

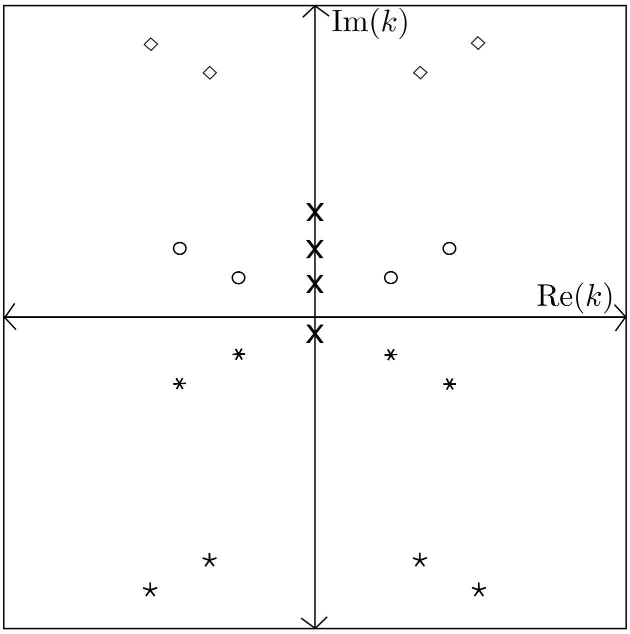

Figure 2.1: A possible distribution of S-matrix poles and zeroes for complex values of k. The poles on the imaginary axis in the upper half plane represent bound states. The pole in the lower half plane on the imaginary axis represents a virtual state. The poles near to the real axis off the imaginary axis in the lower half plane represent resonances, whilst the poles further away from the real axis and off the imaginary axis in the lower half plane represent unphysical background scattering poles. All these poles appear in pairs reflected about the imaginary axis. The zeroes of the S-matrix are also represented in the upper half plane. Each zero exactly corresponds to one pole in the lower half plane.

plane. Defining k_{Re} and k_{Im} such that $k = k_{\mathrm{Re}} + ik_{\mathrm{Im}}$, in the upper half plane, when $k_{\mathrm{Im}} > 0$, the poles can only occur when they are on the imaginary axis: when $k_{\mathrm{Re}} = 0$. S-matrix poles in the lower half plane, when $k_{\mathrm{Im}} < 0$, can occur anywhere, with one constraint: poles in the lower half plane occurring off the imaginary axis (such that $k_{\mathrm{Re}} \neq 0$) always come in pairs reflected about the imaginary axis. Figure 2.1 describes which poles are possible.

Furthermore, every pole in the lower half plane that occurs off the imaginary axis also corresponds to a zero in the upper half plane: the real coordinate of the zero is the same as the real coordinate of the corresponding pole, and the imaginary coordinate of the zero is the negative of the imaginary coordinate of that pole: the zero is the pole's reflection about the real axis.

The poles occurring in the upper half plane on the imaginary axis are the most straightforward to interpret: each pole corresponds to a bound state of the bound system. If the pole occurs at the imaginary $k_{\mathrm{Re}} = 0$, $k_{\mathrm{Im}} > 0$, then the energy of the corresponding bound state energy E is given by $\frac{\hbar^2}{2\mu} k_{\mathrm{Im}}^2$.

Since these poles correspond to bound states, plotting values of $S^J(k)$ for imaginary values of k where $k_{\mathrm{Re}} = 0$ and $k_{\mathrm{Im}} > 0$ is a potential method for finding bound states.

There is one other type of S-matrix pole that corresponds to a physical observable. Poles in the lower half plane that occur off the imaginary axis correspond to resonances in the scattering process. For $k_{\mathrm{Im}} < 0$, if a pole is located at $k = k_{\mathrm{Re}} + ik_{\mathrm{Im}}$, then the energy E_{res} and width Γ_{res} of the corresponding resonance are given by

$$E_{\mathrm{res}} - \frac{1}{2} i\Gamma_{\mathrm{res}} = \frac{\hbar^2}{2\mu} \left(k_{\mathrm{Re}} + ik_{\mathrm{Im}}\right)^2, \tag{2.45}$$

such that the energy of the resonance is given by

$$E_{\mathrm{res}} = \frac{\hbar^2}{2\mu} \left(k_{\mathrm{Re}}^2 - k_{\mathrm{Im}}^2\right), \tag{2.46}$$

and the width is given by

$$\Gamma_{\mathrm{res}} = -4\frac{\hbar^2}{2\mu} k_{\mathrm{Re}} k_{\mathrm{Im}}. \tag{2.47}$$

This means that an S-matrix pole-finding algorithm can also serve as a general resonance finder [118]. This resonance finding method can be compared to a different numerical resonance finding method outlined in Tennyson & Noble [36].

It is possible for the poles to correspond to resonances of any type, but there is an important caveat: not all poles correspond to physical resonances. The larger $|k_{\mathrm{Im}}|$ becomes, the less likely a pole at that value of k is to correspond to a real observable, although there is no clear cut-off between physical and unphysical poles when interpreting an S-matrix. This phenomenon is known as ‘background scattering’.

The explanation for this phenomenon is that the width of the resonances become larger as $|k_{\mathrm{Im}}|$ is increased. According to Nussenzveig, “as the poles get farther away from the real axis, the corresponding resonance peaks in the scattering cross-section become broader and broader, tending to overlap in an inextricable way, until they merge into a slowly-varying background" [116]. This was said in the context of square-well scattering, but the concept applies generally.

Another explanation is that the asymptotic values of the potentials become more important at these larger $|k_{\text{Im}}|$ values. Again from Nussenzveig: "the asymptotic behaviour of the large poles depends very critically on the asymptotic behaviour of the potential. Physically unimportant changes in the potential may completely modify the behaviour of the large poles, so that these poles cannot have much physical significance This 'hypersensitiveness' of the poles with respect to asymptotic conditions, which had previously been noticed in the case of "spurious" poles, is a very unwelcome feature of the S-matrix formalism" [116].

Finally, there is one more type of S-matrix pole which has implications for the physics of the scattering problem. It is also possible for poles to exist in the lower half plane for $k_r = 0$: on the imaginary axis for $k_{\text{Im}} < 0$. These poles do not occur in pairs. They also do not correspond to resonances, or directly to any particular physical observable.

Like the poles in the upper half plane on the imaginary axis, they correspond to energy levels. However they do not correspond to bound states of the bound system. Instead, the states they correspond to are called 'virtual' states, or 'anti-levels', and the poles associated with them are sometimes called 'anti-poles'. The levels are not physically present, but the presence of a virtual state in the complex plot of the S-matrix can have implications for the properties of the scattering system.

In particular, if a virtual state occurs very close to the origin, that can imply the existence of an anomalously large scattering length in the scattering observables. This in turn gives rise to a very large low-energy cross-section, too. In nuclear physics, where the R-matrix theory has its origins, this phenomenon is well known for neutron-proton scattering. Unlike for the poles close to the origin, the presence of poles far from the origin on the imaginary axis does not have a corresponding physical interpretation, and is largely meaningless.

A virtual state pole close to the origin is similar to a $J = 0$ bound state close to dissociation, which also implies the presence of a very large amplitude scattering length: as a state goes from being bound to being unbound as the well depth of the bound system decreases, the scattering length cycles from negative infinity through positive infinity, meaning that any real number is a possible scattering length, and that as the bound state's energy approaches zero, the scattering length is large. This is discussed further in Chapter 5.

2.2 The R-Matrix Method

Here a derivation and explanation of the R-matrix method is presented, as used to describe atoms scattering off each other. In general, the atoms may have a non-zero total angular momentum, J, and they may begin and end the interaction with different quantum numbers. Much of the derivation is adapted from the aforementioned Burke textbook [30] alongside some additional sources by Burke and Tennyson [119, 29]. Considerations are also made in the relevant equations for the reduced mass terms and change of reference frame.

The R-matrix method is one numerical method for calculating scattering observables arising from the scattering theory outlined above. As outlined in the previous chapter, the core principle of the R-matrix method is the partitioning of space into two regions: an inner region and an outer region. The different regions have different potential energy curves, usually with differing levels of numerical complexity and physical accuracy.

The partition is placed at a distance a_0 away from the centre of the reaction, i.e. the 0 of the reaction coordinate. All points for which the internuclear distance r is less than a_0 are in the inner region, and all points for which $r > a_0$ are in the outer region. The system and its physics are treated differently in the two regions, and information from the inner region is used to calculate scattering observables in the outer region.

There is furthermore a third region, known as the asymptotic region, which begins at a distance a_p away from $r = 0$ such that $a_p > a_0$. The point a_p is defined as the point where the effects of the potential can be regarded as negligible – it is the numerical version of assuming infinite distance. In some R-matrix methods, the potential is assumed to be exactly zero at this point, whereas in others it is assumed to still have a small value, and methods known as asymptotic expansions are used to account for this deviation from a zero value.

The explanation of the R-matrix will be divided into discussions of the three separate regions. For each region, a derivation of the simpler, single channel case will be presented first, followed by the extension to the multichannel version of the same theory.

2.2.1 The Inner Region

2.2.1.1 The Single Channel Inner Region

In the inner region, the two-atom system is assumed to be a quasi-bound diatom, and the PEC of the reaction is simply the PEC of a diatom. The reduced radial Schrödinger equation for this diatomic system has the form

$$\hat{H}^J \psi_k^J(r) = E_k^J \psi_k^J(r), \tag{2.48}$$

where the $\hat{H}^J$ is the Hamiltonian of the diatomic system, and the ψ_k^J and E_k^J are the eigenfunctions and eigenenergies associated with that Hamiltonian labelled by their angular momentum quantum numbers J. In the single channel case, the Hamiltonian and eigenfunctions are all scalars.

The core aim of the inner region calculation is to determine these eigenfunctions and eigenenergies, since they form the key part of the R-matrix sum from Equation 1.3.

The diatomic, one-dimensional Hamiltonian $\hat{H}$ of interest is defined in the following way:

$$\hat{H}^J = \frac{-\hbar^2}{2\mu}\frac{d^2}{dr^2} + \frac{\hbar^2 J(J+1)}{2\mu r^2} + V(r), \tag{2.49}$$

where r is the internuclear separation of the diatom, J is its total angular momentum, and $V(r)$ is an element of the matrix of potentials associated with the atomic channels, including the off-diagonal channel coupling elements. For a given value of J, one obtains the eigenenergies and eigenfunctions E_k^J and ψ_k^J of the Hamiltonian in Equation 2.49 using the Schrödinger equation of Equation 2.48.

The potential energy surfaces (which are just curves in this work, as there is only one reaction coordinate in the form of the internuclear distance) and the coupling strengths can be thought of as the inputs to the entire algorithm. They are obtained from a variety of experimental and theoretical sources (e.g. [120, 121, 122, 123, 124]) and, besides fundamental constants, are the only source of experimental data required to obtain the scattering observables at the end.

The implication of the inner region/outer region split is that the inner-region Schrödinger equation is only valid over a finite, bounded region of space: outside of the $[0, a_0]$ range, the Hamiltonian described above is not defined. This is arguably the core principle of the R-matrix method.

In principle, the choice of where to place the R-matrix boundary a_0 should not affect the underlying physics. In practice, the choice of where to define a_0 has significant computational implications in terms of accuracy and computational expense of the calculation, which will be discussed in Chapter 3.

The R-matrix provides the link between the inner region bound state problem of Equation 2.48 and the full scattering problem of Equation 2.6. The derivation of the link between the two begins by defining two operators:

$$L^J(r) = \frac{d^2}{dr^2} - \frac{2\mu}{\hbar^2} V^J(r) + k^2, \tag{2.50}$$

and

$$\mathscr{L}_{a_0} = \delta(r - a_0) \frac{d}{dr}, \tag{2.51}$$

where $\delta(r - a_0)$ is a Dirac delta centred around a_0, $V^J(r)$ is the potential term containing the angular momentum term, $L^J(r)$ is the operator form of Equation 2.6 divided by $\frac{\hbar^2}{2\mu}$ such that

$$L^J(r)\psi^J(r) = 0, \tag{2.52}$$

k is the scattering wavenumber in the body-fixed reference frame, related to the scattering energy by Equation 2.5, and $\mathscr{L}_{a_0}$ is a quantity known as the *Bloch* operator [125], such that $\mathscr{L}_{a_0}\psi_k^J(r)$ is a quantity known as the *surface term*.

Note that the general definition of the Bloch operator has an additional term dependent on some constant b, but this constant can be set to zero without loss of generality and is done so throughout this work. It can also be shown that different values of b do not affect the numerics of the method [126]. For completeness, the full expression for the Bloch operator is usually defined as:

$$\mathscr{L}_{a_0} = \delta(r-a_0)\left(\frac{d}{dr}-b\right). \tag{2.53}$$

The operator $L^J(r)$ is not Hermitian when integrated over a finite region of space, but the operator $\left(L^J(r)-\mathscr{L}_{a_0}\right)$ is Hermitian:

$$\int_0^{a_0}\left(v\left(L^J(r)-\mathscr{L}_{a_0}\right)w - w\left(L^J(r)-\mathscr{L}_{a_0}\right)v\right)dr = 0. \tag{2.54}$$

This is because the surface terms left over when integrating over the operator $L^J(r)$ are precisely cancelled by the terms introduced by the operator $\mathscr{L}_{a_0}$ (assuming that the functions are zero at $r=0$, as suggested by the boundary conditions in Equation 2.8). Note that if one integrates over an infinite region of space, and assumes that at infinite distances the functions v and w tend to zero, then L^J is Hermitian, as one would expect. It is the combination of a finite boundary and non-zero boundary conditions at that boundary that introduce non-Hermiticity to the problem.

The operator $\left(L^J(r)-\mathscr{L}_{a_0}\right)$ has a complete spectrum of eigenvalues and eigenvectors over the range $r=0$ to $r=a_0$. This means that the Green's function [127] of the operator can be represented in terms of those eigenvalues and eigenvectors, due to the completeness relation. It can be shown that the R-matrix *is* the spectral representation of the Green's function of the operator $\left(L^J(r)-\mathscr{L}_{a_0}\right)$. By subtracting $\mathscr{L}_{a_0}\psi^J(r)$ from both sides of Equation 2.52, one can see that the equation

$$\left(L^J(r)-\mathscr{L}_{a_0}\right)\psi^J(r) = -\mathscr{L}_{a_0}\psi^J(r), \tag{2.55}$$

which has the formal solution

$$\psi^J(r) = -\left(L^J(r) - \mathscr{L}_{a_0}\right)^{-1}\mathscr{L}_{a_0}\psi^J(r), \tag{2.56}$$

is one of the form

$$O(x)f(x) = g(x), \tag{2.57}$$

for the operator $O(x)$ and the functions $f(x)$ and $g(x)$, with associated Green's function $G(x,x')$.

If the eigenvalues of $\left(L^J(r) - \mathscr{L}_{a_0}\right)$ are defined to be $\frac{2\mu}{\hbar^2}\left(E - E_k^J\right)$, and the eigenvectors are defined to be χ_k^J, then the Green's function of the operator can be written as

$$G^J(r,r') = \frac{\hbar^2}{2\mu}\sum_{k=1}^{\infty}\frac{\chi_k^J(r)\chi_k^J(r')}{E - E_k^J}. \tag{2.58}$$

Note that the eigenvalues can be assumed to be real, since the operator is Hermitian. The definition of the eigenvalues is related to the fact that, since the inner region is a finite, bounded volume, the eigenenergies of the scattering wave equation can only take on discrete values.

The definition of a Green's function $G(x,x')$ [127] for an operator $O(x)$ acting on a function $f(x)$ to produce a function $g(x)$ is one such that

$$f(x) = \int G(x,x')g(x')dx'. \tag{2.59}$$

Hence, one can obtain the formal solution $\psi^J(r)$ of Equation 2.56 via the equation

$$\psi^J(r) = -\int_0^{a_0} G^J(r,r')\mathscr{L}_{a_0}\psi^J(r')dr', \tag{2.60}$$

which, due to the Dirac delta in the definition of $\mathscr{L}_{a_0}$, results in the expression

$$\psi^J(r) = \frac{\hbar^2}{2\mu}\left(\sum_{k=1}^{\infty}\frac{\chi_k^J(r)\chi_k^J(a_0)}{E_k^J - E}\right)\frac{d\psi^J}{dr}\bigg|_{r=a_0}. \tag{2.61}$$

By evaluating this expression at a_0, and multiplying and dividing by a_0, the expression

$$R^J(E,a_0) = \frac{\hbar^2}{2\mu a_0} \sum_{i=k}^{\infty} \frac{\left(\chi_k^J(a_0)\right)^2}{E_k^J - E} \tag{2.62}$$

can be identified with the quantity previously defined as the R-matrix itself. Thus the R-matrix is the Green's function of the operator $\left(L^J(r) - \mathscr{L}_{a_0}\right)$ evaluated at the point a_0. Hence it is possible to write

$$\psi^J(a_0) = a_0 R^J(E,a_0) \left.\frac{d\psi^J}{dr}\right|_{r=a_0}. \tag{2.63}$$

Clearly here the R-matrix is a scalar quantity. It will become a matrix quantity when multiple atomic channels are introduced shortly.

Equation 2.63 shows that the R-matrix can be thought of as the log-derivative of the scattering wavefunction $\psi^J(r)$, evaluated at the inner region boundary a_0. Furthermore, the R-matrix is constructed of the eigenvectors and eigenvalues of the operator $\left(L^J(r) - \mathscr{L}_{a_0}\right)$, which suggests a clear method for calculating this quantity based on a calculation of the eigenvalues and eigenvectors of the Hamiltonian constrained to the inner region.

The computational advantages are also apparent: the computation to obtain the eigenvalues and eigenvectors only needs to be performed once, and then the R-matrix can be computed for a number of scattering energies E at no extra computational expense.

2.2.1.2 The Multichannel Inner Region

The key difference between the single and multichannel cases is the replacement of the PEC $V(r)$ with a matrix of potential energy curves and couplings, $\mathbf{V}(r)$. The elements of the matrix of potentials, $V_{ii'}(r)$, correspond to the elements of the R-matrix itself. The possibility for the scattering event to cause the atoms to transition between atomic channels is what defines the different elements of the R-matrix. This is equivalent to saying their atomic quantum numbers change.

Specifically, the scattering event under consideration is one in which two atoms with a set of quantum numbers i interact with each other, and that interaction causes them to leave the interaction with a set of quantum numbers i', where i and i' may be different. In this work the possibility of the atoms leaving the interaction event as a bonded diatom, or with a different electric charge, is not considered.

Depending on the choice of which quantum numbers to specify as ‘good’, which itself depends on the system being studied, the different elements of the potential matrix (and by association the R-matrix) can have different meanings. This chapter is agnostic to the specific quantum numbers in a specific problem. Channels will be labelled i and i' with no consideration for what i represents. More discussion of the specifics can be found in Chapter 6.

Much of the theory concerning the R-matrix which this discussion is derived from is written from the perspective of electron-atom and electron-molecule scattering [30, 119, 29]. In the multichannel case this leads to considerable differences between the theory that is needed for this work and the written theory, beyond reduced mass terms and reference frames.

Some fundamentals remain the same across the single and multichannel definitions, and the different systems. There is still a time-independent Schrödinger equation:

$$\mathbf{H}^{\Gamma}\mathbf{\Psi}_{k}^{\Gamma} = E_{k}^{\Gamma}\mathbf{\Psi}_{k}^{\Gamma}, \tag{2.64}$$

except now the Hamiltonian $\mathbf{H}^{\Gamma}$ is a matrix quantity, and the scattering wavefunction $\mathbf{\Psi}_{k}^{\Gamma}$ is a vector quantity, where the N_c elements of the vector $\mathbf{\Psi}_{k}^{\Gamma}$ correspond to the N_c different channels i of the interaction. The Hamiltonian contains the potential matrix, along with the matrix of kinetic operators. The specific form of the kinetic matrix will depend on the reference frame one is in, which, as discussed in Chapter 3, will depend on the specific inner region code being used.

Here, k labels the different eigenfunctions of the scattering Hamiltonian, and Γ labels the symmetry of the scattering event by listing all the good quantum numbers. In this work, Γ represents J and τ, the total angular momentum, and the parity of the interaction respectively. Splitting the interaction by symmetry like this is a form of partial wave expansion, which must be consolidated when measuring certain scattering observables, as discussed in Section 2.1.3.

From here the same derivation as in the single channel case can be performed.

The Bloch operator becomes a diagonal matrix with the surface term at a_0 for each channel on the diagonal, and again a Green's function can be found for the operator formed from subtracting the Bloch operator from the Hamiltonian. This Green's function can then be identified again with the R-matrix, such that one can form the equation

$$F_i^\Gamma(a_0) = \frac{\hbar^2}{2\mu}\left(\sum_{i'=1}^{N}\sum_{k=1}^{\infty}\frac{w_{ik}^\Gamma(a_0)w_{i'k}^\Gamma(a_0)}{E_k^\Gamma - E}\right)\left.\frac{dF_{i'}^\Gamma}{dr}\right|_{r=a_0}. \tag{2.65}$$

In this equation, several new quantities have been introduced. The quantity $F_i^\Gamma(r)$ is the *channel function* for a given channel i in a given symmetry Γ – the radial wave function in the outer region for a given channel. Equation 2.65 shows that this quantity is, in general, dependent on contributions from other channels, and one must sum over all the solutions of the scattering Schrödinger equation to obtain it.

The quantity $w_{ik}^\Gamma(a_0)$ is called the *surface amplitude* for a given channel i, solution k, and symmetry Γ, at the inner region boundary a_0. It can be thought of as the contribution from a single channel to the scattering solution k. An explanation of how $w_{ik}^\Gamma(a_0)$ and $F_i^\Gamma(r)$ were obtained in this work will be presented in subsequent chapters.

Equation 2.65 suggests the following definition of an element of the R-matrix which couples channel i to channel i':

$$R_{ii'}^\Gamma(E,a_0) = \frac{\hbar^2}{2\mu a_0}\sum_{k=1}^{\infty}\frac{w_{ik}^\Gamma(a_0)w_{i'k}^\Gamma(a_0)}{E_k^\Gamma - E}, \tag{2.66}$$

which suggests that Equation 2.65 can be written in the form

$$F_i^\Gamma(a_0) = a_0\sum_{i'=1}^{N} R_{ii'}^\Gamma(E,a_0)\left.\frac{dF_{i'}^\Gamma}{dr}\right|_{r=a_0}. \tag{2.67}$$

Equations 2.66 and 2.67 are analogous to the two R-matrix definitions introduced in the last section. The former is a definition based solely on the scattering energy and inner region quantities, and the latter suggests that the R-matrix can be thought of as the log-derivative of the channel function, which is an outer region quantity. This once again demonstrates the R-matrix's role as a connection between the two regions. Note that the R-matrix is symmetric.

At this point in most R-matrix methods a quantity known as the Buttle correction is often introduced [128]. This is an additional term in the R-matrix sum which accounts for the imposition of arbitrary boundary conditions at a_0 which is implicit in the R-matrix method. In this work this correction is not included. This may be the cause of some issues concerning artificial boundary conditions which were confronted in this work. Further discussion of the topic can be found in Chapter 3.

2.2.2 The Outer Region

Equations 2.62 and 2.63, and Equations 2.66 and 2.67 are similar to the definitions of the R-matrix first introduced in the previous chapter. Equation 2.62 is defined in terms of the boundary a_0, the scattering energy, and inner region quantities: eigenvalues and eigenvectors of the Hamiltonian evaluated between $r = 0$ and $r = a_0$ with a Bloch term. Equation 2.63 is presented in terms of the boundary a_0 and an outer region quantity: the scattering wavefunction.

This completes the derivation of the R-matrix in the inner and outer regions. If one wished, one could evaluate the scattering observables at the boundary a_0 using the R-matrix as an input.

However, doing this severely restricts the efficiency and accuracy of the suite of R-matrix methods. Much of the utility of the R-matrix method comes in the form of R-matrix *propagation*. This is when the R-matrix at a_0, $R(E,a_0)$ that one obtains from the inner region calculation is used to obtain a value of the R-matrix at a further distance $r \geq a_0$, $R(E,r)$. This allows one to define a third region, the asymptotic region, at a distance further out than a_0. The point at which one ends the propagation and begins the asymptotic region is known as the propagation distance, a_p, see Figure 1.2. (The derivation of the procedure by which one obtains scattering observables from the R-matrix at any distance $r \geq a_0$ is presented in the next subsection.)

The advantage of evaluating scattering observables at a_p is that more accurate *asymptotic expansions* – approximations to the asymptotic boundary conditions – can be made. If it is being assumed that the potential is zero at the point the scattering observables are being evaluated at, then this approximation gains accuracy the further the point a_p is placed, as the potential decreases in strength monotonically with distance at long range. If the potential is not assumed to be zero, then a type of asymptotic expansion must be used, and most types still rely on the assumption that the potential is small at the distance being evaluated.

There is a large variety of propagator methods in use by those who use R-matrix methods. A propagator takes as its input $R(E,a_0)$ and outputs $R(E,a_p)$. As such, propagators are dependent on E, and a propagation must be repeated for each separate scattering energy.

This is where the true power of the inner/outer region distinction in R-matrix methodology is revealed. The inner region calculation can be performed once to obtain the eigenvalues and eigenvectors, then, for a given value of E, the R-matrix at a_0, $R(E,a_0)$, can be constructed and propagated for relatively minimal computational cost. This means the value of $R(E,a_p)$ can be obtained efficiently for a variety of E values.

R-matrix propagation methods can be compared with wavefunction propagation methods, such as the Numerov method [129]. They operate in a similar way to R-matrix methods, and in the case of the Light-Walker and BBM propagators discussed below, one can even derive wavefunction propagators from the R-matrix propagator. This is useful in e.g. photoassociation calculations [130]. This can be compared to MOLSCAT, where the log-derivative of the wavefunction, and the wavefunction itself, can both be propagated in all circumstances.

Whilst wavefunction propagators *can* be used to obtain scattering observables as a replacement for R-matrix propagators, R-matrix methods have a key advantage in that they tend to be more stable under the propagation. Since the R-matrix is the log-derivative of the wavefunction, any constant factors attached to the wavefunction are cancelled out, meaning that the R-matrix always has a reasonable absolute value. This is crucial in propagation techniques, which have a tendency to amplify small instabilities caused by constant factors [15], leading them to be generally unstable over large propagation distances, and in particular over closed channels.

Two propagation methods were used in this work: Light-Walker propagation [93, 30] and Baluja, Burke and Morgan (BBM) propagation [131, 30]. The single-channel version of the Light-Walker propagator was implemented directly, whilst the single and multichannel BBM propagators were used as part of the PFARM program.

Both methods work by partitioning the outer region into smaller sub-regions. The value of the R-matrix at the end of a sub-region closer to $r = 0$, $R(E, a_s)$, is used to obtain the value of the R-matrix at the farther end, $R(E, a_{s+1})$. Both methods achieve this by constructing a Green's function to construct an equation similar to Equation 2.61 for both ends of the sub-region. These Green's functions can then be used to create an iteration equation to obtain $R(E, a_{s+1})$ from the value of $R(E, a_s)$, allowing one to 'propagate' the R-matrix at a_0 to obtain its value at a_p.

The BBM propagator obtains these Green's functions by treating each sub-region as a 'mini-inner region', and diagonalising a Hermitian operator over this space to obtain eigenvalues and eigenvectors to obtain the Green's function analogous to Equation 2.58 (with an adjustment to the Bloch operator to account for the now two non-zero boundary conditions). For a given sub-region this process is more efficient than the initial inner region calculation because it is over a much smaller range, and so can be achieved with a much smaller matrix diagonalisation.

The Light-Walker propagator obtains the Green's functions by assuming the potential to be constant over the sub-region, avoiding the need for the diagonalisation of the BBM method. The Green's functions then assume standard forms depending on the value of the potential which are straightforward to implement in the iteration equation.

The two methods have relative strengths and weaknesses [30]. For instance, as with the aforementioned pure propagation methods, the need for diagonalisation is avoided. In the Light-Walker case, since the potential is assumed to be unchanging throughout the sub-region, the sub-regions must be made very small to ensure that the propagation is accurate. By contrast, the BBM method can often achieve high accuracy with only a handful of sub-regions.

The BBM method also has the same advantage that the inner region method has in that the diagonalisations need only be carried out once before being re-applied to many scattering energies [30], which means they are partially (but not entirely) energy-independent.

There are also some methods which allow the step size in the Light-Walker method to be dynamically varied based on the (simple numerical) derivative of the potential at the point a_s [132] to ensure that the step size is sufficiently small in regions where the potential changes rapidly, whilst being efficient in regions where the potential is varying slowly. This is discussed further in Chapter 3.

2.2.2.1 The Single Channel Outer Region

The Light-Walker propagator assumes a constant potential over the sub-region $a_{s-1} < r < a_s$. The width of this region is controlled by the numerical parameter N_p, the number of iterations used in the propagator. If the length between the points a_p and a_0 is divided into N_p sub-regions, then the size of each sub-region, $(a_s - a_{s-1})$, will be $(a_p - a_0)$ divided by N_p.

For a given symmetry J, for a given sub-regon a_s, the quantity λ_s is defined such that

$$\lambda_s^2 = k^2 - \frac{2\mu}{\hbar^2} V^J(a_s), \tag{2.68}$$

where k^2 is the scattering wavenumber as before, $V^J(a_s)$ is the potential with the angular momentum term included, and the approximation is made that $V^J(a_{s-1}) = V^J(a_s)$. The symmetry labels are not explicitly included in this derivation.

Using similar arguments as presented in the single-channel inner region derivation above [30], Green's functions can be derived for the formal solution to the scattering Schrödinger equation in this region. Unlike in the inner region, Green's functions must be formed at both ends of the finite region in question in order to produce the iteration equation. Also unlike in the inner region, the Bloch operator that must be included to construct these Green's functions now has two terms – one for each non-zero boundary condition at the two ends of the finite region:

$$\mathscr{L}_{a_s} = \delta(r - a_s)\frac{d}{dr} - \delta(r - a_{s-1})\frac{d}{dr}. \tag{2.69}$$

A separate complication is that the possibility is now introduced that $\lambda_s^2 < 0$, i.e. that the scattering energy is lower than that of the potential, implying the system is bound (similar to the extension of the k-coordinate to complex values when studying S-matrix poles). This is a consideration that must be made when exploring systems with closed channels.

Thus there are four Green's functions to consider. For $\lambda_s^2 > 0$, the functions have the following form:

$$G_s(r,r') = \frac{-1}{\lambda_s \sin(\lambda_s \delta a_s)} \times \begin{cases} \cos(\lambda_s(r'-a_s))\cos(\lambda_s(r-a_{s-1})) & a_{s-1} \leq r \leq r' \\ \cos(\lambda_s(r-a_s))\cos(\lambda_s^J(r'-a_{s-1})) & r' \leq r \leq a_s \end{cases}. \tag{2.70}$$

When $\lambda_s^2 < 0$, then the quantity μ_s can be defined such that $\mu_s^2 = -\lambda_s^2$, and the Green's functions have the following form:

$$G_s(r,r') = \frac{-1}{\mu_s \sinh(\mu_s \delta a_s)} \times \begin{cases} \cosh(\mu_s(r'-a_s))\cosh(\mu_s(r-a_{s-1})) & a_{s-1} \leq r \leq r' \\ \cosh(\mu_s(r-a_s))\cosh(\mu_s^J(r'-a_{s-1})) & r' \leq r \leq a_s \end{cases}. \tag{2.71}$$

In all these cases, the quantity δa_s is defined such that $\delta a_s = a_s - a_{s-1}$.

As in the inner region case, these Green's functions can then be used with the formal solution to the scattering wavefunction equation to produce an expression for the R-matrix. Here it can be used to create an iteration equation which provides the value of the R-matrix for a given symmetry and scattering energy at a_s, R_s, as a function of the value of the R-matrix for that symmetry and scattering energy at R_{s-1} [30]:

$$R_s = \frac{1}{a_s}\left(G_s(a_s,a_s) - \frac{G_s(a_s,a_{s-1})G_s(a_{s-1},a_s)}{(G_s(a_{s-1},a_{s-1}) + a_{s-1}R_{s-1})}\right). \tag{2.72}$$

In the single-channel, $J = 0$ case, this equation reduces down to one iteration equation:

$$R_s = \frac{-1}{a_s\lambda_s}\left(\frac{1}{\tan(\lambda_s\delta a)} + \frac{2}{\sin(2\lambda_s\delta a)}\left(a_{s-1}R_{s-1}\lambda_s\tan(\lambda_s\delta a) - 1\right)^{-1}\right), \tag{2.73}$$

where R_s is the value of the R-matrix at each iteration step (beginning at R_{a_0}), $\delta_a = a_s - a_{s-1}$, and λ_s^2 is replaced with μ_s^2 when $\lambda_s^2 < 0$.

Equation 2.72 also applies to the BBM propagator [30] – the only difference is the value of the Green's function that is used in it. Here the Green's function has the same form as in Equation 2.58, with the adjustment that the functions $\chi_k^J(r)$ and energies E_i^J are now replaced with $\chi_k^s(r)$ and E_i^s (with the symmetry label J still persisting, but not explicitly included in the new expressions). The s denotes that these functions and energies only exist within a given sub-region $a_{s-1} < r < a_s$, and are formed by diagonalising the operator formed by subtracting the Bloch operator defined in Equation 2.69 from the Schrödinger equation within this region.

2.2.2.2 The Multichannel Outer Region

In the multichannel case, the Light-Walker propagator is constructed (following the derivation by Burke [30] based on the derivation by Schneider & Walker [133]) by diagonalising the following matrix:

$$\mathscr{V}(r) = \mathbf{V}^J(r) - \mathbf{E} + E\mathbf{I}, \tag{2.74}$$

where $\mathbf{I}$ is the identity matrix, E is the scattering energy, $\mathbf{E}$ is the diagonal matrix of eigenenergies (not to be confused with the scattering energy), and $\mathbf{V}^J(r)$ is the (in general) non-diagonal matrix of potentials for each channel, including channel coupling elements (defined properly below in Equation 2.90 – note the J-dependence).

As in the single channel case, the general symmetry labels are suppressed. In the single channel case, only the J symmetry was considered. In the multi-channel case the general symmetry label would be Γ, which would include J, along with parity, τ, the other conserved quantity.

The version of this matrix which has been evaluated at a_s and diagonalised is called $\mathbf{v}_s^2$, and the matrix which diagonalises it is called $\mathbf{O}_s$:

$$\mathbf{O}_s^T \mathscr{V} \mathbf{O}_s = \mathbf{v}_s^2. \tag{2.75}$$

From this the real, diagonal matrix $\boldsymbol{\lambda}_s$ can be defined in the following way:

$$\boldsymbol{\lambda}_s^2 = \frac{2\mu}{\hbar^2}\left(E\mathbf{I} - \mathbf{v}_s^2\right). \tag{2.76}$$

This equation is, of course, in analogy with Equation 2.68. The elements of the matrix are λ_{is}. This suggests that the elements $\mathscr{G}_{is}$ of the diagonal matrix $\mathscr{G}_s$ for when $\lambda_{is}^2 > 0$ can be defined in the following way in analogy with Equation 2.71:

$$\mathscr{G}_{is}(r,r') = \frac{-1}{\lambda_{is}\sin(\lambda_{is}\delta a_s)} \times \begin{cases} \cos(\lambda_{is}(r'-a_s))\cos(\lambda_{is}(r-a_{s-1})) & a_{s-1} \le r \le r' \\ \cos(\lambda_{is}(r-a_s))\cos(\lambda_{is}(r'-a_{s-1})) & r' \le r \le a_s \end{cases}, \tag{2.77}$$

and in the following way when $\lambda_{is}^2 < 0$ such that $\mu_{is}^2 = -\lambda_{is}^2$ (which corresponds to a closed channel):

$$\mathscr{G}_{is}(r,r') = \frac{-1}{\mu_{is}\sin(\mu_{is}\delta a_s)} \times \begin{cases} \cos(\mu_{is}(r'-a_s))\cos(\mu_{is}(r-a_{s-1})) & a_{s-1} \le r \le r' \\ \cos(\mu_{is}(r-a_s))\cos(\mu_{is}(r'-a_{s-1})) & r' \le r \le a_s \end{cases}, \tag{2.78}$$

where in all cases $\delta a_s = a_s - a_{s-1}$.

Then, defining $\mathbf{G}_s(r,r')$ as

$$\mathbf{G}_s(r,r') = \mathbf{O}_s \mathscr{G} \mathbf{O}_s^T, \tag{2.79}$$

one can then write down the expression for the propagation equation equivalent to

Equation 2.72:

$$a_s \mathbf{R}_s = \mathbf{G}_s(a_s, a_s) - \mathbf{G}_s(a_s, a_{s-1}) \left(\mathbf{G}_s(a_{s-1}, a_{s-1}) + a_{s-1}\mathbf{R}_{s-1}\right)^{-1} \mathbf{G}_s(a_{s-1}, a_s). \tag{2.80}$$

The BBM propagator has a similar multichannel derivation – the iteration equation is the same as Equation 2.80, but the Green's functions are replaced with a multichannel, analogous version of Equation 2.58.

2.2.3 The Asymptotic Region

The final step needed before the scattering observables can be obtained is the calculation of a quantity called the K-matrix. All of the scattering observables of interest can be defined using this quantity. There are several methods for obtaining the K-matrix, each representing a different level of approximation.

In Section 2.1.3 the K-matrix was introduced as relating to the tangent of a quantity known as the eigenphase (in the single channel case it was precisely the tangent of the eigenphase). Here it will be shown how the K-matrix can be expressed as a function of the R-matrix and thus how scattering observables can be obtained from the R-matrix.

2.2.3.1 The Single Channel Asymptotic Region

In the single channel case, the K-matrix for a given symmetry J is a scalar quantity $K^J(k)$ which depends on the scattering energy (which can be represented either as the energy E or the scattering wavenumber k).

The form of the K-matrix depends on the choice of asymptotic boundary conditions. The simplest case is when it is assumed that beyond a certain point in space a_p the potentials are all zero. In that case, the asymptotic boundary conditions that can be assumed are the ones in Equations 2.10 and 2.11 for $J = 0$ and $J > 0$ respectively.

In this case, by assuming that the K-matrix $K^J(k)$ is equal to the $\tan\left(\delta^J(k)\right)$ term in the boundary conditions, the value of the K-matrix at the asymptotic distance a_p can be shown to be

$$K^J(k) = \frac{-s_J(ka_p) - R^J(E,a_p)ka_p s'_J(ka_p)}{c_J(ka_p) - R^J(E,a_p)ka_p c'_J(ka_p)}, \tag{2.81}$$

where $s_J(x)$ and $c_J(x)$ are the modified spherical Bessel and Neumann functions defined by Equations 2.12 and 2.13 respectively, and $s'_J(x)$ and $c'_J(x)$ are their respective derivatives with respect to x.

This expression can be obtained by utilising the definition of the R-matrix as the log-derivative:

$$\psi^J(a_p) = a_p R^J(E,a_p) \left.\frac{d\psi^J}{dr}\right|_{r=a_p}. \tag{2.82}$$

The derivative of the asymptotic boundary condition that $\psi^J(r)$ obeys is

$$\frac{d\psi^J}{dr} = ks'_J(kr) + kc'_J(kr)K^J(k). \tag{2.83}$$

This suggests that

$$s_J(ka_p) + c_J(ka_p)K^J(k) = ka_p R^J(E,a_p)\left(s'_J(ka_p) + c'_J(ka_p)K^J(k)\right), \tag{2.84}$$

which can be rearranged to obtain Equation 2.81.

When $J = 0$ this expression for the K-matrix reduces to the much simpler form:

$$K^0(k) = -\frac{\sin(ka_p) - Rka_p\cos(ka_p)}{\cos(ka_p) + Rka_p\sin(ka_p)}, \tag{2.85}$$

where $R = R^0(E,a_p)$. This can also be written as

$$K^0(k) = \frac{Rka_p - \tan ka_p}{1 + Rka_p \tan ka_p}. \tag{2.86}$$

A better approximation can be achieved by assuming that the potential is not zero at a_p, but some small value. This is where a so-called *asymptotic expansion* is used, such as the one constructed by Burke & Schey [134].

2.2.3.2 The Multichannel Asymptotic Region

The asymptotic boundary conditions introduced in Equations 2.10 and 2.11 are one instance of a general trend: asymptotic boundary conditions are always composed of a 'sine-like' and a 'cosine-like' function, or vector in the multichannel case, with the latter term multiplied by the K-matrix.

Following on from the introduction in Section 2.1.2, when the potential is assumed to be zero at asymptotic distances, the multichannel version of these sine- and cosine-like functions are simply sines and cosines:

$$F_{i\eta}^{\Gamma}(r \to \infty) = \frac{1}{\sqrt{k_i}} \left(\sin\left(k_i r\right) + \sum_j K_{ij}^{\Gamma}(k) \cos\left(k_j r\right) \right), \tag{2.87}$$

where the Γ label is composed of conserved quantities total angular momentum J and parity τ, K_{ij}^{Γ} is the element of the K-matrix, $F_{i\eta}^{\Gamma}$ is the reduced radial wavefunction for channel i and scattering solution η, as introduced in Section 2.2.1.2, and k_i is given by Equation 2.15.

When performing an asymptotic expansion, it is assumed that the potential is non-zero at asymptotic distances, and so the asymptotic boundary conditions are modified by the presence of the potential. In general, the vector of channel functions $\mathbf{F}^{\Gamma}$ obeys the boundary condition

$$\mathbf{F}^{\Gamma}(r \to \infty) = \mathbf{s}_{\Gamma}(k,r) + \mathbf{K}^{\Gamma}(k)\mathbf{c}_{\Gamma}(k,r), \tag{2.88}$$

where $\mathbf{s}_{\Gamma}(k,r)$ and $\mathbf{c}_{\Gamma}(k,r)$ are vectors of sine- and cosine-like functions, respectively, whose forms depend on the specific asymptotic expansion being utilised.

In both the zero and non-zero potential cases, the K-matrix can be expressed as a function of the R-matrix, a_p, the $\mathbf{s}_{\Gamma}(k,r)$ and $\mathbf{c}_{\Gamma}(k,r)$ vectors, and their derivatives $\mathbf{s}_{\Gamma}'(k,r)$ and $\mathbf{c}_{\Gamma}'(k,r)$, using the multichannel equivalent of the derivation outlined in Section 2.2.3.1.

The potential can be introduced by considering the Schrödinger equation. In the outer and asymptotic regions the channel function obeys the following

Schrödinger equation:

$$\left(\frac{d^2}{dr^2}+k_i^2\right)F_i^\Gamma=\frac{2\mu}{\hbar^2}\sum_{i'=1}^{N_a}V_{ii'}^\Gamma(r)F_{i'}^\Gamma(r), \tag{2.89}$$

where N_a is the number of open channels – the number of channels with energies lower than the scattering energy.

As mentioned previously, the K-matrix has dimensions $N_a \times N_a$. However, since closed channels are propagated, as discussed in the previous section, it is possible for them to influence the physics of the scattering observables produced for the open channels. This is how it is possible for one to obtain Feshbach resonances, where the presence of a closed channel affects the cross-section of an open channel that it is coupled to by a potential term. Closed channels are not explicitly included in the asymptotic expansions, however.

In this work the potentials and the couplings between them are always assumed to be either constants or central potentials composed of finite sums of powers of r^{-1}:

$$V_{ii'}^\Gamma(r)\sum_{\lambda=1}^{\lambda_{max}}a_{\lambda ii'}^\Gamma r^{-\lambda}, \tag{2.90}$$

for a given symmetry (with the angular momentum term included in $V_{ii'}^\Gamma(r)$), and where the coefficients $a_{\lambda ii'}$ are obtained from literature sources. The exception to this is the consideration of Morse potentials below and in Chapter 4. Note that in general λ_{max} can vary for different channels. The coefficients are utilised in the construction of the sine- and cosine-like functions in the K-matrix.

The asymptotic expansions used in this work are the ones implemented in PFARM [94]. Similar to the aforementioned attempt made to implement the Light-Walker propagator, an attempt was made to directly implement the Burke-Schey expansion [134]. The derivation of the Burke-Schey asymptotic expansion is presented below. PFARM uses the Gailitis asymptotic expansion, which is a modification of the Burke-Schey expansion [135].

The Burke-Schey asymptotic expansion follows from a specific version of

Equation 2.88 [134]. In the Burke-Schey expansion, the vectors $\mathbf{s}_\Gamma$ and $\mathbf{c}_\Gamma$ have the following forms:

$$s_{i\Gamma} = A_i^\Gamma \cdot \sin(k_i r), \quad c_{i\Gamma} = B_i^\Gamma \cdot \cos(k_i r) \tag{2.91}$$

where

$$A_i^\Gamma = \sum_{p=0}^{p_{\max}} \alpha_{pi}^\Gamma r^{-p}, \quad B_i^\Gamma = \sum_{p=0}^{p_{\max}} \beta_{pi}^\Gamma r^{-p}. \tag{2.92}$$

The α_{pi}^Γ and β_{pi}^Γ coefficients are obtained from the following interdependent recurrence relations:

$$((p-1)(p-2) - J(J+1))\alpha_{p-2,i}^\Gamma + 2k_i(p-1)\beta_{p-1,i}^\Gamma = \sum_{i'=1}^{N} \sum_{\lambda=1}^{\lambda_{\max}} a_{ii'\lambda}^\Gamma \alpha_{p-\lambda-1,'}^\Gamma, \tag{2.93}$$

and

$$((p-1)(p-2) - J(J+1))\beta_{p-2,i}^\Gamma - 2k_i(p-1)\alpha_{p-1,i}^\Gamma = \sum_{i'=1}^{N} \sum_{\lambda=1}^{\lambda_{\max}} a_{ii'\lambda}^\Gamma \beta_{p-\lambda-1,i'}^\Gamma, \tag{2.94}$$

where N_a is the number of open channels and $\lambda_{\max}$ is the largest value of λ (with larger values chosen increasing accuracy and computation time). The derivatives of the $\mathbf{s}_\Gamma$ and $\mathbf{c}_\Gamma$ vectors also have related recurrence relations, which can be derived by differentiating their power expansions.

The recurrence relations are initialised by assuming that all α_{pi}^Γ and β_{pi}^Γ are zero for $p < 0$, and that for all i values,

$$\alpha_{0i}^\Gamma = \beta_{0i}^\Gamma = 1. \tag{2.95}$$

Finally, the coefficients obtained from the recurrence relations are used to construct the asymptotic expansion. This expansion is combined with the R-matrix to form the K-matrix. From this K-matrix the eigenphases are obtained, and from the eigenphases the cross-sections are obtained.

The Gailitis asymptotic expansion modifies the Burke-Schey asymptotic expansion by replacing the sine- and cosine-like functions with Coulomb functions where needed [135], and by utilising Padé expansions. The derivation then follows from there in a similar manner to above, and a different recurrence relation is derived to obtain the coefficients of the vectors.

One improvement the Gailitis expansion has over the Burke-Schey expansion is that because it utilises Coulomb functions, it is better suited to handling closed channels. Another improvement is that the Padé expansions it uses improve the convergence of the iteration methods.

Both the Burke-Schey and Gailitis expansions allow for the possibility of explicitly including closed channels in the scattering observables. In order to include them, one would introduce a separate matrix $\mathbf{L}^{\Gamma}$ that has dimensions $N_b \times N_a$, where N_b is the number of *closed* channels. Furthermore, instead of assuming that the closed channels' wavefunctions have zero amplitude, one can instead assume that they have an exponentially decaying form, in analogy with the sine- and cosine-like asymptotic forms for open channels. In this work, however, the exponentially decaying asymptotic boundary conditions are not used, and the closed channels wavefunctions are simply assumed to be zero at sufficient distance. All methods used and results obtained were for K-matrices with $N_a \times N_a$ elements.

2.3 Analytic Scattering

In order to assess the accuracy of the scattering observables derived by the new algorithm proposed here, it it necessary to compare the results to some benchmarks. In Chapter 5 and Chapter 6, the results produced in this work will be compared to published results, such as Myatt *et al.* and Krems & Buchachenko [136, 137]. However during the construction of the algorithm it was found to be useful to compare the results to simpler, analytic results. The analytic results chosen were those associated with the Morse potential [106].

2.3.1 The Morse Potential

The reason the Morse potential [106] was selected was because it can be considered the simplest model of a diatomic potential energy curve which captures all of the features seen in realistic ones: it has a strong repulsive barrier at small distances, a well-defined minimum, and a tail which tends to zero from below at large distances (Figure 2.2). It is even possible to add a centrifugal barrier by adding an angular momentum term, such as the J term seen in Equation 2.49.

Many simple models of diatoms use the Morse potential, and many more modern and accurate models use extensions to the Morse potential, such as the popular Morse/long-range potential [138]. One key difference between the Morse potential and more realistic potential energy curves is the fact that the Morse potential dies off exponentially at asymptotic values of the internuclear separation, whereas more realistic curves will die off polynomially (physically, the tail of the curve is caused by van der Waals interactions, dispersion forces, and other weaker multipole interactions which scale as r^n for $n < -1$).

Another useful feature of the Morse potential is that the Schrödinger equation with a Morse potential is analytically soluble. As will be shown below, this implies that analytic scattering observables can be constructed. This further implies that numerical scattering results obtained from the algorithm proposed here can be compared to results with no error for a given system. Unfortunately, this is only true for $J = 0$ potentials, as no analytic solutions exist for the Schrödinger equation with a Morse potential with non-zero J.

The Morse potential with no centrifugal term has the algebraic form:

$$V(r) = D_e\left(\left(1 - e^{-a(r-r_e)}\right)^2 - 1\right), \tag{2.96}$$

where D_e is the dissociation energy or well depth (assuming the zero of potential energy is placed at the dissociation energy), r_e is the equilibrium position, or position of the well minimum, and a is a scaling parameter (the so-called Morse parameter) affecting the shape of the well. The specific Morse potential used in much of the testing of the main algorithm is presented in Figure 2.2.

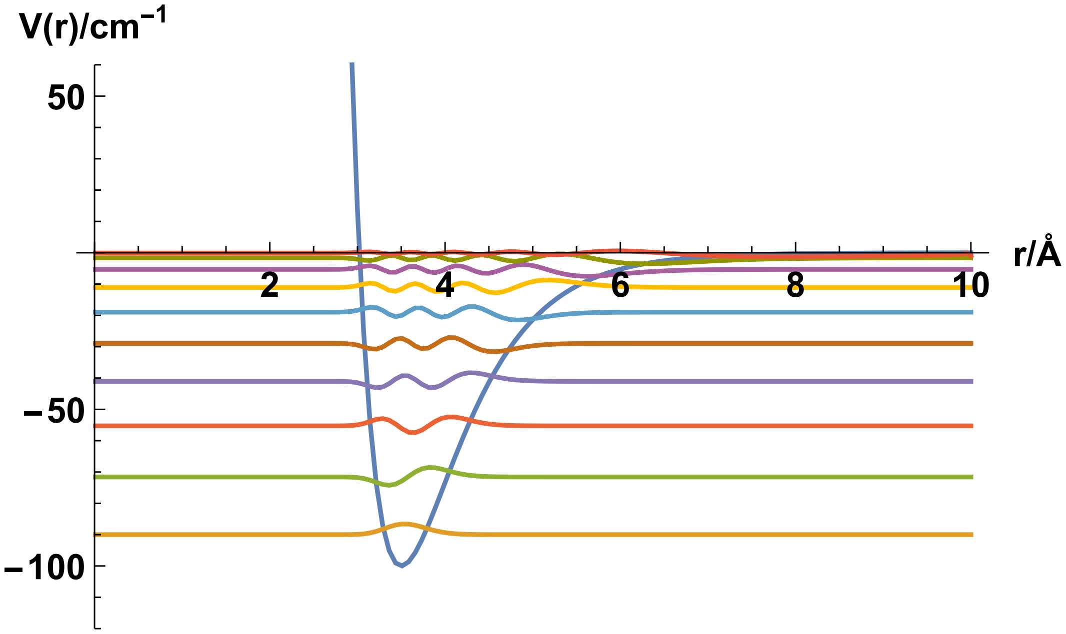

Figure 2.2: The Morse potential with $D_e = 100\,\mathrm{cm}^{-1}$, $a = 1.451455517\,\text{Å}^{-1}$, $r_e = 3.5\,\text{Å}$, and associated bound states.

The analytic eigenenergies E_n^{Morse} and eigenfunctions Ψ_n^{Morse} of the Morse potential are known [106]. For the radial time-independent Schrödinger equation,

$$\left(-\frac{\hbar^2}{2m}\frac{d^2}{dr^2} + D_e e^{-2a_{\mathrm{Morse}}(r-r_e)} - 2D_e e^{-a_{\mathrm{Morse}}(r-r_e)}\right)\Psi_n = E_n\Psi_n, \tag{2.97}$$

the bound eigenenergies E_n and eigenfunctions Ψ_n are given by [106]:

$$E_n^{\mathrm{Morse}} = -D_e + 2a_{\mathrm{Morse}}\sqrt{\frac{D_e\hbar^2}{2\mu}}\left(n+\frac{1}{2}\right) - \frac{1}{4D_e}\left(2a_{\mathrm{Morse}}\sqrt{\frac{D_e\hbar^2}{2\mu}}\left(n+\frac{1}{2}\right)\right)^2, \tag{2.98}$$

and

$$\Psi_n^{\mathrm{Morse}} = N_n z^{(1/(a_{\mathrm{Morse}}r_0)-n-1/2)} \exp\left(\frac{-z}{2}\right) L_n^{(2/(a_{\mathrm{Morse}}r_0)-2n-1)}(z), \tag{2.99}$$

where $L_n^{(\alpha)}(z)$ is the n^{th} associated Laguerre polynomial [109], and N_n is a normalising factor given by

$$N_n = \left(\frac{\left(\frac{2}{a_{\mathrm{Morse}} r_0} - 2n - 1 \right) a_{\mathrm{Morse}} \Gamma(n+1)}{\Gamma\left(\frac{2}{a_{\mathrm{Morse}} r_0} - n \right)} \right)^{\frac{1}{2}}, \tag{2.100}$$

where $\Gamma(x)$ is the standard Gamma function.

Similar to Equation 2.97, for a scattering event between particles with reduced mass μ with energy E interacting over a Morse potential, the radial wavefunction $\Psi(r)$ is given by the time-independent radial Schrödinger equation:

$$\left(-\frac{\hbar^2}{2\mu} \frac{d^2}{dr^2} + D_e e^{-2a_{\mathrm{Morse}}(r-r_e)} - 2D_e e^{-a_{\mathrm{Morse}}(r-r_e)} \right) \psi = E\psi. \tag{2.101}$$

$\psi(r)$ must obey the same asymptotic boundary conditions as in Equation 2.10.

One can define

$$r_0 = \sqrt{\frac{\hbar^2}{2\mu D_e}}, \tag{2.102}$$

$$z(r) = \frac{2}{a_{\mathrm{Morse}} r_0} e^{-a(r-r_e)}, \tag{2.103}$$

and

$$\Phi(z) = z^{\frac{1}{2}} \psi(z), \tag{2.104}$$

and as a consequence it can be shown [139] that Equation 2.101 can be re-written as

$$\frac{d^2\Phi}{dz^2} + \left(-\frac{1}{4} + \frac{1}{a_{\mathrm{Morse}} r_0 z} + \frac{\frac{1}{4} + \left(\frac{k}{a_{\mathrm{Morse}}} \right)^2}{z^2} \right) \Phi(z) = 0. \tag{2.105}$$

In this form, the equation is equivalent to the well-known Whittaker equation, whose solutions are the Whittaker functions. There are two linearly independent solutions to Equation 2.105:

$$\psi_\pm(z) = e^{-z/2} z^{\pm ik/a_{\mathrm{Morse}}} {}_1F_1\left(\frac{1}{2} - \frac{1}{a_{\mathrm{Morse}} r_0} \pm \frac{ik}{a_{\mathrm{Morse}}}, 1 \pm \frac{2ik}{a_{\mathrm{Morse}}}; z \right), \tag{2.106}$$

where ${}_1F_1(x,y;z)$ is the Kummer confluent hypergeometric function of the first kind [140], and the $\psi_{\pm}(z)$ functions represent incoming and outgoing waves.

Using the results for the analytic scattering wavefunctions of the Morse potential in Equation 2.106, it is possible to construct an analytic equation for the eigenphase $\delta(k)$ associated with scattering with the Morse potential.

The derivation below follows that of Rawitscher *et al.* [139] and Selg [141, 142].

The general solution $\psi(r)$ to Equation 2.101 can be written in terms of the two solutions to Equation 2.105, which are given by Equation 2.106, such that:

$$\psi(r) = C_+\psi_+(r) + C_-\psi_-(r), \tag{2.107}$$

where $C_{\pm}$ are two constants.

There are two boundary conditions on $\psi(r)$ that can be used to obtain an expression for the eigenphase, given by Equation 2.10. As $r \to \infty$, $z \to 0$. This means that due to a property of the Kummer confluent hypergeometric functions, both hypergeometric functions tend to 1 as $r \to \infty$.

The S-matrix is introduced in Section 2.1.3, where it is said that it can be defined as a ratio of plane wave coefficients [30]. Here this concept becomes useful because by defining z_0 such that

$$z(r=0) = z_0 = \frac{2}{a_{\text{Morse}} r_0} e^{ar_e}, \tag{2.108}$$

the following expression can be obtained:

$$\left(\frac{z}{z_0}\right)^{\pm \frac{ik}{a_{\text{Morse}}}} = e^{\mp ikr}, \tag{2.109}$$

which can then be combined with the boundary conditions and Equation 2.108. Doing this, one can obtain an expression for the ratio of the coefficients of $\psi_{\pm}$ in this limit, and hence one can obtain an analytic expression for the S-matrix:

$$S(k) = \lim_{r\to\infty} \frac{C_+}{C_-} = \frac{{}_1F_1\left(\frac{1}{2} - \frac{1}{a_{\text{Morse}} r_0} + \frac{ik}{a_{\text{Morse}}}, 1 + \frac{2ik}{a_{\text{Morse}}}; z_0\right)}{{}_1F_1\left(\frac{1}{2} - \frac{1}{a_{\text{Morse}} r_0} - \frac{ik}{a_{\text{Morse}}}, 1 - \frac{2ik}{a_{\text{Morse}}}; z_0\right)}. \tag{2.110}$$

Another way of defining the eigenphase is as the argument of the S-matrix, such that:

$$S(k) = e^{2i\delta(k)}. \tag{2.111}$$

Note that, as discussed in Section 2.1.3, the factor of 2 in the exponent is arbitrary, and other authors define it differently, depending on whether the eigenphase is defined as the argument of the S-matrix (as Selg does [141]), or as the arctangent of the K-matrix, which is equivalent to defining the eigenphase to be half of the argument of the S-matrix (as in this work, and in the work of Rawitscher *et al.* [139]).

The analytic expression for the eigenphase is then given by:

$$\delta(k) = \frac{1}{2} \arg\left(\frac{{}_1F_1\left(\frac{1}{2} - \frac{1}{a_{\text{Morse}} r_0} + \frac{ik}{a_{\text{Morse}}}, 1 + \frac{2ik}{a_{\text{Morse}}}; z_0\right)}{{}_1F_1\left(\frac{1}{2} - \frac{1}{a_{\text{Morse}} r_0} - \frac{ik}{a_{\text{Morse}}}, 1 - \frac{2ik}{a_{\text{Morse}}}; z_0\right)}\right). \tag{2.112}$$

This expression can then be compared to numerical results generated using the R-matrix method.

Whilst the expression is analytically correct, and it produces values between $-\frac{\pi}{2}$ and $\frac{\pi}{2}$ as expected for an arctangent, issues may arise when evaluating this expression computationally. This is because some of the intermediate numbers, most notably the hypergeometric ${}_1F_1$ functions, can have extremely large values when using typical values for Morse parameters. This may be difficult for computers to process. For instance, for the argon dimer Morse potential assessed in Chapter 4, typical values of k lead to ${}_1F_1$ values whose magnitude are approximately 10^{1330}. It would clearly be desirable to avoid these large numbers in any numerical computation.

As such, an alternate expression can be used, based on an identity from [109]:

$$e^{x}{}_1F_1(a;b;-x) = {}_1F_1(b-a;b;x). \tag{2.113}$$

When Equation 2.112 is re-written using this identity, it becomes

$$\delta(k) = \frac{1}{2}\arg\left(\frac{{}_1F_1(\frac{1}{2}+\frac{1}{a_{Morse}r_0}+\frac{ik}{a_{Morse}};1+\frac{2ik}{a_{Morse}};-z_0)}{{}_1F_1(\frac{1}{2}+\frac{1}{a_{Morse}r_0}-\frac{ik}{a_{Morse}};1-\frac{2ik}{a_{Morse}};-z_0)}\right). \tag{2.114}$$

This expression produces the same values as Equation 2.112, however the intermediate values used in the calculation (specifically the ${}_1F_1$ values evaulated) are significantly smaller. For the argon Morse dimer example as above, the magnitudes are more typically of the order of 10^{-31}, which is much more manageable for libraries in various programming languages that handle hypergeometric functions.

Chapter 3

Methods

This chapter presents a description of the RmatReact method developed in this work, several variants of which were used to produce the results presented in the subsequent results chapters. The methods presented here are a combination of new software written for this project, and adaptations of pre-existing software written for use in other problems. The pre-existing softwares, specifically DUO [86] and PFARM [94], were modified to accommodate the physical processes studied in this work. DUO is a general-purpose diatomic nuclear motion code, originally designed to produce high-accuracy diatomic spectra, with a particular emphasis on open-shell systems. PFARM is an R-matrix propagation code designed to produce scattering observables for electron-atom and electron-ion collisions, with specific applications to the UKRmol program suite [67]. The modifications made to these codes are described in this chapter. The program reskit [143], an S-matrix pole-finding software, was also used without modification.

In the case of all three of these programs, code was also written to duplicate their functionality for testing purposes, and code was written to interface between them. The integrated development environment (IDE) used to write the C++ code was Microsoft Visual Studio.

As described in the previous chapters, the RmatReact method is based on solving the Schrödinger equation over the finite space of the inner region, then evaluating the solutions of the Schrödinger equation on the boundary to obtain an R-matrix, then propagating that R-matrix to an asymptotic distance, and matching certain boundary conditions at that distance, to obtain scattering observables.

In this work, DUO was used to solve the inner region Schrödinger equation, PFARM was used to propagate the R-matrix in the outer region, and a 'harness' code was used to transfer the results of the former into the latter, and process the observables produced by the latter. The code reskit was also used to construct and study S-matrices obtained from the results produced by PFARM. The diatomic code LEVEL [88], which has similar functionality to DUO, was also used for testing purposes at various stages of the project.

Alongside descriptions of the codes used and created in this work, a description is provided of the quadrature methods at the heart of DUO, as significant work was done on researching improved quadratures for use in the modified version of DUO.

3.1 Gaussian Quadratures

One expensive step of the algorithm is the solving of the Schrödinger equation in the inner region. In cases where no analytic solutions exist, such as this work, solving the Schrödinger equation is, at its heart, a numerical integration problem. In standard numerical methods, this is translated into the linear algebra problem of a matrix diagonalisation, which has been highly optimised over the years.

There are particularities about this problem, however, which mean many standard methods are unsuitable. For instance, the fact that the Schrödinger equation is being solved over a finite region of space is a concern for many standard methods. The solution method employed here is a Discrete Variable Representation (DVR), which will be defined shortly.

DVRs are usually based on Gaussian quadratures, a general name for a family of numerical integration methods, which has been studied for many years (e.g. [144, 145, 146]). These techniques are based on the zeroes of different polynomials, such as Chebyshev polynomials [147], and Legendre polynomials [148].

Among the first applications of DVR methods to quantum mechanical problems was a DVR method based on Hermite polynomials [149, 150, 151], which is notable as Hermite polynomials are, of course, the analytic solutions to the

Schrödinger equation with a harmonic oscillator potential. Analogies like these can be exploited. For instance, the radial basis sets used in DVR3D [89] are based on associated Laguerre polynomials [109], which is noteworthy as these polynomials are the exact solutions to the Schrödinger equation with a Morse potential, as seen in Chapter 2.

Gaussian quadratures form a key part of the algorithm as a whole, and as such it is important to explain them in detail here. This will also help to explain how DVR methods in quantum chemistry work. Much of the following is taken from *Approximate calculations of integrals*, by V. I. Krylov [152].

In order to explain how Gaussian quadratures work, first a function, $f(r)$, is defined. The objective is to integrate this function over the range $[a,b]$. When performing a Gaussian quadrature, a set of grid points r_k and associated weights w_k are determined such that the following equation holds:

$$\int_a^b f(r)dr \approx \sum_{k=1}^{m} w_k f(r_k), \tag{3.1}$$

where the k sums over the grid points r_k which all lie in the region $[a,b]$ $(0 \leq a \leq b)$. The order of the quadrature is m, which is the number of grid points. The error in this approximation is related to the value of m, with higher values corresponding to better approximations for well-behaved functions. Indeed, if $f(r)$ is a polynomial, the approximation becomes exact if m is larger than the highest degree of the polynomial (implying that the better a given function can be approximated by a polynomial the lower the error will be).

Sometimes the behaviour of the quadrature method is improved by including a *weight function*, $p(r)$, in the integral, which modifies the grid points and weights one ends up choosing. When that happens, the integral ends up looking like:

$$\int_a^b p(r)g(r)dr \approx \sum_{k=1}^{m} w_k g(r_k). \tag{3.2}$$

Note that it is always possible to include a weight function by defining the function $g(r)$ such that $f(r) = p(r)g(r)$. This can lead to numerical problems if dividing by $p(r)$ introduces singularities in the $[a,b]$ range, as is sometimes the case.

The optimum grid points and weights for a given weight function, and for a given accuracy (i.e. for a given value of m) are determined by defining the polynomial $\omega(r)$ such that:

$$\omega(r) = (r - r_1)(r - r_2)\dots(r - r_m), \tag{3.3}$$

and by specifying that $\omega(r)$ satisfy the conditions of being orthogonal (with respect to $p(r)$ over the region $[a,b]$) to any polynomial $Q(r)$ with a degree less than m, such that:

$$\int_a^b p(r)\omega(r)Q(r)dr = 0. \tag{3.4}$$

Under this condition, and with this definition, the polynomial can be specified up to a constant factor, and its roots can be found. A polynomial $P_m(r)$ is defined, which differs from $\omega(r)$ only by a constant factor. The roots of both this polynomial and $\omega(r)$ are the grid points r_k. Finding the roots of the polynomial is a relatively trivial task. For any set of orthogonal polynomials worth considering, the roots will have a standard form which can be easily calculated, and for any other polynomials powerful numerical techniques exist to calculate them.

The equation for the weights w_k is:

$$w_k = \int_a^b \frac{p(r)P_m(r)}{(r - r_k)P'_m(r_k)}dr, \tag{3.5}$$

where $P'_m(r_k)$ is the derivative of the polynomial of degree m at the point r_k. Note that for a given weight function there is usually a more computationally efficient way of defining the grid points and weights of the quadrature scheme, especially since the associated polynomials $P_m(r)$ are known for a large selection of weight functions, and often it is possible to take advantage of the specific functional form of the polynomial when constructing an algorithm for generating the points and weights. This was the case for the weights and grid points used in this work.

3.1.1 Discrete Variable Representations

A discrete variable representation method is a technique for solving the Schrödinger equation based on a discretisation of space [153, 151], relying on an associated Gaussian quadrature scheme.

Since Gaussian quadratures are approximations, a discrete variable representation is an approximation to an exact VBR, or variational basis representation (up to truncation of the VBR operator matrices), via Equation 3.1. DVRs are equivalent to VBRs, but only in the case of an exact quadrature [151]. Making the Gaussian quadrature approximation is equivalent to moving to the DVR regime.

VBRs themselves, meanwhile, are approximations of the true, physical value of the quantity in question (which, in some contrived circumstances, may happen to be exact approximations). In variational methods in quantum mechanics, in order to obtain the exact value of the physical quantity, an infinite number of basis functions are almost always needed. The VBR approximation is precisely the approximation due to truncating the basis to a finite number of functions. The DVR method is then an additional approximation on top of this.

Importantly, in DVR methods, the basis functions are only evaluated on a specific set of grid points. These specific nodes are the ones used in Equation 3.1. That means that many DVR methods, including the ones used here, only evaluate the values of the basis functions at the specified nodes. This has important implications for the project as a whole, as will be discussed in the following sections.

There are many types of DVR, besides the ones based on orthogonal polynomials which are discussed here. One example is a potential-optimised DVR [154], which uses a model potential to attempt to allocate grid points more efficiently. Another is a family of DVR methods that are optimised to certain phase spaces [155, 156]. There are also DVR methods that are simply based on functions other than orthogonal polynomials, such as the sinc DVRs that DUO uses [157, 86], and Lobatto DVRs, which this work utilises and are discussed in-depth further below.

3.1.2 Lobatto Quadratures

One issue with the Gaussian quadratures used with orthogonal-polynomial-based DVR methods is that the grid points the method chooses to optimise the accuracy never includes the points a and b themselves. As Section 3.1.1 implied, when solving the Schrödinger equation with DVR methods, the wavefunctions one obtains are only evaluated at the grid points (in this case the Gaussian quadrature points).

The R-matrix is defined as a sum over the wavefunctions at the *boundary* of the inner region. As such, for the R-matrix method to work it is necessary for the final grid point to be one of the grid points used in the quadrature scheme. Since this cannot be done using regular Gaussian quadrature theory, it must be extended slightly. Again Krylov's textbook [152] shows how to do this and subsection 3.1.3 explores how to do this in more detail.

Initially in this project, the default DVR associated with Duo, the so-called sinc DVR [157], was used to solve the inner region problem. Strictly speaking this is not a DVR in the usual sense as it is not based on an orthogonal polynomial. Rather, it is based on a certain trigonometric function.

For the purposes for which DUO was initially created – high-resolution rovibronic spectroscopy of open-shell diatomics, the sinc DVR method comes with a useful advantage: unlike most Gaussian quadratures, it has a uniform point distribution. Given that a cheap, accurate numerical integration is all that is required of the basis for those purposes, this was sufficient.

For the purposes of this work, however, the sinc DVR method has a key disadvantage: it enforces a zero amplitude boundary condition at both boundaries. Given that the R-matrix method involves using the amplitudes of the basis functions at the boundary to evaluate scattering observables, it would not be possible to use the sinc DVR basis for the purposes of this work.

The next attempted solution of the inner region problem was by using Lobatto quadrature, a specific type of Gaussian quadrature with a weight function of unity, where the two end points of the integration are explicitly included in the scheme as external nodes, thus addressing the issue outlined above. The internal nodes of this

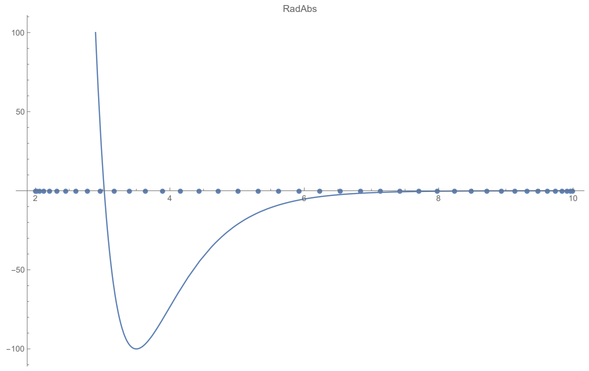

Figure 3.1: The distribution of nodes between the two end points in the Gauss-Legendre quadrature scheme, compared to the shape of a diatomic potential energy curve.

quadrature are the roots of the derivative of the Legendre polynomial [158].

One advantage of this is that the weights associated with the internal and external nodes (the analytic form of which are easily accessible online [158]), can be easily calculated by a simple piece of code, given in a paper by Manolopoulous [148], as derived from a code snippet in *Numerical Recpies* [145], based on a simple Euler method. Furthermore, the weights and grid points are symmetric about the mid-point of the range. This implies that only an even number of grid points can be used.

In this work, the Gauss-Lobatto quadrature scheme was effective, and gave correct inner region solutions when implemented, but two main issues were encountered.

The first issue concerned the distribution of grid points. It was known that the Gauss-Lobatto quadrature would not produce a uniform distribution of quadrature points, however as Figure 3.1 shows, this distribution is very inefficient for the system being analysed.

The PEC being integrated over has its steepest slopes around an equilibrium value near the middle of the integration region. Ideally, the distribution of points in the quadrature scheme would match this by having the densest distribution of points in this region, too. Instead, most of the points are distributed near the start and end of the integration region. These are the two least important regions for integration (except for the last point, which remains important), because the wave functions will not be varying much in these regions. Ideally, a different quadrature scheme with a more efficient distribution of points would be preferable.

Some numerical testing demonstrated the inefficiency of this distribution. Numerical tests were performed on the number of grid points used and its relation to the accuracy of the method. These tests are presented in Rivlin *et al.* [104], and in Chapter 4.

The next issue was the inclusion of the lower bound of the integration range as a quadrature point. The Gauss-Lobatto algorithms given in the citations above rely on the symmetry provided by using both end points in the scheme to simplify the mathematics, making it easier to implement. The issue with this is related to the physics of the problem being solved here.

In the problem being solved here, there is a large repulsive barrier before $r = 0$ (physically, this corresponds to the nuclear repulsion overwhelming the electrostatic force at close range). This means that the wavefunctions for the nuclear motion of the diatom will always be effectively zero at $r = 0$ (the nuclei will never overlap).

As such, there is no issue in the diatomic problem with including the lower bound in the integration (provided the lower bound is placed at a lower value of r than the repulsive barrier). However, when moving to more complex reactions, including atom-diatom collisions, the coordinate systems will include angular coordinates where there will be no repulsive barrier before zero. Furthermore, many wavefunctions have a cusp at the zero point in many coordinates in polyatomic problems. This means that the Lobatto method will break down at these points.

In anticipation of these issues, research was performed in this project into an alternative Gaussian quadrature scheme where only *one* of the end points was included – the point the R-matrix is defined at. Such a scheme, where only one of the end points is included, is called a Gauss-*Radau* quadrature scheme [159]. In addition, research was performed on more general fixed-node quadrature theory, to find a scheme with a better distribution of points.

3.1.3 Quadrature with Fixed Nodes

The objective of this section is to re-define the Gaussian quadrature method to allow for the possibility of including arbitrary fixed points in the algorithm. To simplify the problem, it is helpful to focus on the case where $a = -1$, $b = 1$, and the point -1 is to be explicitly included in the quadrature as the first point.

This range can be transformed into the correct range by a trivial transformation:

$$\int_a^b f(r)\,dr = \frac{b-a}{2}\int_{-1}^{1} f\left(\frac{b-a}{2}r + \frac{a+b}{2}\right)dr, \tag{3.6}$$

which, in the context of Gaussian quadrature, translates to

$$\int_a^b f(r)\,dr \approx \frac{b-a}{2}\sum_{k=1}^{m+1} w_k f\left(\frac{b-a}{2}r_k + \frac{a+b}{2}\right). \tag{3.7}$$

First the polynomial $\Omega(r)$ is introduced, such that

$$\Omega(r) = (r-(-1))\,. \tag{3.8}$$

Clearly in the case of multiple fixed grid points this will be a product over r minus all of the fixed points, in analogy with $\omega(r)$.

Thus the aim is to find a quadrature with $m+1$ grid points, where the first grid point is -1, and the m other points are unfixed and must be determined, as before.

To do this, the polynomial $\omega(r)$, still made up of the same m grid points as in Equation 3.3, must still be orthogonal to every polynomial $Q(r)$ of degree lower than m over the range $[a,b]$, but now not with respect to $p(r)$, but with respect to the product of $\Omega(r)$ and $p(r)$, which is given the name $\rho(r)$:

$$\rho(r) = \Omega(r)p(r), \tag{3.9}$$

such that:

$$\int_a^b \rho(r)\omega(r)Q(r)dr = 0. \tag{3.10}$$

If the polynomial $\pi_m(r)$ is defined to be orthogonal under these conditions but different from $\omega(r)$ by a constant factor (in analogy with $P_m(r)$, as before), then its form can be determined by comparing it to the associated $P_m(r)$. If, for a given weight function $p(r)$, the form of $P_m(r)$ can be determined or is somehow already known, then the corresponding $\pi_m(r)$ for a given set of fixed points can be derived from the following determinant:

$$\pi_m(r) = \frac{K_m}{\Omega(r)} \begin{vmatrix} P_{m+1}(r) & P_{m+1}(-1) \\ P_m(r) & P_m(-1) \end{vmatrix} = \frac{K_m}{\Omega(r)} \left(P_{m+1}(r)P_m(-1) - P_{m+1}(-1)P_m(r) \right), \tag{3.11}$$

where K_m is a constant factor.

From this polynomial, the nodes of the quadrature can be found by determining the roots of the polynomial. Note that $\pi_m(r)$ is not strictly a polynomial due to the $1/\Omega(r)$ term. Instead it is a rational function. Also note that finding the roots of the function is much more difficult than in the previous case, and numerical root finding methods must be carefully employed.

The weights for the unfixed points, w_k, can be determined from a formula similar to Equation 3.5:

$$w_k = \int_{-1}^{1} \frac{p(r)\omega(r)\Omega(r)}{(r - r_k)\omega'(r_k)\Omega(r_k)} dr. \tag{3.12}$$

Note how in this expression the function $\omega(r)$ is divided by its derivative evaluated at r_k, meaning any constant terms attached to the function are eliminated, meaning it can be replaced with $P_m(r)$ and still be valid.

The weight for the fixed point, $r = -1$, can be determined from another formula similar to Equation 3.5:

$$w_1 = \frac{1}{\pi_m(-1)} \int_{-1}^{1} p(r)\pi_m(r) dr. \tag{3.13}$$

Note how in this expression the value of K_m can be ignored by a similar argument to the one used in Equation 3.12: the K_m which comes from the $\pi_m(r)$ term can be taken outside the integral and divided by the K_m from the $\pi_m(-1)$ term, meaning that the value of K_m never needs to be evaluated.

With all of the nodes and weights calculated, the final expression is simply the original definition of the Gaussian quadrature, only with the new definitions for the nodes and weights:

$$\int_{-1}^{1} p(r)f(r)dr \approx \sum_{k=1}^{m+1} w_k f(r_k). \tag{3.14}$$

If the weight function is set to be unity, then this scheme, where one of the end points is included in the quadrature scheme, is the definition of Gauss-Radau quadrature.

3.1.4 Radau Quadratures

As with Gauss-Lobatto quadrature, analytic solutions exist for Gauss-Radau quadrature [159]. Unfortunately the same problem with the distribution of nodes exists, too. An ideal quadrature scheme for use in this work would include a single end point, as Gauss-Radau quadrature does, but also have a distribution of nodes which more closely resembles the slope of a realistic diatomic PEC.

Furthermore, as outlined above, Radau quadratures are more difficult to implement computationally due to the asymmetric nature of the grid. In this work, no grids were discovered that met all the criteria to fulfil the requirements of the RmatReact method, having an efficient numerical implementation and improving on the efficiency of the grid point distribution. Development of an improved Radau-like quadrature did not progress past the theoretical underpinning illustrated here.

Work on the alternative to the Lobatto method for the atom-diatom problem is ongoing, for instance in McKemmish & Tennyson [31], but in this work, the Gauss-Lobatto quadrature was used to produce all results seen in the results chapters.

3.2 Computational Implementation

3.2.1 Inner Region Implementation

Using the Gauss-Lobatto scheme, the inner region solutions can be calculated, starting from a basis set based on Lobatto quadrature, as outlined in [148].

The actual basis functions are Lagrange polynomial shape functions (also known as Lagrange basis polynomials), defined in the following way for a specified grid of $(m+2)$ grid points r_j in a range:

$$\tilde{u}_i(r) = \prod_{j=0}^{m+1}{}' \frac{r - r_j}{r_i - r_j}, \tag{3.15}$$

where the product is over the grid points r_j, and the prime index in the product indicates that the product skips over the $i = j$ term. One of the key properties which makes this basis set useful is the fact that

$$\tilde{u}_i(r_j) = \delta_{ij}. \tag{3.16}$$

Whilst the set of points chosen is in principle arbitrary, the utility of the method rests in a specific choice of points – the Lobatto quadrature points. In this case, that corresponds to the lower bound of r, r_{min}, and the upper bound of r, a_0, being external grid points. The m internal grid points are the roots of the polynomial $P'_m(r)$, which is the derivative of the m^{th} *Legendre polynomial* [158]. Note that this implies boundary conditions of:

$$\begin{aligned}
\tilde{u}_i(r_{\text{min}}) &= \begin{cases} 0 & i \neq 0 \\ 1 & i = 0 \end{cases}, \\
\tilde{u}_i(a_0) &= \begin{cases} 0 & i \neq m+1 \\ 1 & i = m+1 \end{cases}.
\end{aligned} \tag{3.17}$$

The spacing between grid points is non-uniform in this scheme, but the average grid spacing can be shown to be simply:

$$\Delta r = \frac{(a_0 - r_{\text{min}})}{m}, \tag{3.18}$$

where m is the number of internal grid points. Knowing this value is useful for diagnostics. As with most numerical integrators, the spacing between grid points is a crucial metric for the accuracy and convergence of the method.

Anticipating the interaction with the Gauss-Lobatto quadrature scheme, one can also re-normalise the basis by dividing each basis function by the root of the associated quadrature weight, which will be useful for the construction of the matrix to diagonalise:

$$u_i(r) = \frac{1}{\sqrt{w_i}}\tilde{u}_i(r). \tag{3.19}$$

The reason this choice of grid points has utility is its connection to Gaussian quadrature. This is because one can use properties of the basis, and the rules of Gaussian quadrature, to avoid doing any computationally expensive numerical integration. For example, assuming the equality of Equation 3.1 holds, the matrix of overlaps between basis functions can be derived analytically [148]:

$$S_{ij}^{DVR} = \int_{r_{\min}}^{a_0} u_i(r)u_j(r)dr = \sum_{k=0}^{m+1} w_k u_i(r_k)u_j(r_k) = \frac{w_k\delta_{ik}\delta_{jk}}{\sqrt{w_i w_j}} = \delta_{ij}. \tag{3.20}$$

Note that the fact that the overlap matrix is the identity matrix in the discrete variable representation does *not* imply that the functions are orthonormal, even after taking into account the effects of Equation 3.19. Tests using different numerical integration methods have shown that the actual overlap matrix of the functions has non-zero off-diagonal terms. As the number of states is increased, the off-diagonal terms become smaller and the diagonal terms approach unity, however this is not an exact relationship. Hence, the form of Equation 3.20 is an approximation. Testing has shown, so far, that the off-diagonal components are small, and this appears to be a robust approximation within the framework of this algorithm.

Suppressing the J label in the single-channel case, and defining $u_i'(r)$ to be the first derivative of the basis, it is also possible to compute matrix elements of the Hamiltonian plus Bloch/surface operator matrix in this basis:

$$
\begin{aligned}
(H+\mathscr{L})_{ij} &= \int_{r_{\min}}^{a_0}\left(-\frac{\hbar^2}{2\mu}u_i\frac{d^2u_j}{dr^2}+u_iV(r)u_j\right)dr+\frac{\hbar^2}{2\mu}u_i(a_0)u_j'(a_0)\\
&= \int_{r_{\min}}^{a_0}\left(\frac{\hbar^2}{2\mu}u_i'u_j'+u_iV(r)u_j\right)dr-\frac{\hbar^2}{2\mu}\left[u_iu_j'\right]_{r_{\min}}^{a_0}+\frac{\hbar^2}{2\mu}u_i(a_0)u_j'(a_0)\\
&= \sum_{k=0}^{m+1}w_k\left(\frac{\hbar^2}{2\mu}u_i'(r_k)u_j'(r_k)+u_i(r_k)V(r_k)u_j(r_k)\right)+\frac{\hbar^2}{2\mu}u_i(r_{\min})u_j'(r_{\min})\\
&= \sum_{k=0}^{m+1}\left(\frac{\hbar^2}{2\mu}w_ku_i'(r_k)u_j'(r_k)\right)+V(r_i)\delta_{ij}+\frac{\hbar^2}{2\mu}\frac{1}{\sqrt{w_i}}u_i'(r_{\min})\delta_{i0}. \qquad (3.21)
\end{aligned}
$$

Note that in this derivation the surface term added at $r = a_0$ cancels the contribution to the Hamiltonian from the boundary at $r = a_0$, but there is no equivalent surface term at the $r = r_{\min}$ boundary, despite the boundary conditions being equivalent, as shown in Equation 3.17.

This means there is a leftover term at the surface, U_0:

$$
U_0 = \frac{\hbar^2}{2\mu}\frac{1}{\sqrt{w_0}}u_0'(r_{\min}), \qquad (3.22)
$$

and this affects the first element of the matrix. However, for any realistic diatomic PEC there is an asymptotic repulsive barrier in the potential as the distance tends towards zero. As such, assuming the boundary is placed sufficiently far inside this classically forbidden region, all final wavefunctions will have zero amplitude at this boundary, and so this extraneous extra surface term should not influence the physics of the problem in any way. The term was not included in the final version of the code used in the results chapters of this work. The properties of the wavefunction in the classically forbidden region are also of importance for the pure propagation-based R-matrix methods discussed in the previous chapter.

This derivation clearly shows that the expression for the Hamiltonian matrix depends only on the values of the potential and the first derivatives of the basis functions at the Gauss-Lobatto abscissas, and the weights of the Gauss-Lobatto quadrature for each basis function. Hence, once one has calculated the weights and abscissas, the only computation left is the derivatives. The analytic form of the derivative is:

$$u_i'(r) = \frac{1}{\sqrt{w_i}} \frac{1}{\prod_{k=0}^{m+1}{}'(r_i - r_k)} \sum_{j=0}^{m+1}{}' \prod_{k=0}^{m+1}{}''(r - r_k), \tag{3.23}$$

where the prime in the summation indicates the sum does not include the $j = i$ term, the two primes in the product indicates the product does not include both the $k = j$ and $k = i$ terms, and the prime in the denominator means that the product does not include the $k = i$ term.

Since only the values of the derivatives at the abscissae are required, one can reduce this expression to a simpler form. This also has the advantage of being less computationally expensive [160]. The simplification is done by using Gaussian quadrature to integrate $\left(u_i'(r)u_j(r) + u_i(r)uj'(r)\right)$ from 0 to a_0 [160]:

$$u_i'(r_j) = \frac{1}{\sqrt{w_i}} \begin{cases} \frac{1}{2w_i}(\delta_{i(m+1)} - \delta_{i0}) & i = j \\ \frac{1}{r_i - r_j} \prod_{k=0}^{m+1}{}'' \left(\frac{r_j - r_k}{r_i - r_k}\right) & i \neq j \end{cases}, \tag{3.24}$$

where the double prime in the product indicates that the product does not include both the $k = j$ and $k = i$ terms, as before.

The computational expense of the problem can be further reduced by consideration of the symmetry of the grid points and abscissas, which imply that:

$$u_i'(r_j) = -\frac{w_i}{w_j} u_j'(r_i). \tag{3.25}$$

The key reasons for the use of the Lobatto basis functions are the properties of the basis on the boundary: notably, due to Equation 3.16, one of the basis functions has non-zero amplitude on the boundary, which is sufficient to construct the final unbound functions with non-zero amplitude and non-zero first derivative which are vital for the success of the R-matrix method, all without resorting to extra additions to the R-matrix method such as Buttle corrections [128].

Manolopoulos outlines how to construct the basis described in Equations 3.15 and 3.19 both mathematically and computationally [148]. The code outlined in [148] was first implemented in Mathematica for testing purposes, and then implemented in DUO itself. The same was done for Equations 3.24 and 3.25 to construct the derivatives at the grid points, which are necessary to obtain the kinetic components of the Hamiltonian matrix elements of Equation 3.21.

DUO operates in a body-fixed frame, which means that the kinetic components of the Hamiltonian matrix elements have Coriolis coupling terms between different angular momentum projections. These terms are all handled internally by DUO, and are not explicitly included in inputs, or considered separately in outputs.

With the Hamiltonian matrix elements constructed, the next step is to construct the basis, $\chi_k^J(r)$ (in the single-channel case and reintroducing the J label), which diagonalises this matrix. The basis function $\chi_k^J(r)$ is precisely the eigenfunction of the operator on the left hand side of Equation 2.55, which, as described in Equation 2.58, is the basis function used to construct the R-matrix at the boundary.

In the single-channel case, the basis $\chi_k^J(r)$ is constructed from the Lobatto basis $u_i(r)$, such that

$$\chi_k^J(r) = \sum_{i=0}^{N} u_i(r) c_{ik}^J, \tag{3.26}$$

where the c_{ik}^J are the elements of the matrix of coefficients, and N is the number of basis functions used in the calculation. These coefficients are obtained through a matrix diagonalisation routine. The diagonalisation routine also produces the energy eigenvalues, E_k^J, which are also needed for the R-matrix sum at the boundary.

In Mathematica, where the algorithm was first tested, the coefficients c_{ik}^J and energies E_k^J were obtained using the default eigensolver in Mathematica. The algorithm was also tested in C++, where the LAPACK routine *dsyev* [161] was used to diagonalise the matrix to obtain the coefficients and energies. In the final version of DUO used to obtain the results, the similar LAPACK routine *syevr* is also used to obtain these coefficients and energies.

As with the conventional version of DUO, the diagonaliser only provides the eigenvectors of the $J = 0$ problem directly. The $J > 0$ eigenfunctions are provided in the form of coefficients to construct the functions from the $J = 0$ basis, in a similar manner to the basis construction presented in Equation 3.26:

$$\chi_k^J(r) = \sum_{i=0}^{N} \chi_i^0(r) c_{ik}^J. \tag{3.27}$$

Note also that, as Equation 2.62 shows, only the value of this function at a_0 needs to be calculated and stored in order to obtain the outer region scattering results.

In the multichannel case $\chi_k^J(r)$ is replaced with w_{ik}^{Γ}, and E_k^J is replaced with E_k^{Γ} (where Γ contains the list of conserved quantum numbers), as described in Equation 2.65. The diagonalisation procedures are effectively unchanged in this case (including the $J > 0$ functions being presented only as coefficients in a $J = 0$ basis), and only the DUO version of the multichannel diagonaliser was used in this work.

In analogy with Equation 2.62, the single-channel R-matrix which is constructed from the quantities computed by DUO has the form

$$R^J(E) = \frac{\hbar^2}{2\mu a_0} \sum_{k=1}^{N} \frac{\chi_k^J(a_0)^2}{E_k^J - E}, \tag{3.28}$$

where the k counts over the N inner region functions with eigenenergies and eigenfunctions E_k^J and $\chi_k^J(r)$ respectively, and E is the scattering energy in the body-fixed frame. The difference between this and Equation 2.62 is that the sum runs over a finite number N of basis functions, not an infinite number.

Equivalently, the multichannel version of Equation 3.28 is analogous to the R-matrix definition featured in Equation 2.66, but with a finite sum up to N, instead of an infinite sum.

In both the single-channel and multichannel versions of the DUO implementation of Equation 3.27, in practice the $J = 0$ amplitudes obtained from DUO, $\chi_i^0(a_0)$ must first be divided by $\sqrt{w_0}$, the square root of the first Lobatto weight, before being used to construct the amplitudes. This is due to the way the derivative of the Lobatto basis is constructed, as outlined by Manolopoulos [148].

3.2.1.1 DUO Modifications

It is important to note that, as Equation 3.21 shows, the eigenvalues and eigenvectors obtained by the diagonalisation method *are not* the same as the eigenvalues and eigenvectors one would obtain from using DUO in its conventional form. The difference is due to the presence of the Bloch operator, $\mathscr{L}$. This operator subtracts a small term from each matrix element which precisely cancels the contribution at one of the boundaries of the integral.

Because the matrix being diagonalised is not precisely the matrix formed from the Hamiltonian operator, the problem is technically not solving the physical Schrödinger equation per se. However, the Bloch operator was initially introduced in order to account for a different unphysical feature of the system being studied: the artificial boundary conditions in space being imposed by the R-matrix method. Indeed, as Chapter 2 showed, the Bloch term is needed to make the Hamiltonian matrix Hermitian when evaluated over a finite region.

If the boundary a_0 is placed sufficiently far away from the equilibrium bond length of the diatom such that it can be assumed that all the physics of the problem is contained within the inner region, then in most circumstances the term in the integral introduced by the boundary will be negligible: all wavefunctions will have died off. At that point, the Bloch term's contribution is inconsequential. Of course, for every point in space other than $r = a_0$, the Bloch term is zero anyway. Another way of saying this is that in the limit $a_0 \to \infty$, the matrix elements of Equation 3.21 reduces to the matrix elements of H_{ij}.

This must be considered if one wishes to use Lobatto functionality in DUO for a purpose other than obtaining components of R-matrix sums for scattering purposes, and a_0 should be placed sufficiently far out to mitigate these effects.

One other important feature of the implementation of Lobatto functionality in DUO that must be noted is that, unlike with the conventional version of DUO, the number, N, of basis functions used in the R-matrix sum for a given symmetry must equal the number of grid points used in the Lobatto quadrature (represented by $(m+2)$ in Equation 3.15). This is because the methods explained in Section 3.2.1

assume that the number of grid points is equal to the number of basis functions.

DUO, by contrast features functionality to allow one to use a different number of grid points than basis functions when using the conventional sinc DVR basis. This functionality was not replicated for the Lobatto case.

3.2.2 The Harness

Once the components of the R-matrix sum have been obtained from DUO calculations, the R-matrix must be propagated. Since the inner region is scattering energy-independent, the computation need only be performed once for a given system, set of numerical parameters, and desired accuracy.

The R-matrix itself must be constructed at a given scattering energy, though, as can be seen in Equation 3.28. Once the R-matrix at a given energy is constructed, it must be propagated to an asymptotic distance. And once the propagated R-matrix is obtained, scattering observables must be obtained from that. Different codes were used for all of these purposes, and so a ‘harness’ between them was constructed.

The final version of this work contains a harness, written in C++, that reads the outputs of DUO and constructs the $J > 0$ eigenfunctions from the coefficients provided by DUO. It then passes all the eigenenergies and amplitudes at the boundary of these eigenfunctions to PFARM, reads the K- and T-matrices that PFARM produces, produces cross-sections from the T-matrices, and passes the K-matrices to the code reskit to obtain S-matrices. Much of the functionality of DUO and PFARM was also replicated in the single-channel case for testing purposes, in both Mathematica and C++.

In the multichannel case, there were extra complications in the harness stage. Firstly, the channel functions produced by DUO needed to be transformed into a parity-adapted basis, since DUO wavefunctions are only parity-adapted when summing over all channel contributions: the individual channel contributions are not parity-adapted by default. Secondly, there was a conversion between different Hund’s cases which had to be performed on the amplitudes at the boundary. More discussion of this can be found in Chapter 6, where this is explained in detail.

It is expected that for almost all scattering problems more complicated than elastic scattering of atoms, the RmatReact method will need to involve some kind of conversion at the boundary. In the case where actual chemical reactions occur, it will be necessary to perform a coordinate transformation at the boundary, such that the asymptotic states the reactants map on to are described in different coordinates to the ones used to describe the bound state.

Preliminary work has begun on this (see McKemmish and Tennyson [31]), and more work is ongoing. But even in the atom-atom case where no reactions are allowed, Chapter 6 shows one example of a general trend of a transformation being required at the R-matrix boundary.

3.2.3 Outer Region Implementation

Many of the results in Chapter 4 and Chapter 5 were generated using an algorithm written for this work in C++, which was described in Section 2.2. Equation 2.73 was used to propagate a single-channel R-matrix for a given energy E from a distance a_0 to an asymptotic distance a_p, and then Equation 2.81 was used to construct the K-matrix. The arctangent of the K-matrix was then used to construct eigenphases, and the elastic scattering cross-sections, S-matrices, scattering lengths, and effective ranges were then produced from those eigenphases.

Some of the single-channel results in Chapter 5, and all of the multichannel results in Chapter 6, were generated using the code PFARM [94]. PFARM (or PRMAT) was originally designed to perform multichannel R-matrix propagations for electron-atom and electron-ion collisions, especially electron collisions with open d-shell atoms, and collisions at 'intermediate' energies (which are much higher than the energies considered here). The propagation method PFARM uses is based on the BBM propagator discussed in Chapter 2, and the Gailitis expansion introduced in the same chapter.

Whether with the custom-build C++ code or the PFARM implementation, the propagation process was done for hundreds of scattering energies at a time. This allowed for fine-grained plots of scattering observables as a function of energy over small ranges. As a result, it was possible to produce plots which revealed very narrow resonances in certain systems, as seen in, for instance, Chapter 5.

PFARM was designed to be used in conjunction with an inner-region code, as opposed to other R-matrix propagators which are designed to be used without an inner region. The PFARM paper [94] cites examples of inner region codes which can be used with it, including CIV3 [162] and SUPERSTRUCTURE [163].

In PFARM, outputs from inner region codes – channel amplitudes and eigenenergies – are used as inputs for the PFARM propagator to obtain K-matrices and associated scattering observables. More inputs were also required for PFARM and the other propagators to function, however. All the propagators used in this work, including PFARM, relied on an assumption that the reactants interact over a long-range potential of the form:

$$V_{\mathrm{LR}}(r) = \sum_{i=2}^{N_{\mathrm{LR}}} c_i \, r^{-i}, \tag{3.29}$$

where c_i were some set of coefficients which were obtained from both *ab initio* and experimental sources, and N_{LR} was the maximum power that r^{-1} was raised to for that particular long-range potential $V_{\mathrm{LR}}(r)$, under the assumption that no term contained r^{-1} itself. As such, another input that was provided to the propagators was the value of these long-range coefficients c_i for all of the PECs used in the propagation. Parity-adapted Coriolis coupling terms also needed to be provided, as discussed in Chapter 6.

One issue that arose in the development of PFARM for this work is that electron-atom and electron-ion scattering involve significantly different sets of quantum numbers and symmetries from atom-atom scattering. For the purposes of this project, one of the authors of PFARM, Martin Plummer, made many modifications to the code to allow it to accept inputs from DUO to construct an R-matrix to describe atom-atom scattering.

Most of these modifications were adapted specifically to the problem of intra-multiplet mixing in oxygen scattering off helium, as discussed in Chapter 6, with special consideration given to the issues arising from the Hund's cases used. However another modification to PFARM was also made, in order to allow it to accept standard Morse potentials, as discussed in Chapter 2. This is in contrast to the potentials described by Equation 3.29, as Morse potentials decay exponentially and do not accommodate a form that is a polynomial expansion in r^{-1}.

Besides being different physical systems, the energy ranges PFARM was initially designed to operate on are considerably higher than the ultracold temperatures being considered here, and so considerations were also made with respect to the validity of the PFARM results over the ultracold energy ranges which this work focused on.

One large problem which was not addressed thoroughly in this work was the issue of both reactants having structure. Since most R-matrix theory is focused on electron scattering off atoms, ions, and molecules [30], it is usually assumed that one of the reactants, the electron, has no internal quantum numbers besides a spin, and this is assumed here, too. Future work may focus on addressing this oversight.

3.2.3.1 The Variable Step Size Propagator

One extra addition was made to the single-channel propagator constructed in C++ to test against other propagators. The Light-Walker and BBM propagators used in this work (as discussed in Chapter 2) both use fixed step-size propagation, where the spatial gap between adjacent iteration points is pre-determined.

However, for the single-channel Light-Walker implementation used in Chapters 4 and 5, an algorithm was tested that made use of a variable step size based on the derivative of the potential between the two adjacent points. The intention is for the algorithm to use more propagation points in areas where the potential is steep, and fewer in areas where the potential is more shallow. This is comparable to the intentions behind the investigations into improved quadratures in Section 3.1.3, where it was intended to find a quadrature for the inner region which used more points in steeper parts of the potential, and fewer in more shallow parts.

Both of these methods were intended to improve computational efficiency, which would be useful for multidimensional problems the RmatReact method may be applied to in the future. Another advantage of the variable step size method is that in the multi-channel case, channels which contribute different amounts can be treated differently.

Stechel, Walker, and Light [132] devised the variable step size scheme tested in this work. In this scheme, the gap between adjacent iteration points is dependent on the size of the last step. It obeys its own iteration equation, dependent on the derivative of the long-range potential used, in the following way:

$$\delta a_{s+1} = \beta \left(\frac{1}{N_c} \sum_{i=1}^{N_c} \frac{(\lambda_{i,s})^2 - (\lambda_{i,s-1})^2}{\delta a_s} \right)^{-1/3}, \tag{3.30}$$

where i counts over the channels, N_c is the number of channels and, β is a dimensionless control parameter which allows one to specify how many steps should be taken. In the single-channel case, $N_c = 1$ and the definition is the same as the single channel definition of λ_s in Equation 2.68.

The variable step size method replaces the one numerical parameter, N_p, introduced in Section 2.2.2.1, with two numerical parameters. The two parameters are β and an initial step size δa_0 which is needed to seed the iteration. In the multichannel case both of these parameters can be different for different channels. In the single-channel implementation tested in this work, β was tested with a range of values around 0.01, and δa_0 was taken to be a range of values around 0.1% of the distance from a_0 to a_p in tests.

Ultimately the variable step size was not used to generate any of the results in this work, as the testing revealed negligible improvements to computational efficiency compared to the fixed step size propagator methods.

3.2.4 S-matrix Implementation

The S-matrix was defined in Equation 2.23 as a function of the K-matrix, however one can also define it directly from the R-matrix:

$$S^J(k) = \exp\left(-2ikr\right) \frac{1 + iR^J(E, a_p)kr}{1 - iR^J(E, a_p)kr}, \tag{3.31}$$

where $R^J(E)$ is the R-matrix for a given scattering energy, E (with associated scattering wavenumber k), propagated to an asymptotic distance a_p. This allows one to define the S-matrix directly from the definition of the R-matrix.

In the original implementation of the harness code, the propagation was done alongside the harness code with a custom propagator. Also in this original implementation, code was written to produce single-channel S-matrices using Equation 3.31 for complex values of k. This was in order to construct an S-matrix pole finding tool, with the intention of using it as a resonance-finder and as a bound-state-finder, as outlined in Chapter 2. This pole finder was not especially sophisticated, and effectively amounted to a code that printed the S-matrix over a large number of different complex k values, which were then plotted and visually inspected for the presence of poles. Development on this method was limited, and it was never successfully implemented for $J > 0$.

Even in the single-channel, $J = 0$ case that was implemented, the results were questionable, for reasons that will be discussed in Section 3.3.7. For the single-channel, $J = 0$ case, the only S-matrix poles one should expect to find are located along the imaginary axis. When the S-matrix was plotted for imaginary values of k, poles were located in the upper half plane, and these poles were approximately located in places where one would expect to find a bound state energy. These poles were found to be symmetric about the origin, which is not necessarily predicted by the theory outlined in Chapter 2. Furthermore, the poles themselves were found to be unstable, and sensitive to changes in the numerics of the code.

Ultimately, development was stopped on the custom S-matrix pole finder, and when reskit was released, that code was used to locate S-matrix poles instead. reskit is a code that produces elastic scattering S-matrices, and identifies and characterises the resulting poles. It uses Padé approximants [164] to calculate the analytic continuation of the S-matrix in the complex plane and obtain the poles of this S-matrix.

3.3 Numerical and Computational Issues

During the construction of the algorithms used to produce the results in this work, a number of numerical and computational issues were encountered and resolved. Furthermore, several alternate versions of parts of the method were tried and abandoned for a variety of reasons. This section contains a description of some of the alternate methods tried. It also contains descriptions of some of the issues that were faced, and how they were overcome.

Many of the issues highlighted in this section are related to R-matrix methodology in general, and many of the alternate algorithms tried in this work are those which may be useful in different circumstances. This section discusses why the alternate methods were abandoned, and contains descriptions of resolutions to issues faced in the development of the RmatReact method used here that may be pertinent to future work on the method.

3.3.1 Lobatto Derivative Computation Issues

One small problem occurred when designing the Lobatto routine in Fortran for use in DUO, based on the methods developed by Manolopoulos and collaborators [148, 160]. When implementing Equations 3.23, 3.24, and 3.25 in Fortran to compute derivatives of Lobatto basis functions, it was discovered that many overflow errors were occurring, even in double precision numbers. The cause of this problem was difficult to identify at first, as all of the derivatives should have had values well within acceptable boundaries, even for single precision floats. It was eventually discovered that the problem arose due to a naive implementation of Equation 3.24.

To obtain the derivative of the basis function u_i at point r_j, when $i \neq j$, Equation 3.24 states that the product that must be computed has the form:

$$\prod_{k=0}^{m+1}{}'' \left(\frac{r_j - r_k}{r_i - r_k} \right), \tag{3.32}$$

where the double prime indicates that the $k = i$ and $k = j$ terms are excluded.

The issue arose due to the order the product was computed in. The initial implementation simply multiplied successive terms in the product. (All the terms are unitless ratios of distances.) The problem that created was due to the fact that successive terms were very similar when there were a large number of grid points. When a large number of these similar terms were multiplied together, the product either exponentially increased or exponentially decreased (depending on whether the terms were larger or smaller in magnitude than unity).

If the number of grid points was small enough for the double overflow to not occur, then once enough terms had been multiplied in the product, eventually the product would revert back to a reasonably-sized number: there was usually enough small terms to cancel the large ones and vice-versa, they just happened to appear at opposite ends of the product.

To resolve this issue, the Fortran function that performed this operation was modified to compute all of the terms of the product before multiplying them together. These terms were then sorted in size order, riffle-shuffled, and multiplied in that order, such that the largest and smallest terms were multiplied together first, then the second-largest, then second-smallest, and so on. This ensured that the partial product was always a reasonably-sized number throughout the multiplication.

This solution did add a small computational expense due to the cost of the sorting and shuffling routines, compared to the naive implementation, however as a consequence much larger grids could be used to compute results, which was necessary to offset the issues caused by the grid points being inefficiently distributed, as discussed earlier in this chapter.

3.3.2 Deleting Terms from the R-Matrix Sum

The single-channel R-matrix as defined in Equation 3.28 includes a sum over surface amplitudes and eigenenergies of the bound diatomic system in the inner region, with a small modification for the multichannel equivalent. This sum is over all N eigenstates in the inner region, which is also equal to the number of grid points used in the quadrature scheme, as discussed in previous sections of this chapter.

This is another example of the complications caused by needing a large number of grid points for the sake of accuracy in the inner region: the need to compute an equally large number of eigenstates. However, it is possible that a significant proportion of these states need not be included in the R-matrix sum itself, which may be advantageous for efficiency purposes. The last states added to the sum are the ones with the highest energy above dissociation. Because the energy involved can be very large compared to the scattering energy in these cases, the R-matrix sum's denominator, $\left(E_k^J - E\right)$, will have a very large amplitude, which means that that term's contribution to the sum will be very small.

One should expect, then, that a significant number of terms in the R-matrix sum need not be added to it for a given accuracy. This is another example of a possible efficiency increase that is not especially important in the one-dimensional problem being studied here, but could be important for multidimensional problems the RmatReact method may be applied to in the future.

Some estimates [165] expect that any eigenenergies with more than four times the scattering energy can be excluded from the R-matrix sum without loss of accuracy. These estimates are based on problems at much higher scattering energies, so it should not be expected that ultracold problems would exhibit the same behaviour. When this was tested with the single-channel C++ code, it was found that it took a smaller than expected number of excluded states to start encountering accuracy issues with the R-matrix. It is possible that this is due to general boundary condition problems, as in other works [165] it was found to be necessary to use a correction on the diagonal of the matrix which was similar in form to the Buttle correction [128] in order to obtain accurate results. This type of correction is discussed more in the following sections in this chapter.

Research into this problem was not prioritised in this work, and for all the results in the following chapters, the full R-matrix was used with all terms in the sum included.

3.3.3 The Zero-Derivative Problem and Buttle Corrections

One considerable complication introduced by the R-matrix method's partitioning of space is an issue of artificial boundary conditions. The inner region calculation, and the added Bloch term, impose an artificial boundary condition at a_0, which introduces issues when solving the inner region problem.

In DUO's default sinc DVR method, the artificial boundary condition that is imposed is one of zero amplitude at the boundary. As discussed earlier, this is advantageous for the problems DUO was designed to solve, but was not appropriate for the purposes of this work. The replacement Lobatto DVR has non-zero amplitude at the boundary, but, as discussed in private communications with Zdeněk Mašín [166] and espoused in McKemmish & Tennyson [31], it can be shown that a boundary condition of some kind must be present at the a_0 boundary. If the amplitude is not zero, then instead the derivative must be (or if not zero then some fixed finite value which can be treated as if it were zero). This is simply a consequence of the use of the Bloch operator, combined with the fact that a second-order differential equation is being solved.

This is, of course, a problem that all R-matrix methods face. The usual solution to the problem involves a term called a *Buttle correction* [128], or similar corrections. These corrections are used to improve accuracy in cases where there is an enforced derivative on the boundary. One noteworthy work which did not use Buttle corrections is discussed in detail in the next section.

The zero derivative boundary condition is problematic because the R-matrix's core theoretical definition involves an infinite sum, whereas computational implementations can only use a finite number of terms. The R-matrix has a finite derivative, but its inner region Green's function-based definition is a sum of terms which each have zero derivative (in this work; in cases where the amplitude is chosen to be zero, this argument applies to the R-matrix's amplitude instead). In the infinite sum case it is possible to sum over infinitely many zero-valued derivatives to obtain a finite-valued derivative, but it is difficult to converge such a sum with only a finite number of zero-derivative terms.

The Buttle correction attempts to account for this. It is a perturbation-based method that adds an extra term on the boundary. Because it is perturbative, the Buttle correction makes the problem non-variational. It does, however, make the sum converge more efficiently. Buttle corrections were not used in this work – it was anticipated that they would not be needed, as discussed in the section below.

3.3.4 The Generalised Eigenvalue Problem

One part of the reason why it was anticipated that Buttle corrections would not be necessary in this work was due to the initial formulation of the RmatReact method not involving the diagonalisation method described in this chapter.

Whereas the final version of the method presented in this work obtained the inner region amplitudes and energies by diagonalising the matrix formed from the addition of the H and $\mathscr{L}$ operators, the initial versions of the method were based on an earlier proof-of-principle study of an R-matrix approach to reaction dynamics by Bocchetta and Gerratt [69]. The early paper Tennyson *et al.* [167] outlines the theory as it was implemented at the time which was based on this approach.

The method of Bocchetta and Gerratt used a generalised eigenvalue problem: they diagonalised a matrix constructed from a slightly non-orthonormal basis set. Whereas regular eigenvalue problems construct a matrix $\mathbf{\Phi}$ of eigenvectors ϕ_i and a diagonal matrix of eigenvalues $\mathbf{\Lambda}$ from the square matrix $\mathbf{A}$ such that

$$\mathbf{A}\mathbf{\Phi} = \mathbf{\Phi}\mathbf{\Lambda}, \tag{3.33}$$

a generalised eigenvalue problem [168] introduces a second square matrix $\mathbf{B}$ of equal size to $\mathbf{A}$, such that

$$\mathbf{A}\mathbf{\Phi} = \mathbf{B}\mathbf{\Phi}\mathbf{\Lambda}. \tag{3.34}$$

It is always possible to write Equation 3.33 in the form of Equation 3.34 by inserting the identitiy matrix $\mathbf{I}$ at the beginning of the right hand side. In other words, the *generalised* eigenvalue problem represents one where the eigenvectors ϕ_i are in a non-orthonormal basis, and the extent to which $\mathbf{B}$ deviates from the expected identity matrix is a measure of how different the generalised eigenvalue problem is from the regular eigenvalue problem. $\mathbf{B}$ can be thought of as the overlap matrix of the basis functions that form the vectors ϕ_i, which is the identity matrix when the vectors are orthonormal, and has off-diagonal, non-unity elements otherwise.

(Furthermore, if $\mathbf{B}$ is invertible it can be moved over to the left hand side of Equation 3.34 to construct a single matrix in the form of Equation 3.33, although this matrix may not be Hermitian even if $\mathbf{A}$ and $\mathbf{B}$ are.)

The generalised eigenvalue problem was used in the method of Bocchetta and Gerratt because they took the inner region boundary a_0 to be *within* the range their basis functions were defined over. They defined a region of space over which their basis functions were orthonormal, and then placed a 'wall' close to, but not at the end of, this space. This 'wall' was where they defined their inner region boundary a_0. The reason for doing this was to avoid the boundary condition problems discussed above and to avoid needing to use a Buttle correction. They used basis functions that had a zero-amplitude boundary condition, but crucially did not place the R-matrix boundary at this zero-amplitude point, accepting the small amount of non-orthonormality that resulted as a consequence of this.

One trade-off was that this introduced linear dependencies, and other associated convergence issues. Another trade-off was, of course, that this necessitated using the generalised eigenvalue problem to integrate the basis functions over a region they were non-orthonormal over. Generalised eigenvalue problems are typically more expensive to solve numerically than regular eigenvalue problems.

Bocchetta and Gerratt's method was initially implemented in the RmatReact method, with DUO being adapted to include this 'wall', and a harness code being written to re-orthonormalise the basis functions to be orthonormal up to the 'wall' using the Löwdin symmetric orthonormaisation process [169, 170, 171], which, like the famous Gram-Schmidt process [172], constructs an orthonormal basis from a non-orthonormal one. The Löwdin method was chosen for its computational efficiency and stability. Tests on this implementation done during the development of this project show that, practically speaking, the method presented by Bocchetta and Gerratt using a generalised eigenvalue equation yield identical results to methods which re-orthonormalise and use an ordinary eigenvalue equation.

Both the generalised eigenvalue problem and the Gram-Schmidt re-orthonormalisation versions of the method resulted in inner region eigenfunctions that had zero amplitude at the boundary – it was not possible to construct finite amplitude functions in this work, and it was not possible to re-create the results of Bocchetta and Gerratt as a result.

Neither the generalised eigenvalue problem implementation of the method, nor the Gram-Schmidt re-orthonormalisation method, were used in the final version of the code, however their exploration and development did form a large part of the early stages of this work. Eventually they were replaced with the Lobatto DVR methods described earlier in this chapter.

3.3.5 Potential Energy Curve Accuracy

Throughout this work particular attention has been paid to the accuracy of the PECs used in the inner region. The emphasis was placed on obtaining and using high-accuracy diatomic PECs to obtain the inner region amplitudes and energies for use in the R-matrix sum.

An advantage of this approach is that the diatomic PECs used in this work all had accompanying long-range coefficients, which could also be used in the propagation stage of the algorithm. This meant that for values of a_0 placed sufficiently far out, there was no discontinuity in the potentials due to changing from a full, short-range potential to a long-range potential that only consisted of a power series in r^{-1}. This is discussed more in the results chapters, where specific examples of long-range PECs used are provided.

One reason it was considered to be important to obtain high-accuracy potential energy curves was the very low scattering energies the atoms were simulated to be scattering over. Referring to Equation 3.28, the denominator contains the term $\left(E_k^J - E\right)$. A typical value for E_k^J for a given system might be measured in a few tens of wavenumbers (cm^{-1}). However, given that the scattering energy E was typically taken to be on the order of a few tenths of a cm^{-1}, it would be preferable for the values of E_k^J provided by the inner region codes to be accurate to approximately that energy, for the subtraction in the denominator of Equation 3.28 to be accurate.

Even if the accuracy is not of the order of magnitude of the scattering energy, it is still generally advantageous for the inner region amplitudes and energies to be as accurate as possible, as this does eliminate a significant source of error in the eventual scattering results. This also has implications for the S-matrix and the background scattering resonances, as discussed in Section 2.1.5.

The most apparent manifestation of this drive for higher-accuracy PECs can be found in the discussion of the elusive ‘ninth bound state’ in Chapter 5. Here, changes to the PEC used that are only apparent at the millikelvin scale significantly affect some of the scattering observables produced, highlighting the importance of high accuracy in the PECs used in the inner region.

It is worth noting, however, that it can be shown that R-matrix methods are flexible enough to give good results even when the potentials used in the inner region are not highly accurate. As discussed in Chapter 1, the original R-matrix method invented by Wigner and Eisenbud in the 1940s was created for the purpose of nuclear scattering problems. These problems often had very poorly understood scattering potentials [77, 78].

The inner region was almost a 'black box' in these early works, and heuristic and approximate PECs were used due to limited knowledge about the short-range properties of the interactions. More well-known were the long-range interaction properties, and the R-matrix's space partitioning allowed one to compensate for the lack of knowledge about the inner region with a more accurate outer region.

(Interestingly, some of the original scattering problems the R-matrix was designed for use on, such as lithium-hydrogen scattering, are similar to the problems considered in this work, only with much more well-understood inner region PECs. This is in contrast to the electron-atom and electron-molecule problems that R-matrix theory has focused on in more recent years.)

Perhaps in the spirit of Wigner and Eisenbud, it may be the case that modern quantum ultracold collision research has shifted away from attempting to obtain higher and higher accuracy inner region PECs, with a focus more on a better understanding of the long-range interactions used to compensate [173, 174].

3.3.6 Capturing the Bound States

One problem related to the one discussed in the previous section, and which will be elaborated on more in Chapter 5, was the issue of 'capturing' all of the bound states. Early on in the construction of the method, it was realised that in the single-channel version of the algorithm, the inner region boundary a_0 needed to be placed sufficiently far out such that $V(a_0) \approx E_{\text{max}}$, where E_{max} is the value of the bound eigenenergy which is closest to dissociation. If this was not done, then the method produced spurious results.

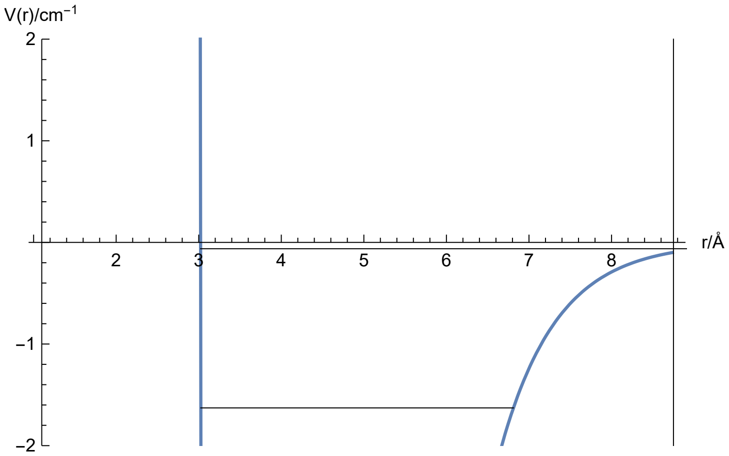

Figure 3.2: A zoom-in of the dissociation region of a PEC used in this work, with the highest two bound states marked with horizontal lines. If the edge of the integration region (represented by a black vertical line) is placed such that $V(a_0)$ is below E_{max}, the state closest to dissociation may be 'missed' by the integration.

A loose explanation for this is that the inner region was not 'capturing' all of the bound states, meaning that an incorrect number of bound states were produced by the inner region diagonalisation due to the boundary not being placed sufficiently far from $r = 0$. By cutting off the integration region before $V(a_0) \approx E_{\text{max}}$, that final state was effectively being assumed to be unbound, as seen in Figure 3.2.

This was especially noticeable when the last bound state was especially close to dissociation, as was the case with some Ar_2 PECs used in Chapter 5, because in these cases the energies were measured in microkelvin and thus for $V(a_0) \approx E_{\text{max}}$, a_0 needed to be very far out, possibly dozens of Ångström (Å), which is large compared to the equilibrium bond length of Ar_2 of 3.5 Å.

The manifestation of this was that the scattering length could potentially be wildly inaccurate if the incorrect number of bound states were found in the inner region diagonalisation, since the scattering length is a quantity that heavily depends on the value of the highest bound state [30]. This is discussed further in Chapter 5.

One practical consequence of this was that very large values of a_0 needed to be used in the method, which meant that larger matrices needed to be diagonalised in the inner region. This was a large part of what drove development of the optimised quadrature schemes and other efficiency improving measures designed to increase the number of states that could be used in the inner region in this work, some of which were discussed earlier in this chapter. These efficiency improving and inner-region enlarging methods are, of course, also useful in the context of the higher-dimension scattering problems this work is intended to lay the groundwork for.

3.3.7 S-matrix Precision

The S-matrix was originally introduced in this work in its single-channel form as the exponent of the eigenphase, $\exp\left(2i\delta^J(k)\right)$. As long as $\delta^J(k)$ is real-valued, then the S-matrix will only have an absolute value of 1. However, when k is allowed to be complex-valued, then $\delta^J(k)$ will also be complex-valued. In that case, the S-matrix will have a real exponential component, and it will be possible for the S-matrix to have any magnitude, including extremely large and extremely small values.

When implementing the custom S-matrix pole finder in the harness code, this problem was quickly encountered. When the S-matrix was plotted over the complex plane for complex k with both positive and negative imaginary values, the resultant values of $S^J(k)$ could vary over 20+ orders of magnitude. This meant that the S-matrix poles were difficult to work with numerically, and also that it was difficult to produce plots that could display identifiable poles.

This is part of the reason why reskit was used instead to produce the results in Chapter 5. Even with reskit, however, a similar issue was encountered. The default numerical settings for reskit were unable to identify poles. It was only when the number of decimal places was changed from 100 to 200 that the pole finder began working as intended. The extreme numerics of the problem may also be why the reskit pole finder only succeeds in finding poles when used over a very narrow range of k values. It is unclear whether these numerical issues imply that the poles themselves are not trustworthy. This will be further discussed in Chapter 5.

Chapter 4

Single-Channel Analytic Scattering

In this chapter results generated using RmatReact are presented for a particle scattering off a Morse potential. These results are then compared to analytic results for this system.

4.1 Potentials Investigated

The main Morse potential used in this chapter is presented in Figure 4.1. This Morse potential uses parameters with reduced mass of $\mu = 33.71525621$ Da (and a value of $\hbar$ obtained from CODATA [175]). The value for μ was chosen for numerical convenience when testing the algorithm, as it meant that $\hbar^2/2\mu$ had a value of 0.5 to seven decimal places in the units of wavenumbers, cm^{-1}, and Ångström, Å. These are the units used throughout this work.

The specific value used for a_{Morse} was chosen such that the ground state eigenenergy was 90 cm^{-1} to six decimal places, for ease of comparison. The values of D_e and r_e used in this work were chosen in analogy with the Ar_2 dimer, which is discussed further in Chapter 5. The analytic eigenenergies were generated from these parameters and Equation 2.98.

Other Morse potentials were tested, notably several obtained from Qiang & Dong [176] for actual diatoms: LiH, H_2, HCl, and CO. Figure 4.2 shows one of these potentials: LiH. In this chapter, only results for the Morse potential shown in Figure 4.1 are presented. Similar numerical behaviour was observed for all of the potentials tested, however.

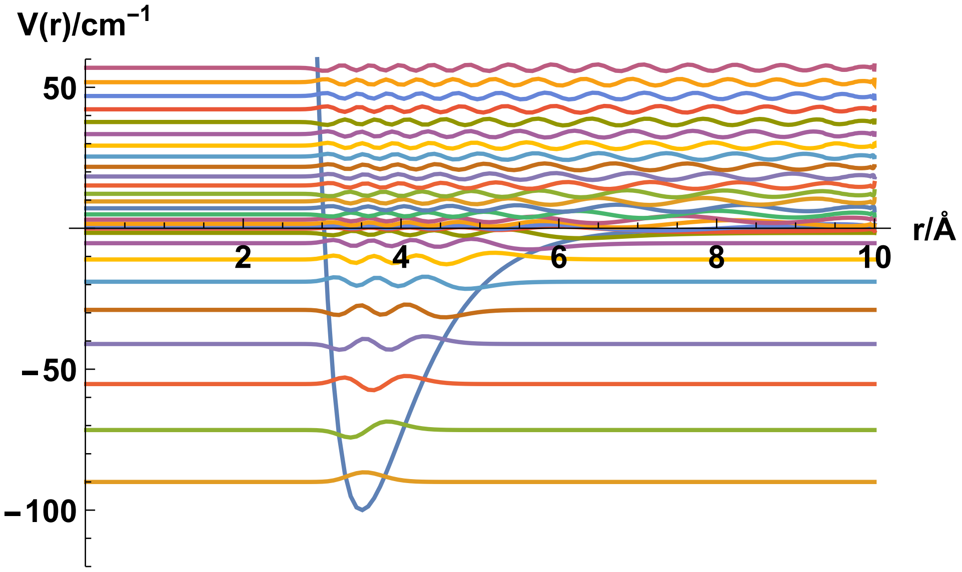

Figure 4.1: A Morse oscillator potential energy curve for an Ar_2-like potential with $D_e = 100$ cm^{-1}, $r_e = 3.5$ Å, $a_{\text{Morse}} = 1.451455517$ Å^{-1}. Wavefunctions of the vibrational bound states are also shown at their associated eigenenergies, along with with the continuum states between 0 and 60 cm^{-1}. The bound and continuum states were generated by solving the Schrödinger equation with $\mu = 33.71525621$ Da with an R-matrix method with a boundary of 10 Å.

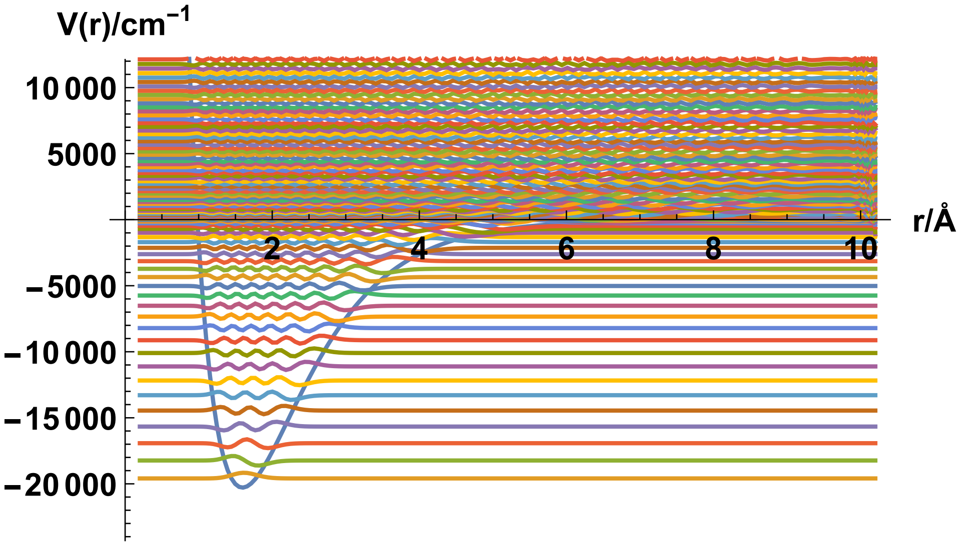

Figure 4.2: Morse oscillator potential and states for LiH. Parameters used are $D_e = 20287.62581$ cm^{-1}, $r_e = 1.5956$ Å, $a_{\text{Morse}} = 1.128$ Å^{-1}. The states were generated by solving the Schrödinger equation with $\mu = 0.8801221$ Da with an R-matrix method with a boundary of 10 Å.

4.2 Numerical Details

The R-matrix method was used to generate scattering results, including the eigenphase and the scattering length, for the single-channel, $J = 0$ Morse oscillator potential. These results are compared with the analytic results quoted above.

In the construction of the R-matrix, the inner region bound system was solved numerically to generate the bound eigenenergies and radial eigenfunctions of two particles interacting over a Morse potential well. To generate the numeric results, $N = 200$ grid points and eigenfunctions were used to obtain the inner region eigenenergies (and amplitudes) using the Lobatto shape functions DVR method outlined in Section 3.2.1. The inner region was defined to range from $r_{\text{min}} = 0.01$Å to $a_0 = 10.0$Å.

The R-matrix was then constructed on the boundary and propagated to an asymptotic radius. For the results presented in the following, the propagation was performed from $a_0 = 10.0$ Å to $a_p = 25.0$ Å, with $N_{\text{prop}} = 2500$ iterations of the propagation equation over a uniform grid. The propagated R-matrix was then used to construct the eigenphase for the $J = 0$ Morse scattering event.

To explore the low-energy behaviour of the numeric method, the analytic and numeric eigenphases were used to generate the scattering length and effective range. This was done by fitting the low-energy plot to the form given in Equation 2.29 using *Mathematica*'s FindFit function over the lower scattering energy range $k = 0.0004$ Å to $k = 0.001$ Å. (This is equivalent to $E = 8.0 \times 10^{-8}$ cm^{-1} to $E = 5.0 \times 10^{-7}$ cm^{-1} for this system.)

4.3 Analytic-Numeric Comparisons

The numerical and analytic results for the eigenenergies are presented in Table 4.1. For low-lying states whose wavefunctions are essentially completely contained in the inner region, the agreement between the two methods is excellent. The final two states are more diffuse, as seen in Figure 4.1, and hence they are more likely to have significant amplitude outside the inner region. Due to this, the inner region solution energies lies slightly below the true answer.

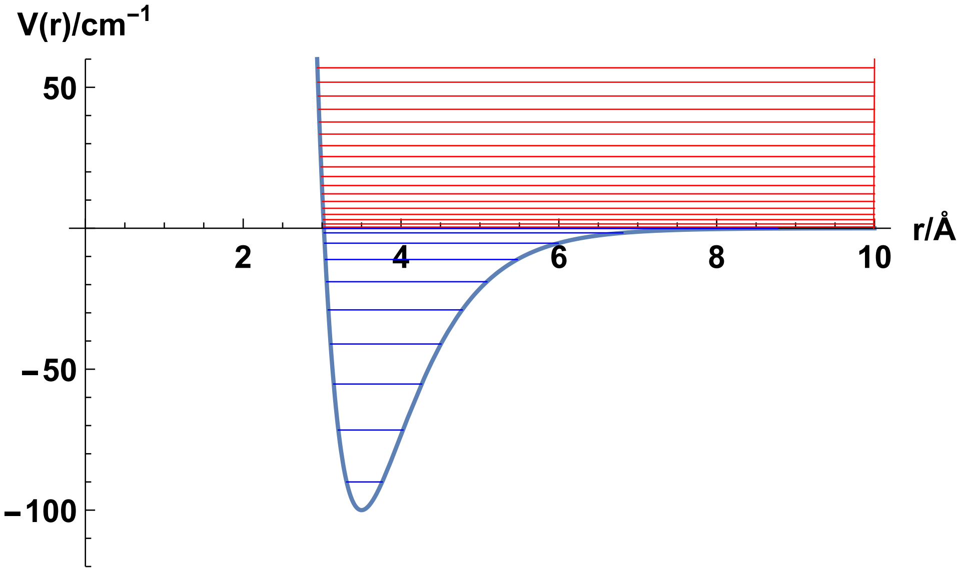

Figure 4.3: The same Morse oscillator potential as in Figure 4.1. Energy levels of the continuum states generated by the R-matrix below below 60 cm^{-1} are coloured differently to the vibrational bound states in order to distinguish the states close to dissociation from the states just above dissociation. The R-matrix inner region boundary, $a_0 = 10$ Å, is also highlighted.

Table 4.1: Comparison of the analytic and numeric bound eigenenergies of the Morse diatomic system for vibrational energy levels $n = 0$ to 9. The relative error refers to the difference between each level's numeric and analytic values, divided by the analytic value (analytic minus numeric, divided by analytic).

n	Analytic / cm^{-1}	R-matrix / cm^{-1}	Relative error
0	-90.000000	-90.000000	1.73×10^{-12}
1	-71.580042	-71.580042	4.59×10^{-11}
2	-55.266807	-55.266807	1.30×10^{-11}
3	-41.060295	-41.060295	1.82×10^{-11}
4	-28.960506	-28.960506	5.73×10^{-12}
5	-18.967441	-18.967441	1.33×10^{-12}
6	-11.081099	-11.081099	3.25×10^{-12}
7	-5.3014807	-5.3014807	-6.42×10^{-12}
8	-1.6285853	-1.6286033	-0.000011
9	-0.062413189	-0.094633937	-0.516

Figure 4.4 compares the RmatReact numerical eigenphase to the analytic solution for the eigenphase given by Equation 2.112 over the scattering energy range of 0.001 to 0.1 cm^{-1} (0.00144 to 0.144 K). The root mean square difference between them is approximately 4.6×10^{-5} radians, which is small.

Table 4.2: Table of comparisons for the analytic and numeric scattering length and effective range. The relative error refers to the difference between each quantity's numeric and analytic values divided by the analytic value (analytic minus numeric, divided by analytic).

	Analytic/Å	R-matrix/Å	Relative error
Scattering Length	10.166078	10.166133	-5.34×10^{-6}
Effective Range	1.6537298	1.6667562	-0.00788

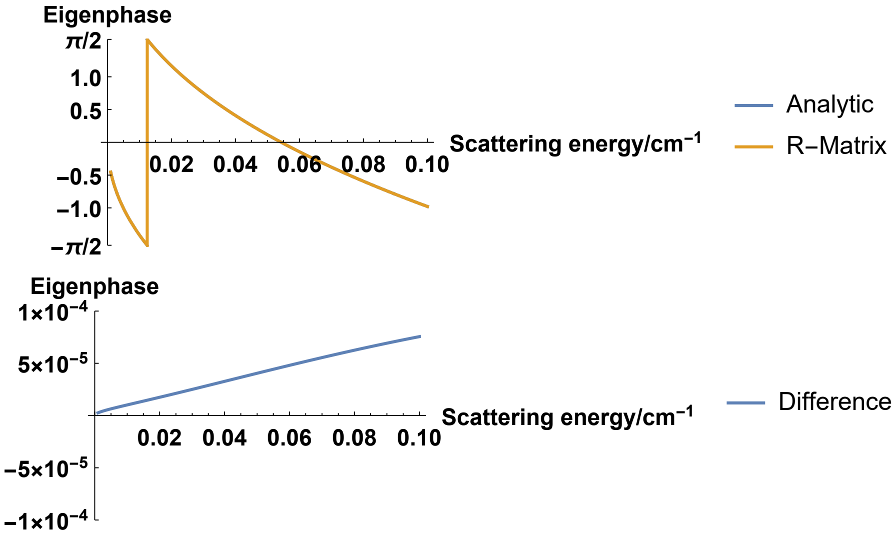

Figure 4.4: Upper plot: eigenphase (in radians) for a scattering event for the Morse potential of Figure 4.1 calculated both analytically and using R-matrix methodology. The two lines overlap. Lower plot: difference (analytic − R-matrix) in eigenphase (in radians) between the two methods.

Analytic and numerical results for scattering length and effective range are presented in Table 4.2. Again the results given by the two methods are very similar.

4.4 Numerical Parameters

To investigate the accuracy of the R-matrix method in comparison to the analytic results, the numerical parameters used in the algorithm were varied and the resultant error was plotted. The seven numerical parameters which the method relies on are summarised in Table 4.3. A consideration of these parameters is relevant to all of the results generated in this work.

To encapsulate all of the information in the lower plot of Figure 4.4 in one number, the error metric used was a variation of the root mean square deviation (RMSD)

Table 4.3: Table of numerical parameters

Symbol	Definition	Units
N	Number of inner region states and grid points	Unitless
N_{prop}	Number of propagation points	Unitless
r_{min}	Start of inner region	Å
a_0	End of inner region and start of propagation	Å
a_p	End of propagation	Å
Δr	$\frac{a_0 - r_{\text{min}}}{N-1}$ Average inner region grid spacing	Å
Δr_{prop}	$\frac{a_p - a_0}{N-1}$ Average propagator grid spacing	Å

between the eigenphase, $\delta(E)$ calculated using the R-matrix method ($\delta_{\text{num}}(E)$) and the analytic eigenphase ($\delta_{\text{ana}}(E)$). The eigenphase was calculated for 100 equally spaced scattering energy values between 0.001 and 0.1 cm^{-1}. The error characteristic was then calculated using a variation of the definition of the RMSD:

$$\delta_{\text{RMSD}} = \sum_{i=1}^{100} \sqrt{\frac{\left(\delta_{\text{ana}}(E_i) - \delta_{\text{num}}(E_i)\right)^2}{100}}. \tag{4.1}$$

A version of this error metric which involved (numerically) integrating the squared difference over the energy range was tested, and found to give the same results as merely sampling over 100 equally spaced points in the energy range. Plotting δ_{RMSD} as a function of different error parameters facilitated the assessment of the numerical stability of the method. These plots can be found in Figure 4.5. For all of the plots in Figure 4.5, r_{min} was kept constant at 0.01Å.

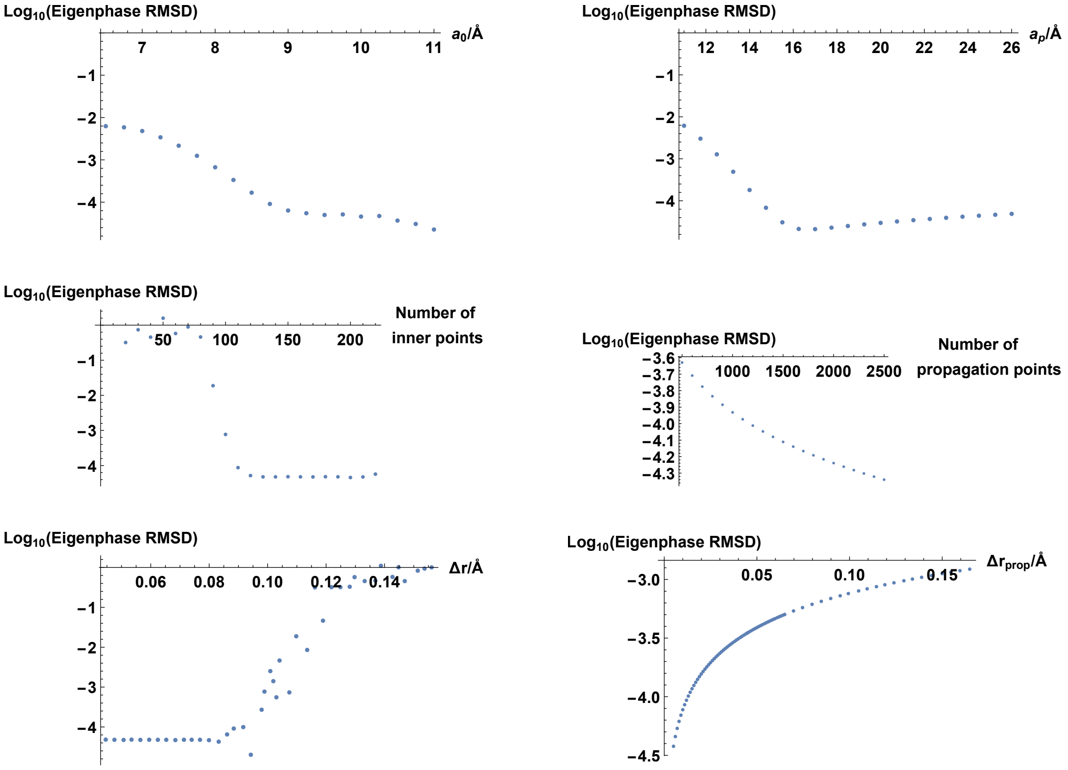

Figure 4.5: Top left: The log of the RMSD of the eigenphase plotted against a_0 between 6.5Å and 11Å. The other parameters were held constant at $N = 200$, $N_{\text{prop}} = 2500$, $r_{\text{prop}} = 25$Å.

Top right: The log of the RMSD of the eigenphase plotted against a_p between 11Å and 26Å. The other parameters were held constant at $N = 200$, $N_{\text{prop}} = 2500$, $a_0 = 10$Å.

Middle left: The log of the RMSD of the eigenphase plotted against N between 20 and 220. The other parameters were held constant at $N_{\text{prop}} = 2500$, $a_0 = 10$Å, $r_{\text{prop}} = 25$Å.

Middle right: The log of the RMSD of the eigenphase plotted against N_{prop} between 500 and 2500. The other parameters were held constant at $N = 200$, $a_0 = 10$Å, $r_{\text{prop}} = 25$Å.

Bottom left: The log of the RMSD of the eigenphase plotted against Δr between 0.0445982Å and 0.156094Å. N was allowed to vary between 223 and 63 to vary Δr. The other parameters were held constant at $a_0 = 10$Å, $N_{\text{prop}} = 2500$, $r_{\text{prop}} = 25$.

Bottom right: The log of the RMSD of the eigenphase plotted against Δr_{prop} between 0.005Å and 0.164835Å. N_{prop} was allowed to vary between 3000 and 90 to vary Δr_{prop}. The other parameters were held constant at $N = 200$, $a_0 = 10$Å, $r_{\text{prop}} = 25$.

When varying a_0, any a_0 value above approximately 9 Å appears to produce converged results where the error changes very little. This is likely because a value of a_0 which is too small cannot accurately ‘capture’ all of the bound states of the potential well. Since the final bound state is of the order 10^{-2} cm^{-1} in depth, $V(a_0)$ must be approximately of that order for the state to be found by the method.

When varying a_p, any value above 16 Å appears to produce converged results; however, the error increases slightly as a_p is extended beyond 16 Å. This is likely due to Δr_{prop} increasing as N_{prop} is held constant, which decreases the accuracy of the approximations made in the propagator method.

When varying N and Δr (where Δr is increased by decreasing N and vice-versa), there is a clear point where increasing N further has no effect, but where decreasing N even slightly significantly increases the error. This suggests that the method is converging on a solution once the grid spacing is sufficiently small, as is common in numerical integration techniques. This further suggests that this solution's RMSD from the analytic solution is approximately 10^{-4}.

Finally, when varying N_{prop} and Δr_{prop}, the method appears to produce results with very low error for all values of N_{prop} and Δr_{prop} tested, with only slight variation in the error recorded. This suggests that it is possible to propagate the R-matrix using very few, very wide steps and still produce accurate results. However, this may be a consequence of using as the test potential the Morse oscillator potential, since it decreases exponentially with distance and thus varies very little in the outer region. More realistic potentials are longer-range and multipolar in nature at large r, so narrower steps may be needed in the propagation.

Chapter 5

Single-Channel Argon-Argon Scattering

In this chapter, numerical results are presented for the elastic scattering of argon atoms off other argon atoms at ultracold temperatures, ranging from sub-μK temperatures up to approximately 1 K ($= 0.695$ cm^{-1}). Several different ground state Ar_2 potential energy curves (PECs) [120, 121, 178, 179, 123, 177, 136] are examined in order to simulate this scattering. These PECs are listed in Table 5.1.

Despite having a shallow PEC formed from van der Waals forces, similar to other noble gas dimers, and in contrast to the more deep-well systems that the method was designed to study [167], the argon-argon system was chosen as a test system for the algorithm. This was in order to compare against existing experimental and computational results, for example the work of Barker *et al.* [14, 180],

Table 5.1: The five PECs studied in this work, with their minima and equilibrium distances. The number of $J = 0$ bound states derived in this work is the same as in all cited references. Note here the differing numbers of calculated bound states (N_{bound}) between the methods.

Label	Authors	Citation	N_{bound}	V_{min} / cm^{-1}	r_{min} / Å
PM	Patkowski *et al.*	[120]	9	-99.269	3.7673
Az	Aziz	[121]	8	-99.554	3.7570
TT	Tang *et al.*	[123]	8	-99.751	3.7565
PS	Patkowski *et al.*	[177]	9	-99.351	3.7624
MD	Myatt *et al.*	[136]	8	-99.490	3.7660

where it is used for sympathetic cooling. The large number of high-accuracy PECs available for Ar_2 make it a good candidate for testing the RmatReact method. Experiments have also been performed on cold ground state argon atoms [180].

Barletta *et al.* [15] studied low-energy Ar-Ar collisions in support of experimental studies using Ar for sympathetic cooling [14]; they assessed four PECs for the Ar_2 system. Of these four, three are also assessed in this work (PM, Az, TT, see Table 5.1); the fourth PEC of Slavíček *et al.* [122] is not considered here, but two additional ones are. All five PECs studied here superficially appear very similar. However, as Table 5.1 shows, they do have slight differences which have significant impacts on their low-energy scattering properties. The PM and PS PECs were generated *ab initio*, whilst Az, TT and MD used experimental results in their fit.

The issue of the highly varying scattering lengths appears to be closely linked to a long-standing debate over the number of vibrational ($J = 0$) bound states belonging to the Ar_2 system. Some PECs appear to support only eight bound states, while others appear to support a ninth bound state. If this state exists, it has a binding energy on the order of magnitude of 1 μK, which is approximately 0.7 μcm^{-1}, or 86 picoelectronVolts, and thus would be difficult to detect. Nevertheless, the value of the scattering length of a particular system is highly dependent on the position of the highest bound state [30]. Consequently, whether or not this state exists has important implications for the physics of argon-argon scattering.

Sahraeian *et al.* [181] study two Ar_2 PECs; those which here have been labelled PM and PS. They claim to have located the ninth bound state in both cases. This result for the PM PEC is in agreement with Barletta *et al.* [15].

5.1 Bound States

When performing the inner region calculations with DUO in this work, the number of bound states was found to be in agreement with literature values [15, 181] for all five PECs studied (see Table 5.1).

However, there were considerable complications when attempting to detect the ninth bound state in this work for the PECs where it was predicted to exist – the

PS and PM potentials. As this state is so weakly bound, it was necessary to extend the inner region calculations out to large distances in order to detect it. This ninth bound state has many similarities to a halo state [182], as seen in Figure 5.1, which shows the ninth bound state as a function of r for the PM PEC when $a_0 = 50$ Å.

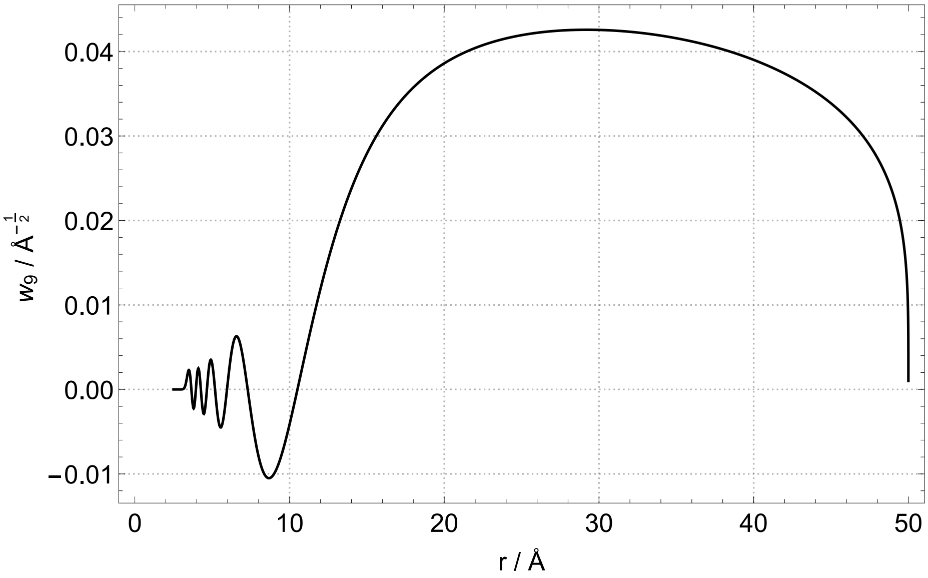

Figure 5.1: The wavefunction of the ninth bound state of the PM PEC, plotted as a function of r, for when $a_0 = 50$ Å.

The results in Table 5.3 of this work were obtained only by extending the inner region boundary a_0 out to distances of over 35 Å for the PM PEC and over 40 Å for the PS PEC. As such, a very large number of points needed to be used in order to maintain precision.

The difficulty in detecting the ninth bound state is underlined by the fact that when the diatomic nuclear motion code LEVEL [88] was used, the ninth bound state was never detected for any of PECs considered here, no matter how far out or how many points the inner region was integrated over. Sahraeian *et al.* [181] also cited difficulties in detecting this state, which they quote a value of $-0.86233\ \mu\text{cm}^{-1}$ for.

Consequently the actual binding energy of the ninth bound state, for PECs in which it was detected, varied as a function of the a_0 used in the integration here, up to 100 Å. This is seen in Figure 5.2, which shows the value of the ninth bound state, E_9, of the PM and PS PECs as a function of a_0, for all values of a_0 under 105 Å for which the state was actually bound. If the calculations are converging on fixed values of E_9, they are significantly different from the value obtained by Sahraeian *et al.*

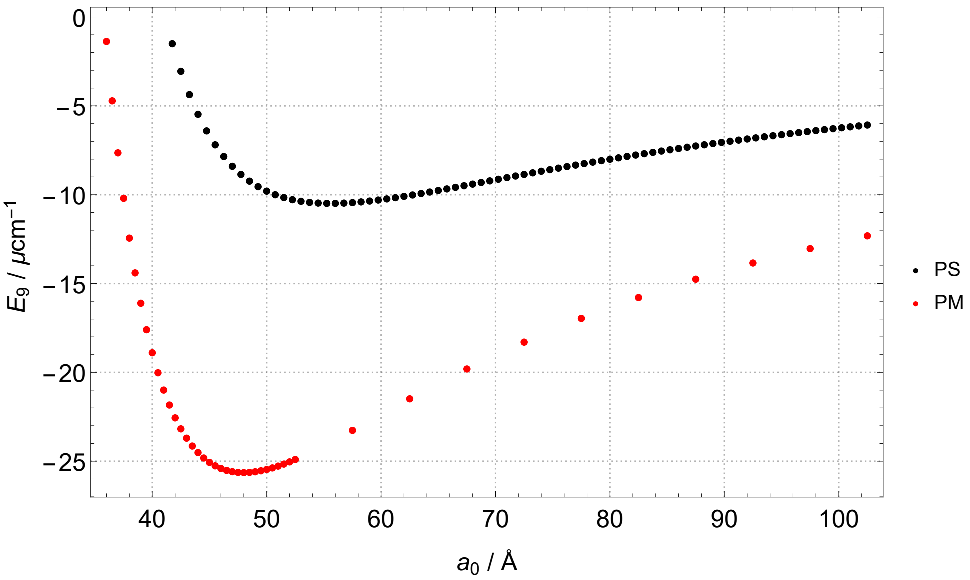

Figure 5.2: The ninth bound state of the PM and PS PECs, plotted as a function of the a_0 used in the calculation to generate them, whilst keeping r_{min} and the average grid spacing used constant.

Once a threshold value of a_0 was reached, every PEC that the literature claimed had nine bound states were consistently found to do so, even if its value changed with a_0. No ninth bound state was detected in this work for any PEC for which it was claimed that there are only eight bound states, even when using large values of a_0 over 100 Å.

5.2 Resonances

The supplementary data provided by Myatt *et al.* [136] (MD) includes the rovibrational eigenenergies of the Ar$_2$ system obtained using LEVEL [88]. The supplementary data also quotes values for states which lie above the dissociation threshold but below a centrifugal barrier for $J > 0$, known as quasibound states. The quasibound states from Myatt *et al.* [136] which have J quantum numbers $J \leq 10$ are quoted in Table 5.2.

In this work, the quasibound states quoted for the MD potential in Myatt *et al.*

Table 5.2: Positions E_{res}, widths Γ_{res}, and background resonance paramters A_0 and A_1 of the three shape resonances produced in this work by fitting eigenphases to Equation 2.44. Standard errors are obtained by comparing these figures to those of the three quasibound states extracted from the supplementary data of Myatt *et al.* (MD). The widths extracted from Myatt *et al.* have been multiplied by two to match the convention employed in this paper.

v	J	E_{res} /cm^{-1} (MD)	Γ_{res} /cm^{-1} (MD)	E_{res} /cm^{-1} (this work)	Γ_{res} /cm^{-1} (this work)
6	9	0.129	0.660×10^{-6}	0.1287	0.663×10^{-6}
6	10	0.448	0.00330	0.4486(2)	0.00247(46)
7	5	0.071	0.00605	0.06993(5)	0.004841(5)

v	J	A_0	A_1 /(cm^{-1})$^{-1}$
6	9	0	0
6	10	-0.107	0.757
7	5	0.00213	-0.997

[136] were characterised by analysing resonances in the scattering calculation. The diatomic nuclear motion code used in this work, DUO, does not have the capacity to detect quasibound eigenvalues directly (although it is possible to detect them using a stabilisation method with continuum states). However, these quasibound states should correspond to shape resonances, which can be detected in plots of the eigenphase and cross-section.

In order to detect the shape resonances, the RmatReact method was used to generate the eigenphase, and from it the partial cross-sections for all the partial waves with $J \leq 10$. The inner region was calculated using 500 Lobatto grid points between $r_{\text{min}} = 2.5$ Å and $a_0 = 22.5$ Å. The outer region propagation was performed from $a_0 = 22.5$ Å to $a_p = 45$ Å, with over 1,000 propagation iterations.

Figure 5.4 shows the eigenphase and cross-section generated using the MD potential for $J = 0$, $J = 5$, and $J = 10$. Figure 5.5 shows the eigenphase and cross-section generated using the MD potential for $J = 9$, with clear Fano profiles [37] associated with a resonance present. In all these cases, the eigenphase and cross-section were calculated for energies between $E = 0.001$ cm^{-1} and $E = 1$ cm^{-1}.

The Fano profiles seen in the results generated in this work are indicative of one of the strengths of the methods presented here over other methods. Because this method facilitates a full scattering calculation, it is able to obtain much more information about the resonances it detects, when compared to the bound state methods that were used to generate the other results in this chapter. For instance, the results generated by Myatt *et al.* using LEVEL only provide resonance positions and widths as numbers, whereas other scattering codes, such as MOLSCAT [59], are able to produce the full line profile and facilitate more in-depth analysis of the specific shape of the resonance. As Figure 5.5 shows, the same is possible with the methods presented here.

The $J = 0$ partial wave plots are included in Figure 5.4 to indicate what a typical eigenphase and cross-section looks like for this system when no resonances are present: in the $J = 0$ cross-section plot the cross-section sharply rises at low energies.

Myatt *et al.* [136] predicted (see Table 5.2) that there should be quasibound states in the $J = 5$, $J = 9$, and $J = 10$ partial waves. These resonances can clearly be seen in the calculations presented here (Figures 5.4 and 5.5) where their positions are marked with dashed lines. These three states are the only quasibound states given by Myatt *et al.* for $J \leq 10$ and the only resonances detected in this work.

For the $J = 5$ and $J = 10$ resonances, the energy E_{res}, width Γ_{res}, and A_0 and A_1 parameters were fitted to the Breit-Wigner form of Equation 2.44, using the values quoted by Myatt *et al.* as the starting point of the fitting procedure. The very narrow $J = 9$ resonance could not be fit in this way, and so the energy location of the width was determined by identifying where the eigenphase suddenly went from $\approx \frac{\pi}{2}$ to $\approx -\frac{\pi}{2}$ and identifying the two points either side of this jump; E_{res} was taken as the mid-point between them. This energy was then inserted directly into the Breit-Wigner fit.

Figure 5.3 shows the result of this procedure for the resonance in the $J = 10$ partial wave. The fitting was performed using the energy range $E = 0.4006$ cm^{-1} to $E = 0.499501$ cm^{-1}, using the Levenberg-Marquardt algorithm as implemented in the software Origin (OriginLab, Northhampton, MA).

Table 5.2 contains the results of this fitting procedure for all three resonances studied in this work (all using the same software and algorithm with appropriate energy ranges). The narrowest resonance is for $J = 9$ and there is very good agreement between the results presented here and those quoted by Myatt *et al.* [136]. For the other two, broader resonances slightly different positions and widths were found. This is consistent with the full treatment of coupling to the continuum obtained in a scattering calculation: LEVEL, as used by Myatt *et al.* for their quasibound states, is known to be less well-adapted for characterising broader resonances [88, 183]. Both the resonance position and width for $J = 10$ are also similar to the figures quoted by Čížek *et al.* [184].

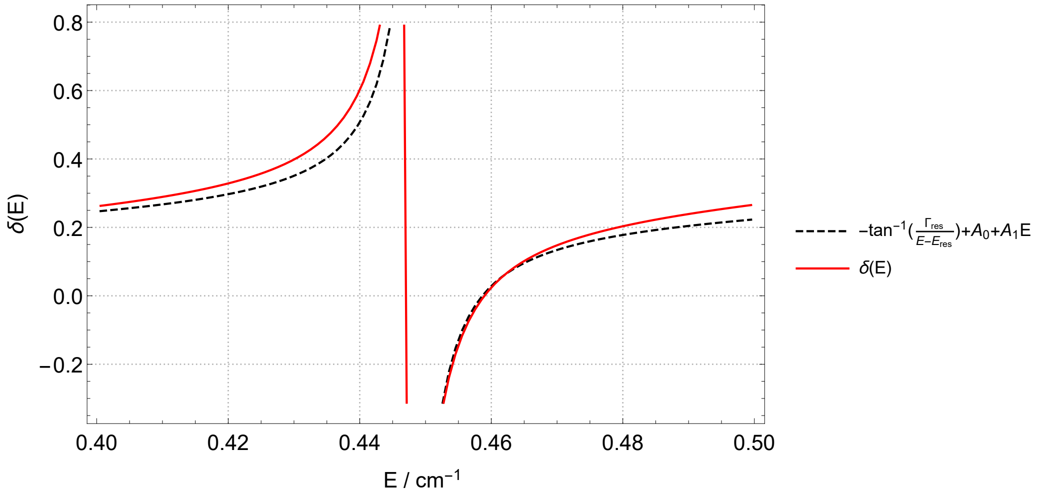

Figure 5.3: Eigenphases in the region of the $J = 10$ resonance (solid red line) with the Breit-Wigner fit used here (dashed black line).

As Figure 5.5 and Table 5.2 show, narrow resonances can be hard to detect. The only resonances detected in this work were ones which had been previously predicted and only needed to be corroborated. In the future, a more sophisticated resonance-detecting software such as those by Tennyson and Noble [36] or Noble *et al.* [185], or possibly a procedure based on the complex analysis of the S-matrix [116] such as that of Čížek and Horáček [118], will be used to to detect resonances which may otherwise be missed. A different S-matrix-pole-based resonance finding method is presented in Section 5.4.

Finally, Figure 5.6 shows the total cross-section generated using the RmatReact

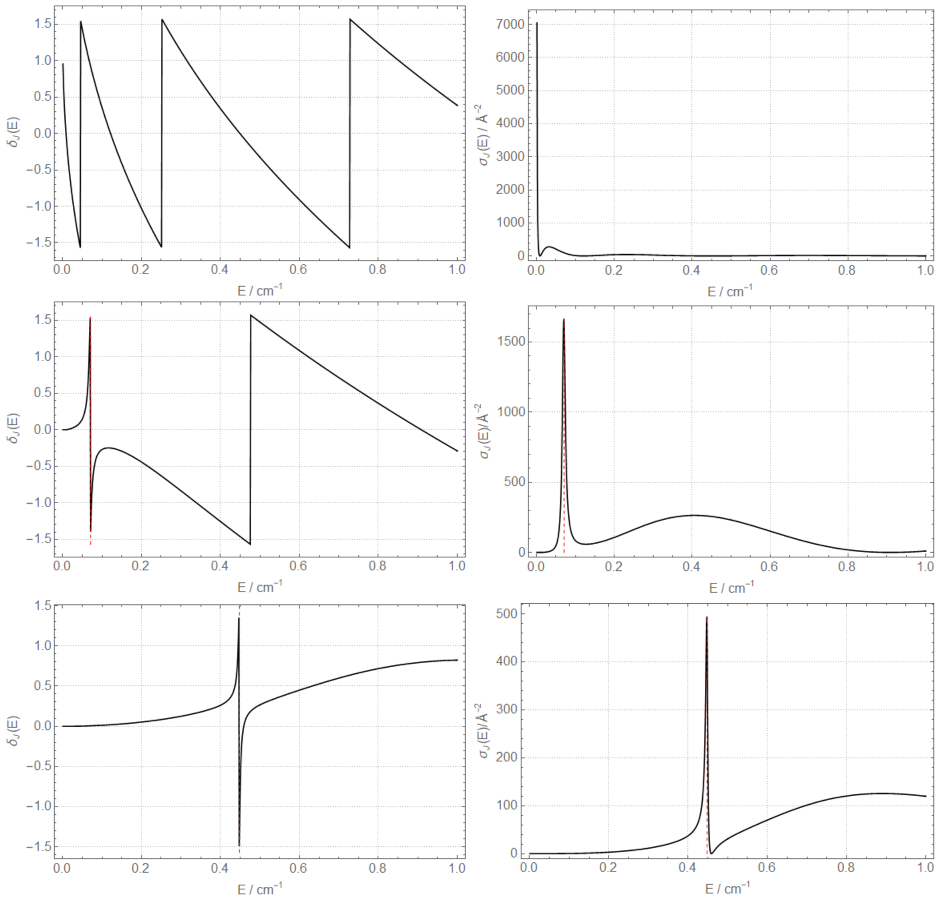

Figure 5.4: Eigenphase (top left, bottom left) and cross-section (top right, bottom right) plots for the $J = 0$, $J = 5$ and $J = 10$ partial waves, generated using the MD potential. The dashed red lines mark the position of the resonances.

method with the MD potential. The quasibound states predicted by Myatt *et al.* [136] are also pictured. This figure gives a good overview of the properties of argon-argon scattering at low energy. It is notable for having many features. Besides the three resonances, there is also more structure to the plot – something that is more prevalent in heavy particle scattering than electron-atom or electron-molecule scattering due to the greater number of partial waves contributing to the scattering process. Furthermore, the cross-section tends to a large value at the lowest energies on the graph. This corroborates the feature seen in Figure 5.7 towards the lowest energies where the cross section becomes very large.

Thus far the consequences of the Pauli principle have not been considered. ^{40}Ar is a Boson with zero nuclear spin; as a consequence collisions with odd J are forbidden. Figure 5.6 shows the observable cross section obtained by simply

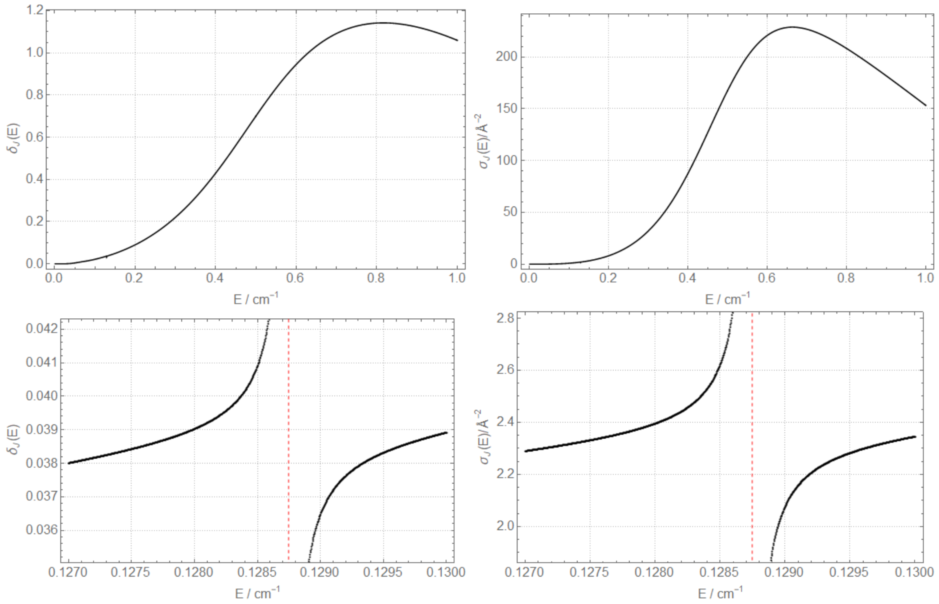

Figure 5.5: Eigenphase (left) and cross-section (right) for the $J = 9$ partial wave. Although the plot appears to be smooth on the scale in the top two plots, the bottom two plots are on a much narrower scale, and a resonance is clearly visible (position given by the dashed red line). Both this narrow width and its position are in agreement with the quasibound state of Myatt *et al.* as described in Table 5.2.

summing partial waves with even J. As a consequence the resonances with $J = 5$ and $J = 9$ disappear and there is a pronounced Ramsauer minimum at about 0.01 cm^{-1}.

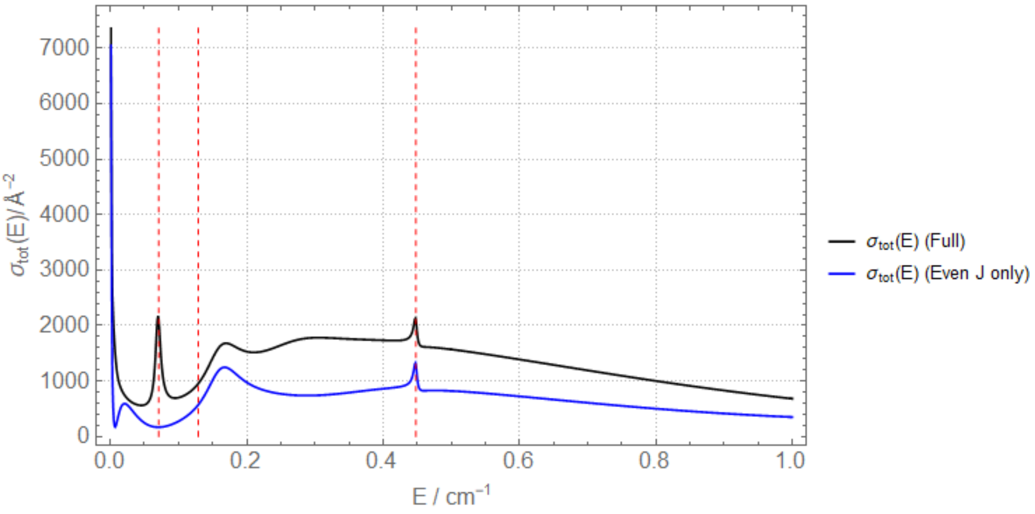

Figure 5.6: Total cross-section when summing over the partial waves $J = 0$ to $J = 10$, using the same numerical parameters as above. The three quasibound states of Table 5.2 are marked with dashed lines. The sum over even Js allows for the Pauli Principle.

5.3 Low-Energy Scattering

In order to analyse low-energy scattering behaviour, the cross-section for $J = 0$ was plotted for $E = 10^{-8}$ cm^{-1} to E = 1 cm^{-1} on a log-log axis, see Figure 5.7. The same numerical parameters were used as in Section 5.2. The plot shows that the cross-section tends towards a constant at lower energies, which is predicted by Equation 2.29.

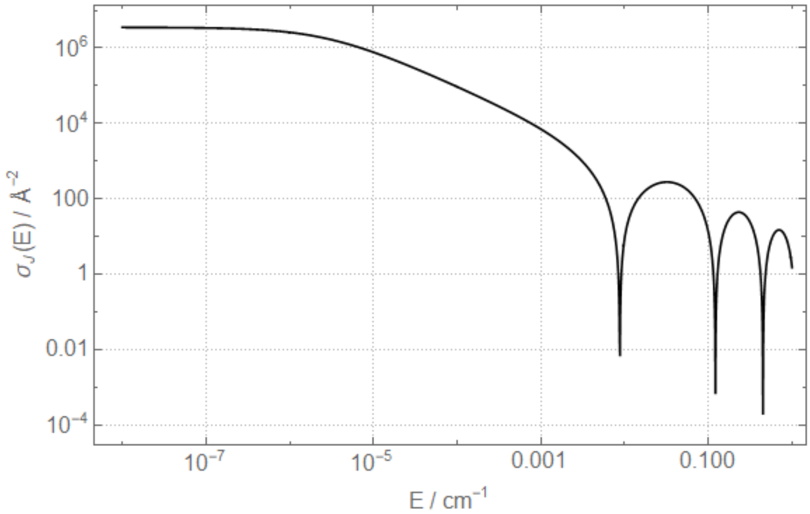

Figure 5.7: Cross-section plot for the $J = 0$ partial wave generated with the MD potential. The plot is placed on log-log axes. At low energy the plot exhibits the signature constant scaling behaviour of low-energy scattering.

Figure 5.8 analyses the region of validity of the low-energy linear fit of Equation 2.29. It is designed to re-create a plot shared as private communications by the authors of the paper Barletta *et al.* [15].

The solid, red line of Figure 5.8 represents the eigenphase calculation generated by the RmatReact method, using an R-matrix inner region ranging from $r_{\text{min}} = 2.5$ Å to $a_0 = 82.5$ Å, an integration over 1600 Lobatto grid points, and an R-matrix propagation from $a_0 = 82.5$ Å to $a_p = 165$ Å, with 1,000 propagation iterations. The dashed line represents Equation 2.29, with the parameters A and r_{eff} determined by using a least-squares linear fit of the lower-energy portion of the red line (intercept $= 0.00146$ Å^{-1}, slope $= 18.42$ Å), again using the software Origin. As with Table 5.3, this Figure is in agreement with results provided in private communications by Barletta *et al.* [15], who also computed the scattering length

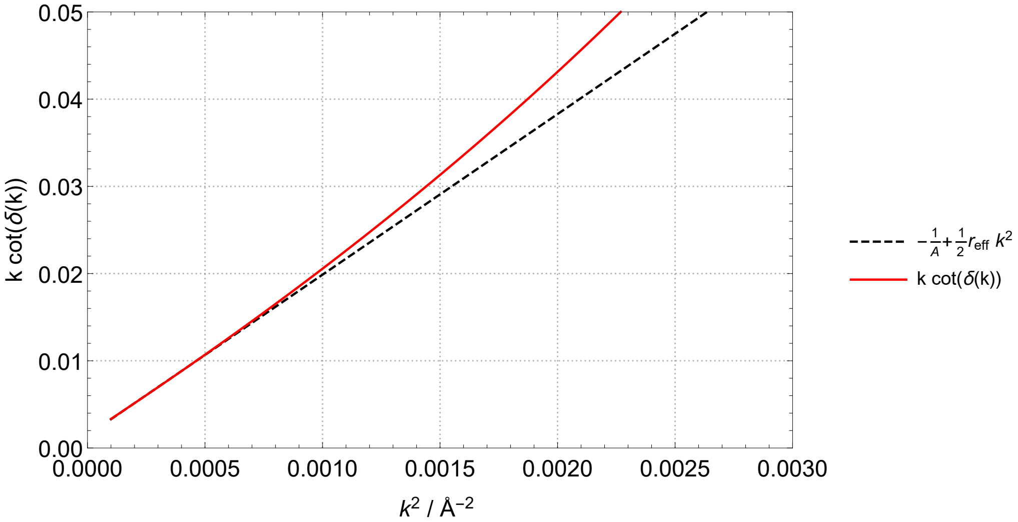

Figure 5.8: Plot of $k\cot\delta(k)$ against k^2 for low values of k using the Az potential.

of the Ar_2 collision based on the potential due to Aziz [121]. It can be seen from Figure 5.8 that the plot is only linear at a very low energy.

A similar low-energy fitting procedure in Origin was performed for all five PECs studied. The values of A and r_{eff} were calculated in this work for the four PECs where corresponding literature values could be obtained, the comparison of which can be seen in Table 5.3.

The effective ranges featured in Table 5.3 all appear to be in broad agreement, as expected since this quantity is not especially sensitive to fine changes to the quantity of the potential, and is not affected significantly by the number of bound states [30].

The values obtained for the scattering length are found to be sensitive to the energy range used in the fitting procedure, and so whilst numbers are quoted in Table 5.3, it should be noted that these numbers are not intended to be definitive. When using the energy range of Figure 5.8 for the low-energy fit, it is possible to obtain the scattering lengths quoted in Barletta *et al.* [15] to within a 5% relative difference. However, when using a much lower energy range for the fit of $k^2 \approx 10^{-10}$ Å^{-2} to $k^2 \approx 10^{-8}$ Å^{-2}, the scattering lengths change significantly. (The effective ranges also change slightly, but are still in agreement.) The values quoted in Table 5.3 are the ones created using the lower energy range fit. As Figure 5.8

Table 5.3: Scattering lengths (A) and effective ranges (r_{eff}) generated using four potentials compared to previous values. For the first three potentials, the scattering lengths and effective ranges cited are from Barletta *et al.* For the fourth potential, the potential and scattering length are from the same source: Myatt *et al.*

Potential	A/Å (literature)	A/Å (this work)	r_{eff} /Å (literature)	r_{eff} /Å (this work)
Az [121]	-505.6	-647.1	35.94	35.53
PM [120]	1285	844.0	33.87	33.53
TT [123]	-60.79	-62.50	50.12	49.20
MD [136]	-714	-709.3	–	35.41

shows, this lower range is where the expansion of Equation 2.29 is most appropriate.

The features seen towards the right of Figure 5.7 correspond to energies where the eigenphase pass through zero. On a log-log plot of the cross-section these crossings manifest as the dips seen in the Figure.

Although the scattering length values significantly diverge from each other, the RmatReact method was able to qualitatively corroborate each one. The PECs in Table 5.3 which have a negative scattering length correspond to PECs for which there are eight bound states in literature (see Table 5.1). The only PEC considered which supports nine bound states, PM [120], has a large, positive scattering length.

This is in line with the observation that the scattering length is strongly affected by the energy of the highest bound state. If the scattering length is plotted as a function of V_{min}, the minimum of the potential, then there is a pole at points where the number of bound states increments by one, going up to positive infinity in one direction and down to negative infinity in the other [30]. The consequence of this is that either side of this pole, the scattering length can be very different: any real number is a potentially valid scattering length.

It is known [186, 120] that relativistic and nonadiabatic effects can impact potential parameters such as the depth of the potential. The different PECs studied in this work all incorporate these effects to different degrees. Whilst this work attempts to verify the scattering observables produced using these potentials, no attempt is made to assess the quality of each potential relative to the other ones. These effects, along with the other sources of uncertainty related to the PECs, are by far the biggest source of uncertainty and error in the results, and contribute much larger error to the numbers quoted here than numerical errors in the algorithm itself.

No previous values are available for the scattering length and effective range of the PS PEC [177]; the scattering length and effective range were calculated, using the same lower energy range fitting as the results in Table 5.3. The scattering length was found to be 1669 Å to four significant figures. This is noteworthy because both this work and Sahraeian *et al.* [181] claim to have detected nine bound states for this system, and so the PS PEC continues the pattern of large, positive scattering lengths for Ar_2 PECs with nine bound states, as seen in Table 5.3. Finally, the effective range was found to be 33.82 Å, in good agreement with most of the other effective ranges cited in the literature and this work.

5.4 S-matrix Poles

As discussed in Chapter 3, reskit [143] was used to find S-matrix poles, which have the potential to correspond to bound states, virtual states, and scattering resonance, and can also provide insights into the scattering length of the system. Using S-matrix poles to identify resonances is a good way to cross-check the resonances cited earlier in this chapter, and using S-matrix poles to detect bound states can also help to shed light on the 'ninth bound state' issue discussed previously.

Because reskit reads in K-matrices using the UKRmol format, PFARM was used to propagate all of the R-matrices in this section. reskit was successful in finding several poles that corresponded to interesting physical phenomena, although it must be noted that, as with other results in this chapter, a large grid was used for the R-matrix inner region before the results were propagated to the asymptotic region.

The $J = 5$, $J = 9$, and $J = 10$ resonances for the MD potential in Table 5.2, which were successfully re-created in this work, were also found using the S-matrix pole method in reskit, using PFARM-produced K-matrices. For each of the three resonances, a pole was located at approximately the correct position. In this case 'correct' is defined as being similar to the resonance positions obtained using other

Table 5.4: Positions E_{res} and widths Γ_{res} of the resonances detected from S-matrix poles using reskit for the MD potential, compared to the results generated in this work using Breit-Wigner fitting.

J	E_{res} /cm^{-1} (reskit)	Γ_{res} /cm^{-1} (reskit)	E_{res} /cm^{-1} (Breit-Wigner)	Γ_{res} /cm^{-1} (Breit-Wigner)
9	0.1287	0.588×10^{-6}	0.1287	0.663×10^{-6}
10	0.4481	0.003003	0.4486(2)	0.00247(46)
5	0.06970	0.004583	0.06993(5)	0.004841(5)

methods, and to the results of Myatt *et al.* [136].

It is worth noting, however, that K-matrix discontinuity and resonance position do not necessarily have a one-to-one correspondence ([117], page 240), as the presence of a varying background eigenphase can affect the position of the discontinuity.

Table 5.4 shows the positions and widths obtained using the S-matrix pole method. The values E_{res} of the resonances obtained using the S-matrix method are systematically lower than those found using the Breit-Wigner functional form. The resonances Γ_{res}, however, all appear to be wider. They are all of similar order of magnitude to the values quoted in Table 5.2, but are not as close to the values in literature as the Breit-Wigner-fitted resonances, despite coming from the same K-matrices. The position and width of the $J = 10$ resonance detected by reskit is also broadly similar to the position of the $J = 10$ resonance cited by Čížek *et al.* [118, 184].

Obtaining the poles corresponding to the resonances was only possible when the energy grid used in PFARM was very dense. For example, for the $J = 5$ state, there is a resonance at approximately 0.448 cm^{-1} with a width of approximately 0.003 cm^{-1}. When the K-matrix used as input for reskit was defined over an energy range of 0.35 cm^{-1} (between 0.36 cm^{-1} and 0.71 cm^{-1}), no pole was detected. But when the range was 0.132 cm^{-1} between 0.395 cm^{-1} and 0.527 cm^{-1} with the same number of points, then the pair of poles was detected. This is despite the resonance looking very prominent in the plot of the K-matrix even in the wider of the two ranges listed here.

The only input to reskit is the K-matrix obtained from PFARM. The only other control the user retains over the algorithm is the ability to change numerical parameters such as tolerance and precision. The same parameters were used in all reskit runs here.

Chapter 3 also mentions that an original S-matrix pole-finding code was written for this work and tested in some circumstances. The testing of this pole finder was limited, but it did detect a pole on the imaginary axis for a real, positive energy of approximately 1×10^{-6} to 3×10^{-6} cm^{-1} when exploring the MD potential's K-matrices. This would seem to suggest that there *is* actually a weakly bound ninth bound state for this potential, contrary to other claims in this chapter.

With respect to ultra-low energy, $J = 0$ S-matrices generated by reskit in this work, reskit was used to generate K-matrices between 1.10×10^{-7} cm^{-1} and 1.10×10^{-4} cm^{-1} along the imaginary axis with 10,000 energy grid points for the four potentials featured in Table 5.3.

Low-energy poles were found for all four potentials for $J = 0$. Three of the potentials supported virtual state poles. In particular, the Az, MD, and TT potentials all had clear virtual state poles on the negative imaginary axis. The Az potential's virtual state pole was located 1.911×10^{-6} cm^{-1} below the origin, the MD potential's virtual state pole 2.791×10^{-6} cm^{-1} below the origin, and the TT potential's 1.577×10^{-6} cm^{-1} below the origin. These values are likely to be prone to some numerical instability. Furthermore, since they do not correspond to physical states, it is not guaranteed that they will have fixed positions with high precision. Notably, the PM potential, which did not support a clear virtual state pole, also had a K-matrix plot as a function of E at these energies that appeared qualitatively different to the other three.

All four potentials had ultra-low-energy poles of a different type for $J = 0$, though. They all had poles which, if they corresponded to a bound state, would have binding energies ranging from 10^{-19} cm^{-1} to 10^{-33} cm^{-1} in energy (assuming their similarly small real-k coordinates were actually zero). These poles clearly cannot be considered accurate representations of the true positions of poles along the imaginary axis. However, it is possible that they represent the presence of another pole (or possibly many poles which are close to each other) along the imaginary axis that reskit was unable to pinpoint precisely [187].

These poles could be either just above or just below the origin, meaning they could represent bound or virtual state poles. Their presence does indicate the presence of *a* low-energy pole (or dense grouping of low-energy poles) for each potential, but does not provide any more information than that. The K-matrix data provided may have been insufficiently precise to determine any more information about these poles. Since reskit was designed to study poles associated with resonances with much larger widths – also with electron-molecule scattering in mind – it should be expected that it would struggle to pinpoint the locations of such narrow poles precisely [187].

A pair of poles was also located in the upper half plane close to and reflected off the imaginary axis for the MD potential for $J = 0$. Taken at face value, they imply a resonance with a negative energy, however it is more likely that, as with the other ultra-low-energy poles, the positions of this pair was not determined with enough precision by reskit, and they may actually represent a pair of poles in the lower half plane. What these poles would represent physically is unclear, too.

It is notable that the only $J = 0$ potential which did not support a clear virtual state pole was the PM potential, which was the only one that was tested using reskit that was expected to support nine bound states. If it is true that virtual states only appear in potentials that have *negative* scattering lengths, and do not appear in the one potential that has both a *positive* scattering length and a ninth bound state, that may be a corroboration of the idea that virtual states are states that are ‘only just’ unbound – the weakly bound ninth bound state in one potential becomes weakly unbound in the others. This would lead to the scattering length value passing through positive infinity and arriving at the large, negative values implied by the results from the Az, MD, and TT potentials.

Chapter 6

Multichannel Oxygen-Helium Scattering

For the multichannel implementation of the RmatReact method, a test system was chosen with nine channels: the scattering of helium atoms off oxygen atoms.

6.1 Intramultiplet Mixing in O-He Collisions

The O-He system was chosen in order to compare results produced by the RmatReact method to literature results of Krems & Buchachenko [137].

In Krems & Buchachenko [137], the authors study the results of collisions between oxygen and helium atoms at energies from 3.0 cm^{-1} down to under 0.1 cm^{-1} above the energy level of the highest state. Specifically, the authors study transitions from the $^3P_0$ state of the oxygen atom (where the term is defined as $^{2S+1}L_j = {}^3P_0$ for atomic spin $S = 1$, atomic orbital angular momentum $L = P = 1$, and atomic total angular momentum $j = 0$) to both its $^3P_1$ and $^3P_2$ states (which both lie below $^3P_0$ in energy [188]), due to collisions with helium in its $^1S_0$ state.

The process by which an atom changes quantum states within a multiplet is known as intramultiplet mixing. Krems & Buchachenko observed structure in the cross-section at these energies, which this work attempts to re-create to prove the effectiveness of the RmatReact method. The spin-orbit couplings used in their work originate in an earlier work by the same authors [108], and the potential energy curves are drawn from the earlier work by Aquilanti *et al.* [124].

Oxygen is an open-shell atom and hence has spin-orbit couplings. The isotopes of oxygen and hydrogen being considered here, ^{16}O and ^{4}He, do not have hyperfine structure, which is the other possible source of spin-orbit couplings in atoms. As mentioned in Chapter 3, DUO was designed to study open-shell systems such as this one.

6.2 Hund's Cases

The potential energy curves presented in Krems & Buchachenko [108] (based on curves initially presented in [124]) are given in Hund's case (c), where it is assumed that the orbital and spin angular momenta **L** and **S** of the diatom are strongly coupled to produce a resultant vector **j**, with quantum numbers L, S and j respectively. Hund's case (c) is used when **L** is more strongly coupled to **S** than it is to the internuclear axis [189].

Hund's case (c) is illustrated in Figure 6.1, based on a similar diagram in Brown & Carrington [189]. **j** is the total internal angular momentum of the diatoms with quantum number j, **R** is the angular momentum due to the rotation of the nuclei around each other, **J** is the total angular momentum of the diatom, which combines **L**, **S** and **R** such that

$$\mathbf{J} = \mathbf{R} + \mathbf{j}. \tag{6.1}$$

The quantum number associated with **J** is J. The quantum number $\tilde{\Omega}$ is the projection of j onto the internuclear axis. Since it is assumed that **R** is perpendicular to the internuclear axis, $\tilde{\Omega}$ is also the projection of J onto the internuclear axis. The definition of **R** here is consistent with Brown & Carrington [189], and the associated quantum number R is equivalent to the quantum number ℓ introduced in Chapter 2 in the space-fixed case.

Note that in the general case the **j** vector has contributions from both atoms in the diatom. However, in the case studied in this chapter (see Section 6.4), it is assumed that $\mathbf{j} = \mathbf{0}$ for one of the two atoms – helium – meaning that **j** effectively represents the total spin + orbital angular momentum of one atom – oxygen – in the diatomic system, making the definition of the quantum number j here consis-

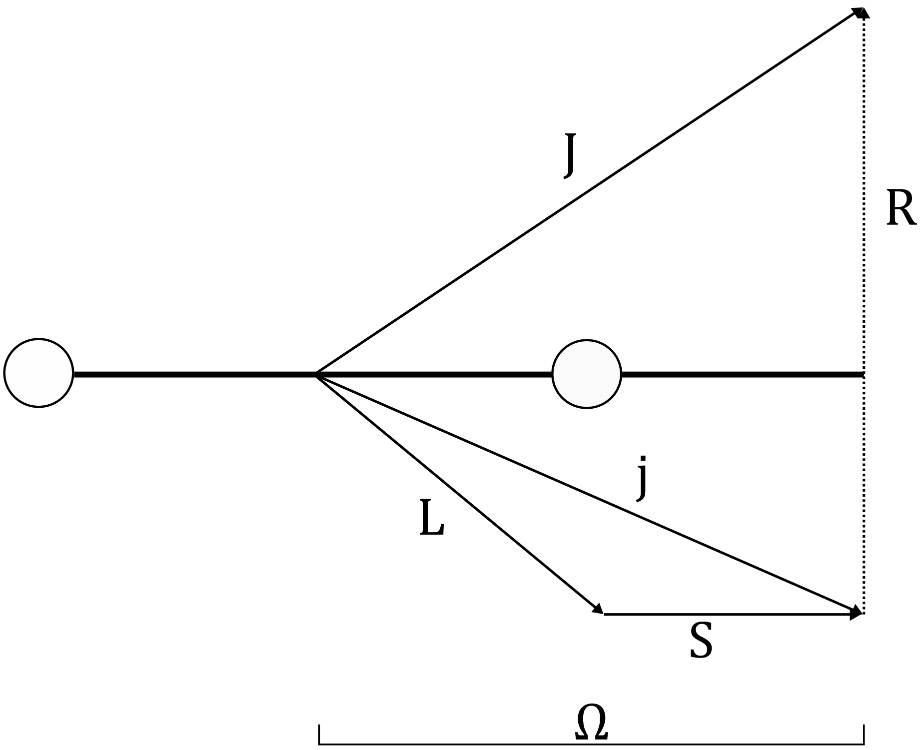

Figure 6.1: Schematic of Hund's Case (c) for a diatomic molecule, based on a similar diagram in Brown & Carrington.

tent with its definition in Figure 6.3. In the general diatomic case, there would be three quantum numbers representing the two total angular momenta of the individual atoms and their sum.

Hund's case (c) is the case where a state can be represented in a basis of the quantum numbers j, $\tilde{\Omega}$, J, and η, where η is a symbol representing all other quantum numbers (e.g. vibrational numbers, electronic state etc.). J and τ, the parity quantum number, are the only truly good quantum numbers in this case, though the others may be assumed to be good in some circumstances (parity will be discussed separately shortly). The different Hund's cases can be distinguished by which quantum numbers are better approximations to good quantum numbers than others. A ket in Hund's case (c) may have the form $|J, j, \tilde{\Omega}, \eta\rangle$ [189, 190]. Note that this is not a formal combination of rotational wavefunctions, but merely a label of states. An accurate combination would actually have the form $|J\tilde{\Omega}M\rangle\,|\eta\tilde{\Omega}\rangle$ [189, 190] (M is the magnetic quantum number – the projection of J onto the space-fixed z-axis – but magnetic fields and space-fixed coordinates are not considered in this work). One key difference here is that j is not explicitly included in the kets – indeed Brown & Carrington [189] imply that j is not as good a quantum number as J and $\tilde{\Omega}$ in case (c).

This problem was studied in a body-fixed frame, where the coordinates are attached to the atoms themselves, and not fixed to some external frame. As a consequence, the angular momentum due to the rotation of the nuclei about each other, $\mathbf{R}$, does not have a projection on the internuclear axis. Instead, a Coriolis effect is present, as discussed by Krems & Buchachenko [108]. The Coriolis terms vary with the J, j, and $\tilde{\Omega}$ quantum numbers in Hund's case (c). Future developments on the RmatReact method would ideally include an option to perform the PFARM calculations in a space-fixed regime, to make it easier to study the effects of external magnetic fields on scattering observables.

Hund's case (a) is the case where it is assumed that $\mathbf{L}$ and $\mathbf{S}$ are more strongly coupled to the internuclear axis than to each other. This is illustrated in Figure 6.2, again based on a figure in Brown & Carrington [189]. The key difference between cases (a) and (c) is that in case (a), it is possible to define two additional quantum numbers: $\tilde{\Lambda}$ and $\tilde{\Sigma}$, which are the projections onto the internuclear axis of $\mathbf{L}$ and $\mathbf{S}$ respectively.

The quantities $\tilde{\Lambda}$, $\tilde{\Sigma}$, and $\tilde{\Omega}$ are signed, and are related by the expression $\tilde{\Lambda} + \tilde{\Sigma} = \tilde{\Omega}$. The absolute values of these three quantum numbers are defined as Λ, Σ, and Ω. One reason for defining these quantities is that the sign of $\tilde{\Omega}$ is not a physical observable, and only the magnitude and relative signs matter. Similarly, the magnitude of Λ is used to label the electronic states in case (a). Furthermore, because $\tilde{\Omega}$ is the projection of J onto the internuclear axis, it follows that $\Omega \leq J$, which, for instance, implies that $\Omega = 2$ states do not exist when $J = 0$ or $J = 1$. The most important reason for defining the absolute values separately is presented in the next section.

Hund's case (a) is the case where a state can be represented in a basis of the good quantum numbers $\tilde{\Lambda}$, S, $\tilde{\Sigma}$, $\tilde{\Omega}$, J, and η. A ket in this basis may have the

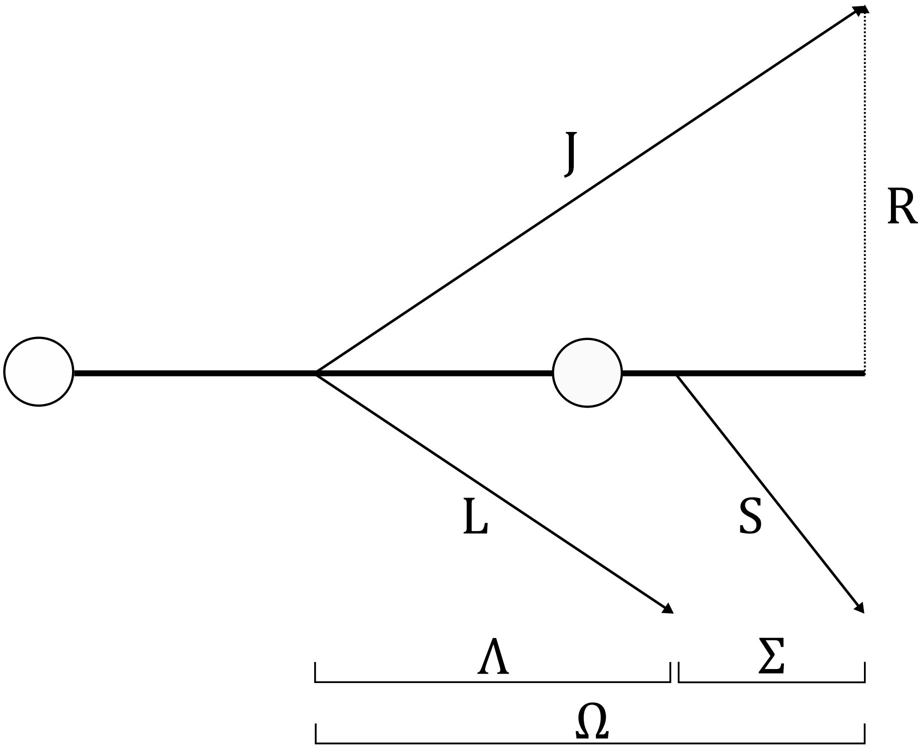

Figure 6.2: Schematic of Hund's Case (a) for a diatomic molecule, based on a similar diagram in Brown & Carrington.

form $|J,\tilde{\Lambda},S,\tilde{\Sigma},\tilde{\Omega},\eta\rangle$ [189, 190]. Again this is an informal labelling of states. The more formally correct combination of kets would have the form $|J\tilde{\Omega}M\rangle\,|n\tilde{\Lambda}\rangle\,|S\tilde{\Sigma}\rangle$ [189, 190].

Hund's case (a) is the case used by DUO in the inner region problem, whereas the outer region calculations were all performed in Hund's case (c). As such, in order to use the potentials in [137], it was necessary to convert them from case (c) to case (a). Furthermore, in order to use the results from DUO in PFARM, it was then necessary to convert the problem back into case (c).

Intuitively speaking, Hund's case (a) and Hund's case (c) are well-suited to treatments of the inner- and outer-regions of the method respectively. This is because in case (a), the individual components of each atom's angular momenta couple more strongly to each other than to other components of their atom's angular momentum – in other words, they act more like a single diatom than as a combination of two separate atoms, and are thus more amenable to being studied using DUO.

By contrast, Hund's case (c) represents the case where it is more sensible to refer to the total angular momentum of an individual atom that is also coupled to another individual atom. This makes it the more sensible choice for representing channel functions and asymptotic states of separate atoms in a scattering problem [191]. Of course, both cases are simply making different approximations. If a full basis is being used, problems solved in the two cases should converge on the same answers.

Fortunately, the conversion between cases (a) and (c) is the simplest of the conversions between the five Hund's cases, since cases (c) and (a) are the only cases where it is possible to separate the electronic and nuclear motions unambiguously in the Born-Oppenheimer approximation [189]. The transformation of a potential matrix in case (a), $\mathbf{V}_{(\mathrm{a})}$, to one in case (c), $\mathbf{V}_{(\mathrm{c})}$, can be achieved by performing the operation

$$\mathbf{V}_{(\mathrm{c})} = \mathbf{U}\mathbf{V}_{(\mathrm{a})}\mathbf{U}^{\dagger}, \tag{6.2}$$

where $\mathbf{U}$ is the unitary matrix composed of the normalised eigenvectors of the matrix of spin-orbit terms in case (a), and $\mathbf{U}^{\dagger}$ is its Hermitian conjugate. The harness code discussed in Chapter 3 performs this transformation. The inverse transformation from case (c) to case (a) can be performed by left-multiplying the case (c) matrix by $\mathbf{U}^{\dagger}$ and right-multiplying by $\mathbf{U}$. An example of the form the matrix $\mathbf{U}$ can take is given in Section 6.4.

The unitary matrix and its Hermitian conjugate can also be used to transform the individual channel amplitudes evaluated at a_0 of the R-matrix sum from case (a) to case (c) and back. If a vector of channel amplitudes in case (a), $\boldsymbol{\psi}_{(\mathrm{a})}$, is constructed, the equivalent vector in case (c) is given by

$$\boldsymbol{\psi}_{(\mathrm{c})}(a_0) = \mathbf{U}\boldsymbol{\psi}_{(\mathrm{a})}(a_0), \tag{6.3}$$

and the inverse transformation is performed using the Hermitian conjugate matrix.

6.3 Parity Adapting the Basis

In DUO, only the complete wavefunctions are eigenfunctions of the parity operator. The amplitudes of individual channel functions that DUO sums over to obtain these wavefunctions are not. Because in this work the channel amplitudes themselves are required, parity is not a good quantum number in the DUO outputs. This is why in the kets quoted in the previous section, the parity quantum number, τ, is not included. Kato [192] does describe how to construct eigenfunctions of the parity operator in Hund's case (a) from the ket $|J, \tilde{\Lambda}, S, \tilde{\Sigma}, \tilde{\Omega}, \eta\rangle$, and this can also be combined with other sources [193, 194, 190, 195] to infer how to transform the ket $|J, j, \tilde{\Omega}, \eta\rangle$. This is because Kato (and indeed DUO itself [86]) describes how the parity operator acts on these kets. In Hund's case (a), the parity operator $\sigma_v(xz)$ (abbreviated to σ_v henceforth) has the effect:

$$\sigma_v |J, \tilde{\Lambda}, S, \tilde{\Sigma}, \tilde{\Omega}, \eta\rangle = (-1)^{s-\Lambda+S-\Sigma+J-\Omega} |J, -\tilde{\Lambda}, S, -\tilde{\Sigma}, -\tilde{\Omega}, \eta\rangle, \qquad (6.4)$$

where s is a quantum number that is only non-zero for Σ^- symmetry electronic states, none of which are featured in this problem. Furthermore, because $S = 1$ always in this problem, and because $\tilde{\Lambda} + \tilde{\Sigma} = \tilde{\Omega}$, in this work the equation can be reduced to

$$\sigma_v |J, \tilde{\Lambda}, S, \tilde{\Sigma}, \tilde{\Omega}, \eta\rangle = (-1)^{J+1} |J, -\tilde{\Lambda}, S, -\tilde{\Sigma}, -\tilde{\Omega}, \eta\rangle. \qquad (6.5)$$

The parity operator σ_v has the effect of a reflection through the molecule-fixed xz plane, which, when applied to rotational eigenfunctions in the molecule-fixed frame, is equivalent to the general parity inversion operator E which simply inverts all three Cartesian coordinates [192, 195].

Equation 6.5 allows one to construct parity eigenstates. Again following Kato [192], and suppressing the S and η labels for simplicity,

$$|J, p, \Lambda, \Sigma, \Omega\rangle = \frac{1}{\sqrt{2}} \left(|J, \tilde{\Lambda}, \tilde{\Sigma}, \tilde{\Omega}\rangle + (-1)^p |J, -\tilde{\Lambda}, -\tilde{\Sigma}, -\tilde{\Omega}\rangle \right). \qquad (6.6)$$

In other words, normalised linear combinations of $+\tilde{\Omega}$ and $-\tilde{\Omega}$ states are in one parity block when one is added to the other, and in the other parity block when one is subtracted from the other.

Note that the implication of this is that in the ket $|J, p, \Lambda, \Sigma, \Omega\rangle$, the signs of the projections are no longer necessary – the basis functions are no longer eigenfunctions of the operator which distinguishes these signs. These observables do not have absolute signs anyway – only relative ones. This equation also defines the parity quantum number τ, which can be either 0 or 1. In order to assign these kets to a parity eigenstate, the eigenvalue of the parity operator σ_v, τ, can be defined in case (a) as

$$\tau_{(\mathrm{a})} = (-1)^{J+1+p}, \tag{6.7}$$

which can take values of ± 1 for the two different values of p, and is dependent on the total angular momentum J.

There is one additional parity eigenstate which must be separately noted. Equation 6.6 is only valid for the case where both Λ and Σ are non-zero. If both are zero (making Ω equal to zero, too), then the parity eigenstate only has one term in it, specifically

$$|J, p, \Lambda = 0, \Sigma = 0, \Omega = 0\rangle = |J, \Lambda = 0, \Sigma = 0, \Omega = 0\rangle . \tag{6.8}$$

The Hund's case (a) parity conversion procedure is well-established. It can also be used to deduce the equivalent parity conversion in Hund's case (c). In Hund's case (c), the parity-adapted basis is given by [193, 194, 195, 190]

$$|J, p, j, \Omega\rangle = \frac{1}{\sqrt{2}} \left(|J, j, \tilde{\Omega}\rangle + (-1)^{j+p} |J, j, -\tilde{\Omega}\rangle \right) . \tag{6.9}$$

The key difference between Equation 6.6 and Equation 6.9 is that the former raises -1 to the power of p whereas the latter raises it to $j + p$. As in 6.6, in Equation 6.9 only the absolute value of the Ω projection is required in the parity-adapted basis. The Hund's case (c) parity eigenvalue assignment when J is an integer is given by

$$\tau_{(c)} = (-1)^{J+p}. \tag{6.10}$$

Similar to case (a), there is also an s value in the exponent in Equation 6.10 which is not included explicitly here, as it is only non-zero for a Hund's case (c) ground state electronic wavefunction, 0^-, that is equivalent to the Σ^- state in case (a), which is not used in this work [190, 196].

As with case (a), there is an additional parity eigenstate which must be considered separately. In case (a), only the state with $\Lambda = 0$, $\Sigma = 0$, and $\Omega = 0$ must be considered separately. However in case (c), it is *all* states with $\Omega = 0$ that must be considered separately. Hund's case (c) wavefunctions with $\Omega = 0$ in the parity-adapted basis are given by [190]:

$$|J, p, j, \Omega = 0\rangle = |J, j, \Omega = 0\rangle. \tag{6.11}$$

Using Equation 6.6, it is possible to construct parity-adapted amplitudes from the amplitudes produced by DUO for the inner region, which can then be passed to the R-matrix sum. There are still as many channels as before, but they have different quantum numbers. The equation also describes how to assign the quantum numbers to the new states.

The choices of which states to subtract from which in Equation 6.6 and Equation 6.9 are arbitrary, as long as consistency is maintained. In this work, states with negative $\tilde{\Omega}$ values were subtracted from states with positive $\tilde{\Omega}$ values in both Hund's cases, and the Hund's case (a) state with $\tilde{\Lambda} = 1$ and $\tilde{\Sigma} = -1$ was subtracted from the state with $\tilde{\Lambda} = -1$ and $\tilde{\Sigma} = 1$.

The transformation from Hund's case (a) to Hund's case (c), which was implemented in the harness code as described in Equation 6.2, actually took place in the parity-adapted bases of the two cases: the Hund's case (a) spin-orbit matrix was transformed into the parity-adapted basis in the harness code, and then it was diagonalised to obtain the transformation matrix. This transformation matrix was then applied to the potential matrix in Hund's case (a) to obtain the parity-adapted

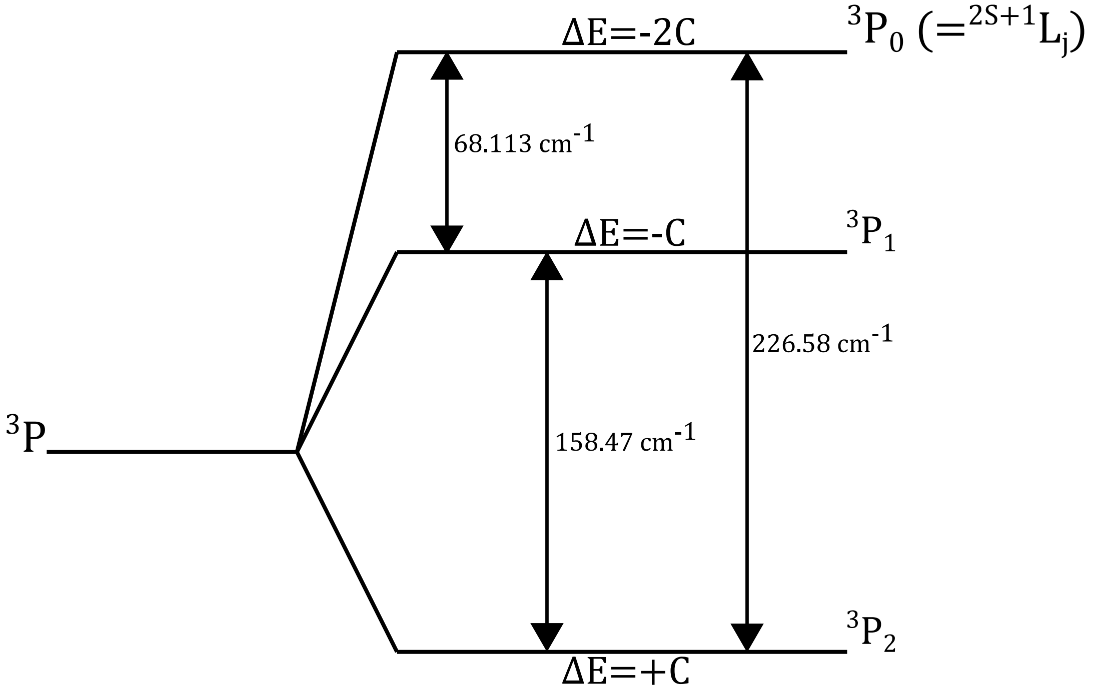

Figure 6.3: Term diagram for the ^3P state of oxygen, and its splitting into fine structure levels by the spin-orbit interaction. The spin transition values are from Berrington, where the energy of the ^3P level is taken to be 0 cm^{-1}. C is the constant matrix element of the spin-orbit matrix operator in Hund's case (a).

Hund's case (c) matrix. It was also shown to be possible to perform the transformations in the opposite order – to transform the un-parity-adapted Hund's case (a) amplitudes to Hund's case (c), and then perform the parity adaptation on those amplitudes. With an appropriate choice of parity considerations as discussed above, the parity-adapted Hund's case (c) amplitudes obtained were the same either way.

6.4 The O-He System

The scattering problem under consideration here is one where the spin-orbit interaction splits the ^3P state of the oxygen atom into three components, each with different values of j. In decreasing order of energy, these are $^3P_0$, $^3P_1$, and $^3P_2$, as seen in Figure 6.3. When oxygen in this state forms a diatom with helium in the $^1S_0$ state (such that $S = 0$, $L = 0$ for helium), then the total spin and orbital angular momenta of the diatom, L and S, are both 1.

This means that the projections in Hund's case (a), $\tilde{\Lambda}$, and $\tilde{\Sigma}$, can have the values -1, 0, or $+1$, with their sum, $\tilde{\Omega}$, having possible values of $-2,-1,0,1$, or 2. As a result, there are nine possible sets of quantum numbers $\tilde{\Lambda}$, $\tilde{\Sigma}$, and $\tilde{\Omega}$ that the resulting diatom can have (see Table 6.2).

In the parity-adapted basis of Hund's case (a), the nine channels divide into two parity sub-blocks, one with five channels and one with four channels. The $p=0$ block is the larger block and the $p=1$ block is the smaller block (the larger and smaller blocks are called the *e*-block and *f*-block respectively by some authors [190]).

The electronic Hamiltonian for the system in case (a) in body-fixed coordinates [107] contains only electronic potential energy curves in the Born-Oppenheimer approximation, and spin-orbit coupling terms.

Since there are nine channels, the Hamiltonian is given by a 9×9 matrix made of a kinetic operator $\mathbf{T}^{\Gamma}_{\mathrm{(a)}}$, a diagonal matrix of electronic PECs $\mathbf{V}^{\Gamma}_{\mathrm{el(a)}}$, a matrix of spin-orbit couplings $\mathbf{V}^{\Gamma}_{\mathrm{SO(a)}}$, and, because this Hamiltonian is being defined in a body-fixed frame, there is also a matrix of Coriolis Force coupling terms $\mathbf{F}^{\Gamma}_{\mathrm{Co(a)}}$ which forms part of the kinetic operator:

$$\mathbf{H}^{\Gamma}_{\mathrm{(a)}} = \mathbf{T}^{\Gamma}_{\mathrm{(a)}} + \mathbf{V}^{\Gamma}_{\mathrm{el(a)}} + \mathbf{V}^{\Gamma}_{\mathrm{SO(a)}} + \mathbf{F}^{\Gamma}_{\mathrm{Co(a)}}. \tag{6.12}$$

Γ in this case refers to a given combination of the conserved quantum numbers J and p, and so this equation is valid for a given symmetry. Unlike the potential and spin-orbit matrices, the Coriolis matrix will only be expressed in Hund's case (c) in this chapter, since in Hund's case (a) it is handled internally by DUO as part of the kinetic operator, not the potential operator, and it is not derived explicitly in this work.

It is only possible to access all nine channels when $J\geq 2$, due to the $\Omega\leq J$ rule discussed above. As such, when $J=0$, the 9×9 matrix is reduced to a 3×3 one where only states with $\Omega=0$ are allowed, and when $J=1$, the matrix is reduced to a 7×7 one where only states with $\Omega=0$ and $\Omega=1$ are allowed. And, as discussed above, even in the $J\geq 2$ case, the matrix is divided by parity into two sub-matrices, one of which is 4×4 and the other of which is 5×5. This also implies that in the $J=1$ case, the 7×7 matrix is divided into a 4×4 matrix and a 3×3 matrix, and in the $J=0$ case the matrix is divided into a 2×2 matrix and a 1×1 matrix.

In Hund's case (a), the matrix of electronic PECs, $\mathbf{V}^{\Gamma}_{\text{el(a)}}$, is diagonal, and has only two distinct elements. All diagonal elements for which $\Lambda=0$ are given by V_Σ, and all diagonal elements for which $\Lambda=1$ are given by V_Π.

The two PECs which are labelled by their Λ values, V_Σ and V_Π, are defined in terms of two other PECs, labelled V_0 and V_2. They are given by [124]

$$V_0(r) = \varepsilon \begin{cases} f_{\text{Morse}} & r \le r_1 \\ f_{\text{Spline}} & r_1 < r < r_2 \\ f_{\text{vdW}} & r_2 \le r \end{cases} \tag{6.13}$$

$$V_2(r) = A_2 e^{-\alpha_2 r} - \frac{C_2}{r^6}, \tag{6.14}$$

where

$$f_{\text{Morse}} = e^{-2\frac{\beta}{r_m}(r-r_m)} - 2e^{-\frac{\beta}{r_m}(r-r_m)} \tag{6.15}$$

$$f_{\text{Spline}} = b_1 + \frac{1}{r_m}(r-r_1)\left(b_2 + \frac{1}{r_m}(r-r_2)\left(b_3 + \frac{1}{r_m}(r-r_1)b_4\right)\right) \tag{6.16}$$

$$f_{\text{vdW}} = -\frac{C_0}{\varepsilon r^6}. \tag{6.17}$$

The values of the parameters ε, r_1, r_2, A_2, α_2, C_2, β, r_m, b_1, b_2, b_3, b_4, and C_0 are all provided in Aquilanti *et al.* [124], and displayed in Table 6.1 (note that R_m here is expressed as r_m, and $r_1 = x_1 r_m$ and $r_2 = x_2 r_m$).

V_Σ and V_Π themselves are given by [124]

$$V_\Sigma(r) = V_0(r) + \frac{2}{5}V_2(r) \tag{6.18}$$

$$V_\Pi(r) = V_0(r) - \frac{1}{5}V_2(r). \tag{6.19}$$

Note that the long-range forms of the V_0 and V_2 potentials are both van der Waals r^{-6} potentials. The coefficients are C_0 and C_2, respectively. As such, the

Parameter	Value
$\varepsilon/\mathrm{cm}^{-1}$	16.938
$r_1/\mathrm{Å}$	3.597
$r_2/\mathrm{Å}$	4.6434
A_2/cm^{-1}	274460
$\alpha_2/\mathrm{Å}^{-1}$	3.4865
$C_2/\left(\mathrm{cm}^{-1}\mathrm{Å}^6\right)$	6177.4
β	6.5
$r_m/\mathrm{Å}$	3.27
b_1	-0.7716
b_2	1.8949
b_3	-4.2150
b_4	1.4838
$C_0/\left(\mathrm{cm}^{-1}\mathrm{Å}^6\right)$	28084

Table 6.1: The parameters from Aquilanti *et al.* used to define $V_0(r)$ and $V_2(r)$ in Equations 6.13 and 6.14, with a value of 8.0655445769 used to convert from millielectronVolts to wavenumbers. Where units are not provided, the parameter is dimensionless.

long-range forms of V_Σ and V_Π (and any linear combinations of them) are given by the linear combinations of these coefficients implied by eq. (6.18) and eq. (6.19).

The spin-orbit matrix in Hund's case (a) is entirely defined through one constant, C. Its value can be determined by averaging the experimental values for the fine structure splittings of the ^3P state of oxygen. In Krems & Buchachenko [108], the two values are quoted as $\Delta_1 = 158.1\ \mathrm{cm}^{-1}$ and $\Delta_0 = 226.6\ \mathrm{cm}^{-1}$ for the $^3P_2 \to {}^3P_1$ and $^3P_2 \to {}^3P_0$ transitions, respectively. By taking (the negative of) the average of half of Δ_1 and a third of Δ_0, one obtains a value of $C = -77.29\ \mathrm{cm}^{-1}$. This is the value used in this work. Note that the values used in [108] are slightly different to those quoted in Figure 6.3. Taking (the negative of) an average of those values produces $C = -77.38\ \mathrm{cm}^{-1}$.

C and $-C$ are the values of the matrix elements of the spin-orbit operator. This is explained by Kato [192], where it is also explained how to determine which off-diagonal matrix elements are C, and which are zero, and which diagonal elements are $+C$ term, which are $-C$ term, and which are zero.

The full potential energy matrix for the potential in Hund's case (a) is given by

	(0,-1,-1)	(0,0,0)	(0,1,1)	(-1,-1,-2)	(-1,0,-1)	(-1,1,0)	(1,-1,0)	(1,0,1)	(1,1,2)
(0,-1,-1)	V_Σ				C				
(0,0,0)		V_Σ				C	C		
(0,1,1)			V_Σ					C	
(-1,-1,-2)				$V_\Pi+C$					
(-1,0,-1)	C				V_Π				
(-1,1,0)		C				$V_\Pi-C$			
(1,-1,0)		C					$V_\Pi-C$		
(1,0,1)			C					V_Π	
(1,1,2)									$V_\Pi+C$

Table 6.2: The potential matrix in Hund's case (a). The quantum numbers in brackets are $\left(\tilde{\Lambda},\tilde{\Sigma},\tilde{\Omega}\right)$. $C=-77.29$ cm^{-1}. V_Σ and V_Π are defined by Equation (6.18) and Equation (6.19) respectively.

	(0,0,1,1)	(0,0,0,0)	(0,1,1,0)	(0,1,0,1)	(0,1,1,2)
(0,0,1,1)	V_Σ			C	
(0,0,0,0)		V_Σ	$\sqrt{2}C$		
(0,1,1,0)		$\sqrt{2}C$	$V_\Pi-C$		
(0,1,0,1)	C			V_Π	
(0,1,1,2)					$V_\Pi+C$

Table 6.3: The upper parity block of the parity-adapted potential matrix in Hund's case (a). The quantum numbers in brackets are $(p,\Lambda,\Sigma,\Omega)$. $C=-77.29$ cm^{-1}. V_Σ and V_Π are defined by Equation (6.18) and Equation (6.19) respectively.

Table 6.2. The functionality required to generate the matrix in Table 6.2 is provided by DUO. When DUO is provided with one off-diagonal, and one on-diagonal spin-orbit curve (here all spin-orbit curves are constant with values either C or $-C$), it can use the rules provided by Kato [192] to determine all the spin-orbit matrix elements [86], making the conversion from Hund's case (c) to Hund's case (a) much simpler.

When transforming the Hund's case (a) basis functions into the parity-adapted basis, Equations 6.6 and 6.8 also describe how to transform the elements of the

	(1,0,1,1)	(1,1,1,0)	(1,1,0,1)	(1,1,1,2)
(1,0,1,1)	V_Σ		C	
(1,1,1,0)		$V_\Pi-C$		
(1,1,0,1)	C		V_Π	
(1,1,1,2)				$V_\Pi+C$

Table 6.4: The lower parity block of the parity-adapted potential matrix in Hund's case (a). The quantum numbers in brackets are $(p,\Lambda,\Sigma,\Omega)$. $C=-77.29$ cm^{-1}. V_Σ and V_Π are defined by Equation (6.18) and Equation (6.19) respectively.

potential matrix and the spin-orbit matrix. This transformed matrix is given by the two Tables 6.3 and 6.4.

The reason there are two tables is that the parity-adapted matrix can be divided into two blocks, each containing states with a different parity quantum number τ. Whether the $\tau = \pm 1$ parity block corresponds to $p = 0$ or $p = 1$ depends on whether J is even or odd. If J is even, then $p = 1$ corresponds to $\tau = +1$ and $p = 0$ corresponds to $\tau = -1$. The inverse is true when J is odd.

In Hund's case (c) in body-fixed coordinates, the full potential energy matrix in the Hamiltonian again has two components: electronic and spin-orbit, and the kinetic matrix has a set of Coriolis coupling elements, such that:

$$\mathbf{H}^{\Gamma}_{(\mathrm{c})} = \mathbf{T}^{\Gamma}_{(\mathrm{c})} + \mathbf{V}^{\Gamma}_{\mathrm{el(c)}} + \mathbf{V}^{\Gamma}_{\mathrm{SO(c)}} + \mathbf{F}^{\Gamma}_{\mathrm{Co(c)}}. \tag{6.20}$$

As with Hund's case (a), some channels are inaccessible when $J = 0$ and $J = 1$ due to the $\Omega \leq J$ rule, and the matrix sub-divides into parity blocks when transformed into the parity-adapted basis.

Unlike in case (a), the elements of the electronic matrix $\mathbf{V}^{\Gamma}_{\mathrm{el(c)}}$ cannot be simply assigned by their Λ value, as this is no longer a good quantum number. Instead, every diagonal element is a linear combination of V_{Λ} and V_{Σ} functions, and can be determined from the transformation in Equation 6.2.

Furthermore, the electronic matrix now has off-diagonal components, which are also linear combinations of these two functions. Specifically, they depend on the difference between V_{Σ} and V_{Π}. Because the two potentials are solely composed of r^{-6} terms at long distance that tend towards zero as r tends to infinity, at asymptotic distances there are no couplings between channels. This is what one would expect for two separated atoms which cannot exchange angular momentum. This is why Hund's case (c) is preferable for calculating asymptotic region scattering observables – the atoms can be regarded as separate at asymptotic distances.

In Hund's case (c), the spin-orbit terms are confined to the diagonal. There are three possible values the spin-orbit matrix's elements can have: $-2C$, $-C$, or C. These are the eigenvalues of the matrix of spin-orbit terms in Hund's case (a).

These eigenvalues are determined using Equation 6.2. In this problem, it is possible to uniquely determine the quantum numbers associated with each state in the transformed matrix: for a given Γ, each eigenvector that $\mathbf{U}$ is composed of has a unique $\left(j,\tilde{\Omega}\right)$ assignment. The j value can be determined from the associated eigenvalue, and the $\tilde{\Omega}$ values can be determined from properties and symmetries of the components of the matrix in both the parity-adapted and non-parity adapted cases. This means that each amplitude in the eventual R-matrix sum will have a unique quantum number assignment, too.

All channels for which $j = 0$ have the spin-orbit term $-2C$, all channels for which $j = 1$ have the term $-C$, and the state which has $j = 2$ has the term C. There is five-fold degeneracy in the $j = 2$ term, and three-fold degeneracy in the $j = 1$ term, as one would expect given the number of distinct $\tilde{\Omega}$ projections each j value has. The same is true in the parity-adapted basis due to parity considerations.

When $J = 0$, the eigenvalues of the spin-orbit coupling matrix are $-2C$, $-C$, and $-C$, due to the fact that the $\Omega \geq 1$ states are inaccessible. This suggests that the allowed quantum numbers are $(j = 0, \Omega = 0)$, $(1,0)$, and $(2,0)$. When $J = 1$, the eigenvalues are $-2C, -C, -C, -C, C, C, C$, with quantum numbers $(0,0)$, $(1,0)$, $(1,-1)$, $(1,1)$, $(2,0)$, $(2,-1)$, $(2,1)$. When $J \geq 2$, all nine eigenvalues are allowed: $-2C, -C, -C, -C, C, C, C, C, C$, and all nine quantum number combinations are allowed: $(0,0)$, $(1,0)$, $(1,-1)$, $(1,1)$, $(2,0)$, $(2,-1)$, $(2,-2)$, $(2,2)$, $(2,1)$. In the parity-adapted basis, the states cannot be distinguished by the sign of Ω, but instead each state also has a parity label, thus making unique assignments still possible by assigning states with non-zero $+\tilde{\Omega}$ to the opposite block to states with $-\tilde{\Omega}$.

The nine channels with three distinct energy values define the *target states* of the scattering problem. The three energy levels correspond to ${}^3P_0$, ${}^3P_1$, and ${}^3P_2$, as seen in Figure 6.3. Because $V_\Sigma(r)$ and $V_\Pi(r)$ are zero in the asymptotic limit of r, the potential matrix has no V_Σ or V_Π terms at asymptotic distances, meaning the only terms left are the constant spin-orbit terms on the diagonal.

In the Hund's case (c) representation, it was decided that the experimental values of the target states' energies should be used, instead of the C value obtained from averaging them. As such, in the full potential matrix table in both the non-parity-adapted and parity-adapted bases, Table 6.5, the spin-orbit matrix's elements are not given in terms of C, but in terms of Δ_j, which is defined as the difference in energy between the ${}^3P_j$ and ${}^3P_2$ states (meaning that $\Delta_2 = 0$). Berrington [188] cites values for Δ_1 and Δ_0 of 158.47 and 226.58, respectively, and [108] cites the similar values quoted above. The Δ_j values are the ones used on the diagonal of the Hund's case (c) spin-orbit matrix in Table 6.5.

To illustrate how these transformations work in practice, the transformation matrix $\mathbf{U}$ that transforms the non-parity-adapted case (a) wavefunctions into non-parity-adapted case (c) wavefunctions is presented here. The exact form of the matrix is dependent on the order the channels are listed in, and whether the value of J is less than 2. Choosing an arbitrary order for the case (a) wavefunctions $\psi_{\left(\tilde{\Lambda},\tilde{\Sigma},\tilde{\Omega}\right)}$ and the case (c) wavefunctions $\psi_{\left(j,\tilde{\Omega}\right)}$, the $J \geq 2$ form of Equation 6.3 is

$$\begin{pmatrix} \psi_{(0,0)} \\ \psi_{(1,0)} \\ \psi_{(1,-1)} \\ \psi_{(1,1)} \\ \psi_{(2,0)} \\ \psi_{(2,-1)} \\ \psi_{(2,-2)} \\ \psi_{(2,2)} \\ \psi_{(2,1)} \end{pmatrix} = \begin{pmatrix} 0 & -\frac{1}{\sqrt{3}} & 0 & \frac{1}{\sqrt{3}} & 0 & 0 & 0 & 0 & \frac{1}{\sqrt{3}} \\ 0 & 0 & 0 & \frac{1}{\sqrt{2}} & 0 & 0 & 0 & 0 & -\frac{1}{\sqrt{2}} \\ \frac{1}{\sqrt{2}} & 0 & 0 & 0 & 0 & 0 & 0 & -\frac{1}{\sqrt{2}} & 0 \\ 0 & 0 & -\frac{1}{\sqrt{2}} & 0 & \frac{1}{\sqrt{2}} & 0 & 0 & 0 & 0 \\ 0 & \sqrt{\frac{2}{3}} & 0 & \frac{1}{\sqrt{6}} & 0 & 0 & 0 & 0 & \frac{1}{\sqrt{6}} \\ \frac{1}{\sqrt{2}} & 0 & 0 & 0 & 0 & 0 & 0 & \frac{1}{\sqrt{2}} & 0 \\ 0 & 0 & 0 & 0 & 0 & 0 & 1 & 0 & 0 \\ 0 & 0 & 0 & 0 & 0 & 1 & 0 & 0 & 0 \\ 0 & 0 & \frac{1}{\sqrt{2}} & 0 & \frac{1}{\sqrt{2}} & 0 & 0 & 0 & 0 \end{pmatrix} \begin{pmatrix} \psi_{(0,-1,-1)} \\ \psi_{(0,0,0)} \\ \psi_{(0,1,1)} \\ \psi_{(1,-1,0)} \\ \psi_{(1,0,1)} \\ \psi_{(1,1,2)} \\ \psi_{(-1,-1,-2)} \\ \psi_{(-1,0,-1)} \\ \psi_{(-1,1,0)} \end{pmatrix} . \tag{6.21}$$

In Equation 6.21, for the states with $j = 1$, there is a possible phase difference that can arise depending on the overall sign assigned to the individual eigenvectors. For example, the state $\psi_{\left(j=1,\tilde{\Omega}=-1\right)}$ can be constructed by either subtracting the state $\psi_{\left(\tilde{\Lambda}=0,\tilde{\Sigma}=-1,\tilde{\Omega}=-1\right)}$ from the state $\psi_{(-1,0,-1)}$, or vice-versa.

As with the parity adaptation sums, there is a certain arbitrariness to this choice. Once the overall sign of the $\psi_{\left(j=1,\tilde{\Omega}=-1\right)}$ state is determined, ladder operators can be used to derive what the appropriate signs of the $\psi_{(1,0)}$ and $\psi_{(1,1)}$ states should be, since the $\mathbf{j}_+$ ladder operator can be written as a sum of the $\mathbf{L}_+$ and $\mathbf{S}_+$ operators [196]. The convention used here is based on the convention used with the Clebsch-Gordan coefficients that arise from adding the ladder operators [196]. These signs have implications for the overall signs of the off-diagonal spin-orbit coupling terms in Table 6.5. The convention used here results in the same signs as in the table produced by Krems & Buchachenko [108].

For comparison, the unitary matrices that transform the parity-adapted case (a) wavefunctions into the parity-adapted case (c) wavefunctions can also be presented. Again the exact form of the matrix is dependent on the order the channels are listed in. For $J \geq 2$, the 5×5 and 4×4 matrices that transform the parity-adapted case (a) wavefunctions $\psi_{(p,\Lambda,\Sigma,\Omega)}$ into the parity-adapted case (c) wavefunctions $\psi_{(p,j,\Omega)}$ are given by

$$\begin{pmatrix} \psi_{(0,0,0)} \\ \psi_{(0,1,1)} \\ \psi_{(0,2,2)} \\ \psi_{(0,2,1)} \\ \psi_{(0,2,0)} \end{pmatrix} = \begin{pmatrix} 0 & -\frac{1}{\sqrt{3}} & \sqrt{\frac{2}{3}} & 0 & 0 \\ \frac{1}{\sqrt{2}} & 0 & 0 & -\frac{1}{\sqrt{2}} & 0 \\ 0 & 0 & 0 & 0 & 1 \\ \frac{1}{\sqrt{2}} & 0 & 0 & \frac{1}{\sqrt{2}} & 0 \\ 0 & \sqrt{\frac{2}{3}} & \frac{1}{\sqrt{3}} & 0 & 0 \end{pmatrix} \begin{pmatrix} \psi_{(0,0,1,1)} \\ \psi_{(0,0,0,0)} \\ \psi_{(0,1,1,0)} \\ \psi_{(0,1,0,1)} \\ \psi_{(0,1,1,2)} \end{pmatrix} \tag{6.22}$$

and

$$\begin{pmatrix} \psi_{(1,1,1)} \\ \psi_{(1,1,0)} \\ \psi_{(1,2,2)} \\ \psi_{(1,2,1)} \end{pmatrix} = \begin{pmatrix} -\frac{1}{\sqrt{2}} & 0 & \frac{1}{\sqrt{2}} & 0 \\ 0 & 1 & 0 & 0 \\ 0 & 0 & 0 & 1 \\ \frac{1}{\sqrt{2}} & 0 & \frac{1}{\sqrt{2}} & 0 \end{pmatrix} \begin{pmatrix} \psi_{(1,0,1,1)} \\ \psi_{(1,1,1,0)} \\ \psi_{(1,1,0,1)} \\ \psi_{(1,1,1,2)} \end{pmatrix}. \tag{6.23}$$

The same parity considerations apply here, too. Since the $\psi_{(p=1,j=1,\Omega=1)}$ state exists in the same parity block as the $\psi_{(1,1,0)}$ state, it is assumed that the $\psi_{(1,1,1)}$ state has the same sign convention as the $\psi_{\left(j=1,\tilde{\Omega}=1\right)}$ state of Equation 6.21, and the $\psi_{(p=0,j=1,\Omega=1)}$ state has the same sign convention as the $\psi_{\left(j=1,\tilde{\Omega}=-1\right)}$ state. Again, this has implications for the signs of the off-diagonal elements of Table 6.6 and Table 6.7.

The final set of elements which are included in the potential matrix are the Coriolis coupling terms. These elements couple different Ω states, and arise due to the body-fixed reference frame this derivation is performed in. In the non-parity-adapted basis, a matrix element of the centrifugal Coriolis operator can be written as

$$\langle J, j, \Omega' | CF | J, j, \Omega \rangle = F_{Jj\Omega\Omega'}(r), \tag{6.24}$$

since the Coriolis operator does not couple different j states.

The values of these matrix elements depend on J and j, and the expression is given by:

$$F_{Jj\Omega\Omega'}(r) = \begin{cases} \frac{\hbar^2}{2\mu r^2}\left(J(J+1)+j(j+1)-2\Omega^2\right) & \Omega = \Omega'. \\ -\frac{\hbar^2}{2\mu r^2}\sqrt{J(J+1)-\Omega\Omega'}\sqrt{j(j+1)-\Omega\Omega'} & \Omega' = \Omega \pm 1. \\ 0 & \text{otherwise.} \end{cases} \tag{6.25}$$

Note that Equation 6.25, which is derived from Krems & Buchachenko [108], implies that for all values of Ω and Ω', $F_{J\Omega\Omega'}$ is the same if a signed version of Ω is used, and both Ω values are replaced with their negatives, so only the absolute value of Ω is required. Furthermore, the equation is symmetric to the exchanging of Ω with Ω', meaning that $F_{Jj\Omega\Omega'} = F_{Jj\Omega'\Omega}$.

The potential matrix and the amplitudes in Hund's case (c) can also be parity-adapted. As with case (a), the parity-adapted matrix can be split into blocks, and the τ assignment of the blocks is dependent on whether J is odd or even.

In the parity-adapted Hund's case (c) basis, the Coriolis coupling elements can be assigned a p label. It can be shown that states in different p-blocks do not have any non-zero Coriolis coupling matrix elements, such that

$$\langle J, p, j, \Omega' | CF | J, p, j, \Omega \rangle = F_{Jpj\Omega\Omega'}(r). \tag{6.26}$$

The elements have new forms which can be expressed in terms of the old forms.

	(2,-2)	(2,-1)	(2,0)	(2,1)	(2,2)	(1,-1)	(1,0)	(1,1)	(0,0)
(2,-2)	V_Π $+F_{J222}$	F_{J221}							
(2,-1)	F_{J212}	$\frac{1}{2}(V_\Sigma+V_\Pi)$ $+F_{J211}$	F_{J210}			$\frac{1}{2}(V_\Sigma-V_\Pi)$			
(2,0)		F_{J201}	$\frac{1}{3}(V_\Pi+2V_\Sigma)$ $+F_{J200}$	F_{J201}					$\frac{\sqrt{2}}{3}(V_\Pi-V_\Sigma)$
(2,1)			F_{J210}	$\frac{1}{2}(V_\Sigma+V_\Pi)$ $+F_{J211}$	F_{J212}			$\frac{1}{2}(V_\Pi-V_\Sigma)$	
(2,2)				F_{J221}	V_Π $+F_{J222}$				
(1,-1)		$\frac{1}{2}(V_\Sigma-V_\Pi)$				$\frac{1}{2}(V_\Sigma+V_\Pi)$ $+\Delta_1+F_{J111}$	F_{J110}		
(1,0)						F_{J101}	V_Π $+\Delta_1$ $+F_{J100}$	F_{J101}	
(1,1)				$\frac{1}{2}(V_\Pi-V_\Sigma)$			F_{J110}	$\frac{1}{2}(V_\Sigma+V_\Pi)$ $+\Delta_1+F_{J111}$	
(0,0)			$\frac{\sqrt{2}}{3}(V_\Pi-V_\Sigma)$						$\frac{1}{3}(2V_\Pi+V_\Sigma)$ $+\Delta_0+F_{J000}$

Table 6.5: The full potential matrix in Hund's case (c) for when $J \geq 2$, with the Coriolis coupling terms featured too, based on the matrix in Krems & Buchachenko. The quantum numbers in brackets are (j,Ω). V_Σ and V_Π are the same as in Table (6.2). $F_{Jj\Omega\Omega'}$ is given by Equation 6.25.

There are still no Coriolis couplings between different values of j.

For the off-diagonal elements, the symmetry of Equation 6.25 suggests that the acts of swapping Ω and Ω', or of changing the sign of both Ω and Ω' simultaneously has no effect on the form of $F_{Jp\Omega'\Omega}$. If either one of Ω or Ω' is zero, then changing the sign of the other has no effect either. These facts have implications for the effect of the parity transformation on the matrix elements. Because in the non-parity-adapted case only off-diagonal elements where Ω and Ω' differ by 1 are non-zero, the expressions for the parity-adapted Coriolis terms are:

$$F_{Jpj\Omega'\Omega}(r) \quad = \quad \begin{cases} F_{Jj\Omega'\Omega} & \Omega = \Omega'. \\ \sqrt{2}F_{Jj\Omega'\Omega} & \Omega' = \Omega \pm 1,\ (\Omega \text{ or } \Omega') = 0,\ p = 0. \\ F_{Jj\Omega'\Omega} & \Omega' = \Omega \pm 1,\ (\Omega \text{ and } \Omega') \neq 0. \\ 0 & \text{otherwise.} \end{cases}$$

The full potential matrix in the parity-adapted Hund's case (c) is given by the

	(0,0,0)	(0,1,1)	(0,2,2)	(0,2,1)	(0,2,0)
(0,0,0)	$\frac{1}{3}(2V_\Pi + V_\Sigma)$ $+\Delta_0 + F_{J000}$				$\frac{\sqrt{2}}{3}(V_\Sigma - V_\Pi)$
(0,1,1)		$\frac{1}{2}(V_\Sigma + V_\Pi)$ $+\Delta_1 + F_{J111}$		$\frac{1}{2}(V_\Sigma - V_\Pi)$	
(0,2,2)			V_Π $+F_{J222}$	F_{J221}	
(0,2,1)		$\frac{1}{2}(V_\Sigma - V_\Pi)$	F_{J212}	$\frac{1}{2}(V_\Sigma + V_\Pi)$ $+F_{J211}$	$\sqrt{2}F_{J210}$
(0,2,0)	$\frac{\sqrt{2}}{3}(V_\Sigma - V_\Pi)$			$\sqrt{2}F_{J201}$	$\frac{1}{3}(V_\Pi + 2V_\Sigma)$ $+F_{J200}$

Table 6.6: The potential matrix in Hund's case (c), based on the matrix in Krems & Buchachenko, in the parity-adapted basis. The states are labelled by (p, j, Ω). This is the upper portion of the matrix for when $J \geq 2$ and J is odd.

	(1,1,1)	(1,1,0)	(1,2,2)	(1,2,1)
(1,1,1)	$\frac{1}{2}(V_\Sigma + V_\Pi)$ $+\Delta_1 + F_{J111}$	$\sqrt{2}F_{J110}$		$\frac{1}{2}(V_\Pi - V_\Sigma)$
(1,1,0)	$\sqrt{2}F_{J101}$	V_Π $+\Delta_1 + F_{J100}$		
(1,2,2)			V_Π $+F_{J222}$	F_{J221}
(1,2,1)	$\frac{1}{2}(V_\Pi - V_\Sigma)$		F_{J212}	$\frac{1}{2}(V_\Sigma + V_\Pi)$ $+F_{J211}$

Table 6.7: The parity-adapted potential matrix in Hund's case (c). This is the lower portion of the matrix for when $J \geq 2$ and J is odd.

Tables 6.6 and 6.7. These two matrices represent the upper and lower parts of the matrix. Note that there are fewer Coriolis coupling terms overall than in the full matrix without parity-adjustment. It was these potential matrices that were input into PFARM.

6.5 Results for O-He Scattering

PFARM produces T-matrices as a function of energy E with elements $T^{J\tau}_{(j,\Omega)\to(j',\Omega')}(E)$, for transitions for a given set of conserved quantum numbers J and τ between channels with quantum numbers (j,Ω) and (j',Ω'). Using Equation 2.40, these T-matrix elements can then be used to construct partial cross-sections for a given symmetry $\{J\tau\}$, which can then be summed using Equation 2.39 to give a total cross-section. Substituting the generic channel label i featured in Equation 2.40 and Equation 2.39 with the specific quantum numbers used in this chapter, an expression for the partial cross-section for a given channel can be produced:

$$\sigma^{J\tau}\left(j\rightarrow j'\right)(E)=\frac{\pi}{k_j^2}\frac{1}{(2j+1)}\sum_{\Omega}|T^{J\tau}_{(j,\Omega)\rightarrow(j',\Omega')}(E)|^2. \tag{6.27}$$

The sum in Equation 6.27 is over all of the transitions $(j,\Omega)\rightarrow(j',\Omega')$ from channels with j to channels with j' which are allowed by parity.

In Equation 6.27, k_j is the scattering wavenumber associated with channel j, and it is defined in terms of the scattering energy E_{tot} and the channel energy E_j by:

$$k_j^2=\frac{2\mu}{\hbar^2}(E_{\text{tot}}-E_j). \tag{6.28}$$

The total cross-section can be constructed by summing over the partial cross sections up to some maximum J value J_{max} and including the degeneracy factor:

$$\sigma^{\text{Tot}}\left(j\rightarrow j'\right)(E)=\sum_{J=0}^{J_{\text{max}}}\sum_{\tau}(2J+1)\sigma^{J\tau}\left(j\rightarrow j'\right)(E). \tag{6.29}$$

Some eigenphase sums were also produced for testing purposes. As discussed in Section 2.1.3.2, these were obtained by diagonalising the K-matrix for a given symmetry at a given energy, and summing the arctangents of the eigenvalues of that K-matrix.

6.5.1 Numerical Testing

Tests were performed on the inner region diagonalisation and outer region propagation portions of the method to ensure stability and convergence in the results. To test convergence, cross-sections were generated using a specific set of numerical parameters, and these cross-sections were compared to each other. When a cross-section was found to be negligibly different upon the altering of a numerical parameter, that parameter was said to be converged.

In the inner region, the number of grid points used, N, which equals the number of functions used in the diagonalisation, was tested, as was the size of the grid and the position of r_{min} and a_0. In the multichannel case, the number of eigenfunctions must be equal to the number of grid points used for *each* potential. It was found that the results were converged when $N = 100$ for a sufficiently large grid, meaning that 100 grid points and 100 basis functions were used per potential. The value of r_{min} was not tested, and kept constant at 2.0 Å, but the value of a_0 was varied. It was found to be convergent at $a_0 = 8.0$ Å and above.

In the outer region, there were four variables to consider, including a_0, which, as the boundary between the regions, also counts as an outer region variable. One other variable, a_p, can be comfortably identified with the a_p defined in previous chapters as the propagation distance in other propagation methods such as the Light-Walker method. However, the BBM propagator employed by PFARM has two variables instead of the single Δr_{prop} variable discussed in Chapter 4. Because the BBM propagator works by dividing the outer region into smaller sections and diagonalising each of those individually, the two variables that must be considered are the number of sectors, called N_{sect}, and the number of basis functions used in the diagonalisation in each sector, called N_ℓ due to the fact that the basis set used in PFARM is a Legendre polynomial basis.

In order to converge N_{sect}, it was found that the size of each section, $(a_p - a_0)$ divided by N_{sect}, was important to keep low. In particular, if $\frac{(a_p - a_0)}{N_{\text{sect}}}$ was equal to approximately 5.0 Å, this was insufficiently converged. Sectors of 3.0 Å or lower were required to converge the results. It was found that N_ℓ was converged for values of 30 or above.

The value of a_p, and the difference between a_p and a_0, were both found to be important factors. The difference between a_p and a_0 was important because it affected the size of the propagation grid, and therefore the size of individual sectors. For this reason, despite the fact that a_0 was converged for 8.0 Å, a value of a_0 which was almost double that was used in the actual calculations. But the value of a_p was important in itself. If it was placed insufficiently far out, then the results were not converged.

A large value of a_p was found to be needed. Results were not converged until a_p was approximately 150 Å, and a value of a_p close to 250 Å was ultimately used to generate the results in this section. This is not entirely unexpected, given the low energies being considered. Indeed there is precedent for up to 10^5 atomic units being needed to converge ultracold results for certain systems with very long-range potentials [197].

Finally, the number of partial waves needed to converge the results was also explored, and so the maximum value of J used, J_{max} was tested. A larger number of partial waves was needed to generate the results here than in the previous chapters, because the results being studied here, whilst technically ‘ultracold’ relative to the $j = 0$ threshold, are still hundreds of cm^{-1} above the $j = 2$ threshold, and so a large number of partial waves are non-zero for non-trivial portions of the energy ranges tested. Different numbers of partial waves were used at different energies, after they were tested for convergence.

6.5.2 Comparisons with Literature

The results presented here were constructed to be compared with results by Krems & Buchachenko [137], and by Monteiro & Flower [198]. These authors studied the intramultiplet mixing of oxygen due to collisions with helium to test a selection rule that dramatically alters the amplitude of the cross-section of the $j = 0 \rightarrow j = 1$ transition relative to the amplitude of the cross-section of the $j = 0 \rightarrow j = 2$ transition. One reason why the fine structure of oxygen is important is because fine-structure transitions within the ^{3}P level of oxygen are relevant to the study of interstellar clouds, and oxygen-helium collisions are likely to be common in these systems [199].

The selection rule states that the $0 \rightarrow 1$ transition in collisions is forbidden to a first order approximation [198]. Unlike transitions between the $j = 0$ and $j = 2$ states, which are permitted by electrostatic couplings in the system, the only matrix elements which permit transitions between the $j = 0$ and $j = 1$ states in the body-fixed frame are the Coriolis couplings discussed above [137], and so one would expect the cross-section of these transitions to be smaller.

The older Monteiro & Flower paper only provided a few numbers which are relevant to the temperatures being considered here. Table 6.8 provides some of the numbers from that paper, alongside the equivalent numbers produced here. The

Table 6.8: Cross-sections for various transitions produced by Monteiro & Flower, and produced in this work. Here, E is measured relative to the energy of the $j = 2$ state.

E /cm^{-1}	j	j'	$\sigma^{\mathrm{Tot}}(j \to j')$ /Å^2 (Literature)	$\sigma^{\mathrm{Tot}}(j \to j')$ /Å^2 (This work)
200	1	2	3.64	3.65
240	0	1	0.025	2.02
240	0	2	5.60	63.7
240	1	2	4.17	8.32

results presented in this table were produced using partial waves from $J = 0$ to $J = 15$, with 100 inner region eigenfunctions and grid points, $r_{\mathrm{min}} = 2.0$ Å, $a_0 = 15.0$ Å, $a_p = 264.6$ Å, 96 outer region diagonalisation sectors with 30 Laguerre functions each, and 32 partial waves for two values of τ and 16 values of J.

Monteiro & Flower claim that their calculations converged rapidly with respect to J, although they do not explicitly state how many partial waves they used. Furthermore, the potential energy curves and energy positions of the j sublevels used in their paper are different to the ones used in this work ($j = 1$ is located at 158.5 cm^{-1} and $j = 0$ is at 226.5 cm^{-1} in their work), and so exact agreement should not be expected. This does not explain the discrepancy between the results produced in this work and most of the numbers in Table 6.8, which remains unresolved.

The other authors whose results were compared against the results produced here were Krems & Buchachenko. Two cross-section plots were produced by them, showing the $0 \to 2$ and $0 \to 1$ transitions at low temperatures. Their plots are between 0 cm^{-1} and 3 cm^{-1}, although it is unclear how far above zero they computed down to to produce the lower end of their plots. The energies were measured relative to the threshold energy of the $j = 0$ state: 226.6 cm^{-1}, as they report it. Those plots were re-created here. Note that the threshold values used in this work were 158.47 cm^{-1} for $j = 1$ and 226.58 cm^{-1} for $j = 2$, after Berrington [188]. However, testing using the 158.1 cm^{-1} and 226.6 cm^{-1} values used by Krems & Buchachenko showed no difference in the final results. The same potential energy curves that were used to produce their cross-sections [124, 108] were also used in this work.

Figure 6.4 shows the $0 \to 1$ cross-section produced in this work, and Figure 6.5 shows the $0 \to 2$ cross-section. 21 partial waves from $J = 0$ to $J = 20$ were used to generate these figures from 0.001 cm^{-1} above the threshold energy of the $j = 0$ state to 3 cm^{-1} above it. The numerical parameters used were 100 inner region eigenfunctions and grid points, $r_{\text{min}} = 2.0$ Å, $a_0 = 15.0$ Å, $a_p = 264.6$ Å, 96 outer region diagonalisation sectors with 30 Laguerre functions each, and 42 partial waves for two values of τ and 21 values of J.

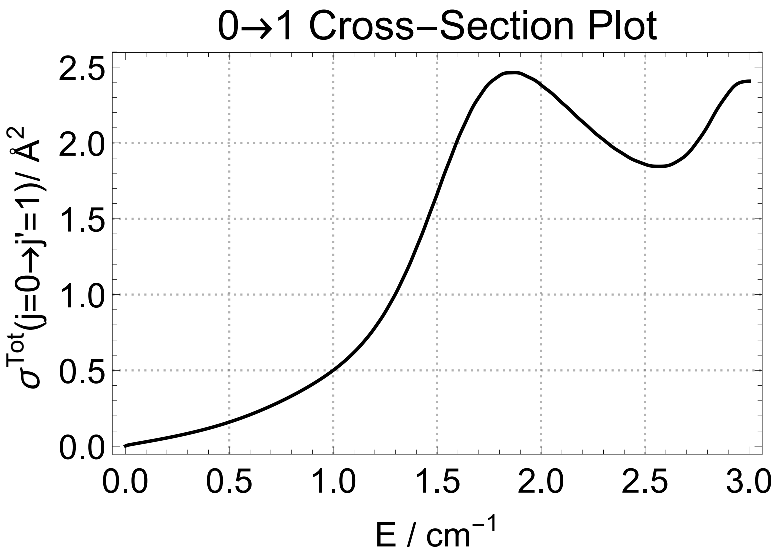

Figure 6.4: The total $j = 0$ to $j = 1$ cross-section as a function of energy relative to the $j = 0$ threshold at 226.58 cm^{-1}.

The value of J_{max} that was used to generate these results was chosen after testing for convergence. Figures 6.6 and 6.7 show the partial waves used in the sum. For each value of J, only one of the two parity states contributed to the sum. This is because the larger parity block contains the $j = 0$ state and the smaller one does not, as Tables 6.6 and 6.7 show. This means that the contributions to the $0 \to 1$ and $0 \to 2$ transitions only come from the partial wave with the larger parity block, and so these partial waves are the ones represented in Figures 6.6 and 6.7.

It is clear that the largest values of J used had negligible contributions to the magnitude of the cross-section. This is even more visible in Figures 6.8 and 6.9, which show how the total cross-section for the transitions changes as more partial

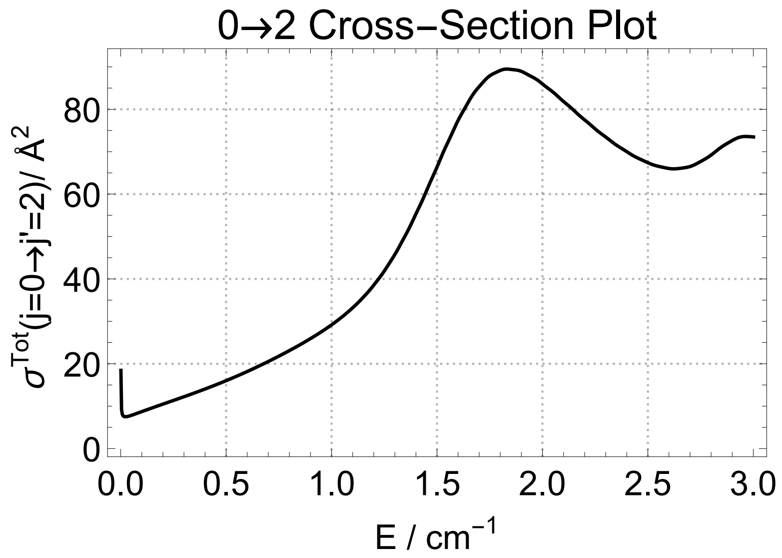

Figure 6.5: The total $j = 0$ to $j = 2$ cross-section as a function of energy relative to the $j = 0$ threshold at 226.58 cm^{-1}.

waves are added, and which is clearly converged by the time the last few partial waves are included. It is also clear that resonances exist in the $J = 9$ and $J = 16$ partial waves for both transitions, which significantly affects the shape of the converged total cross-sections.

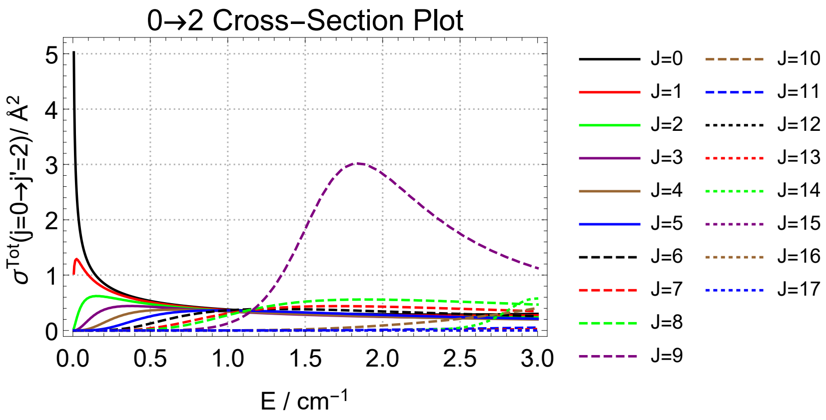

Figure 6.6: The partial waves for $J = 0$ to $J = 17$ for the $j = 0$ to $j = 2$ transition over the energy range studied.

There are two resonances that are visible in Krems & Buchachenko's plots (which both have the same overall structure), both of which are not visible in the plots produced here. Instead, the two resonances due to the $J = 9$ and $J = 16$ partial waves are visible in the two cross-section plots produced here, as demonstrated by

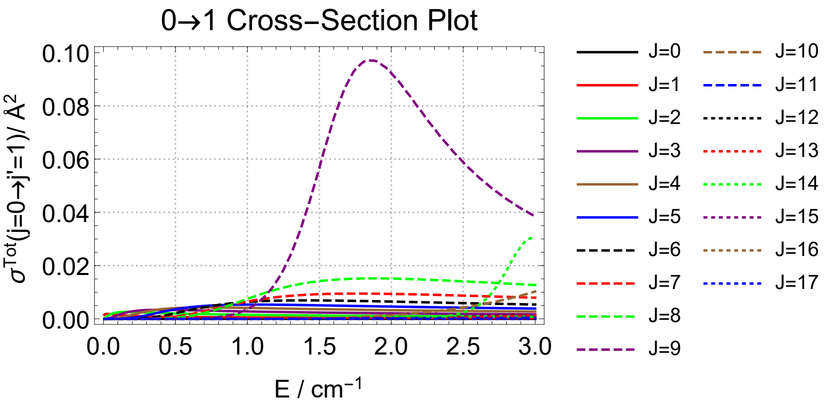

Figure 6.7: The partial waves for $J = 0$ to $J = 17$ for the $j = 0$ to $j = 1$ transition over the energy range studied.

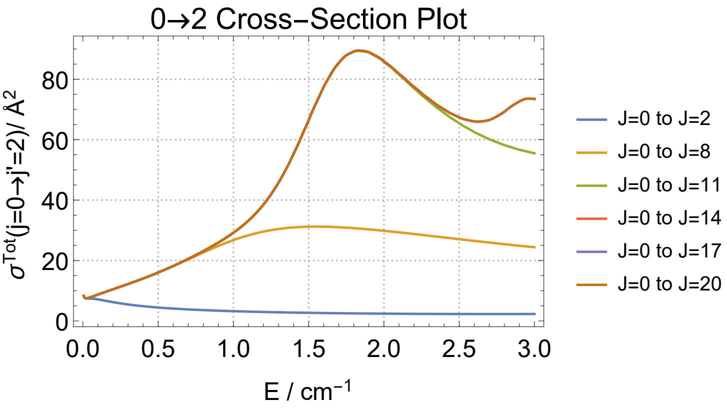

Figure 6.8: The total cross-sections for $J_{\max} = 2$ to $J_{\max} = 17$ for the $j = 0$ to $j = 2$ transition over the energy range studied. The final two lines overlap, proving that the sum is converged.

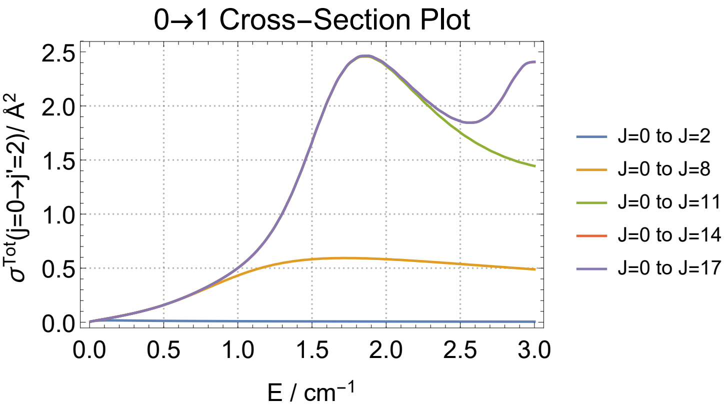

Figure 6.9: The total cross-sections for $J_{\max} = 2$ to $J_{\max} = 17$ for the $j = 0$ to $j = 1$ transition over the energy range studied. The final two lines overlap, proving that the sum is converged.

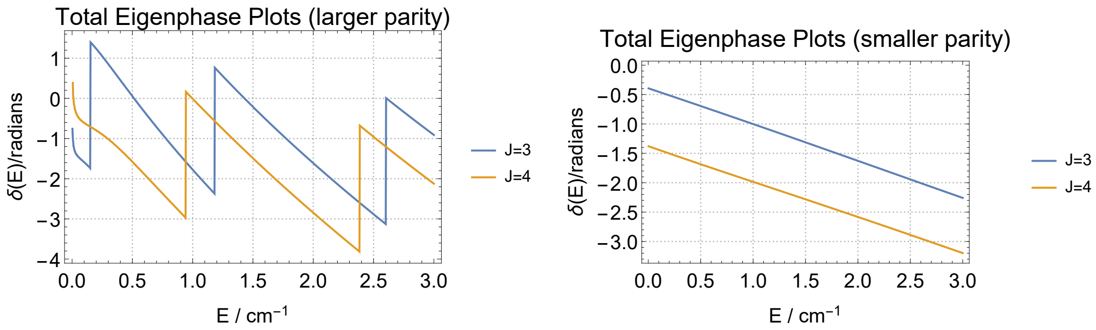

Figure 6.10: The total eigenphase sums for the $J = 3$ and $J = 4$ partial waves, for both parity values, over the same energy range as the cross-section plots above.

Figures 6.6, 6.7, 6.8, and 6.9.

This is difficult to compare directly with the plots in the paper, as they display their partial waves in space-fixed coordinates, labelled by the ℓ quantum number, (equivalent to the ℓ and R numbers defined in this work). Since $\mathbf{J} = \boldsymbol{\ell} + \mathbf{j}$, the partial cross-sections labelled by J in this work can be compared, if only indirectly, to the partial cross-sections labelled by ℓ in their paper. They claim to see resonance structure in the $\ell = 3$ and $\ell = 4$ partial waves for the $0 \rightarrow 2$ and $0 \rightarrow 1$ transitions, meaning the $J = 3$ and $J = 4$ eigenphases produced in this work should have resonant structure for the appropriate parity value.

Figure 6.10 shows the total eigenphase for $J = 3$ and $J = 4$ (modulo π), for the two parity blocks. Only the larger parity block contributes structure to the cross-sections involving the $j = 0$ state, and this effect is clearly seen in Figure 6.10, with different-shaped eigenphases and more low-energy structure in the larger parity block partial wave. However, these plots do not show any signs of resonances, as one would expect for results that corroborate those produced by Krems & Buchachenko.

Figure 6.11 shows the $J = 9$ and $J = 16$ eigenphases (which have been adjusted by π where appropriate to remove discontinuities). These are the partial waves which do appear to contain resonance structure in the cross-section plots. Of these two partial wave eigenphases, only $J = 9$ appears to have any resonance structure. The width of this resonance was estimated to be approximately 0.77 cm^{-1}, and its

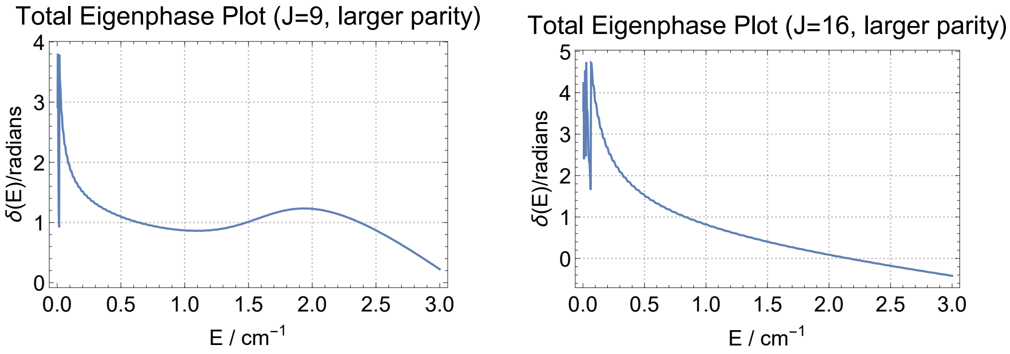

Figure 6.11: The eigenphases for the $J = 9$ and $J = 16$ partial waves, where resonance structure is expected.

position was estimated to be approximately 1.95 cm^{-1} above the $j = 0$ threshold.

Figure 6.11 also displays clear numerical instability in the low-to-ultralow-energy portions of the plots. This suggests that these figures are not entirely correct and that there are processes occurring at low energy which interfere with the normal functioning of the method.

As such, the results in this section are preliminary. Whilst some of the numbers agree with literature sources, others do not. Although the forms of the plots presented in Figures 6.4 and 6.5 do not match those presented by Krems & Buchachenko, the most important result – the disparity in magnitude between the $0 \to 2$ and $0 \to 1$ cross-sections due to the selection rule – is accurately reproduced in the results presented here.

There are several possible explanations for the discrepancy. Whilst testing has showed convergence in the numerical parameters, it cannot be ruled out that simple programming errors are to blame. At the time of submission, there are a handful of known outstanding issues with the results that could hint at solutions to these concerns. Firstly, even when converged and propagated to 500 Å, there are small oscillations in the partial cross-sections that follow the overall shape of the cross-sections but reduce in size as a_p is increased. This suggests that, even though the overall shape of the cross-section is unchanged at the high values of a_p used to generate the results in this section, the actual numbers being generated are still slightly noisy. This is shown in Figure 6.12 for one partial wave, using the same numerical parameters as those used to generate Figures 6.4 and 6.5.

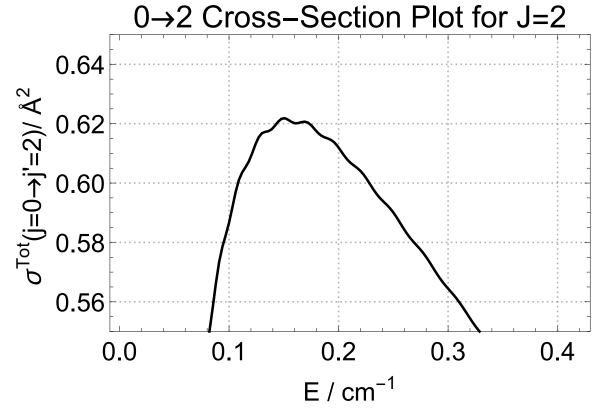

Figure 6.12: The $j = 0$ to $j = 2$ cross-section for the $J = 2$ partial wave as a function of energy relative to the $j = 0$ threshold at 226.58 cm^{-1}. The unphysical oscillations can clearly be seen.

Finally, one other observed inconsistency in the results is that some of the eigenphases generated seem to be unstable at low-energy, especially those for higher values of J, as seen in Figure 6.11. The fact that some of these eigenphases were unphysical and unstable at low energy suggests that some of the low-energy results generated here are not to be considered final. It is for this reason that the beginning of Figure 6.5 was not plotted for values of E closer to the $j = 0$ threshold, which would likely have revealed a much larger peak in the cross-section as the energy tended to the threshold.

Chapter 7

Conclusions

7.1 This Work

At its core this thesis was a work of method development: a new method was constructed to simulate ultracold heavy particle scattering, specifically the scattering of atoms off other atoms at sub-kelvin temperatures.

The project did, however rely extensively on some pre-existing codes. As such, it contains both original code projects, and modifications to existing code structures, with, for instance, the outputs of DUO adapted to be used as inputs for PFARM. In the case of DUO, these modifications have been made available on GitHub. In the case of PFARM, the unmodified version of PFARM is available on GitLab, and the modifications made to it will be released in time.

Whilst the final version of the RmatReact method presented here heavily utilises DUO and PFARM (and to a lesser extent reskit), this work did involve a large amount of construction of new code to replicate the functionality of DUO, PFARM, and reskit. This was primarily in order to test the outputs of these codes, but some results were also generated using purely original codes, especially in Chapter 4.

Alongside the codes that were developed, the project also involved theoretical work. A significant amount of new methodology and algorithms needed to be developed to adapt the pre-existing codes to the new physical problems which they were not originally designed to accommodate.

The simplest instance of this was the need to add reduced mass terms to all of the theoretical work which had been written with electron-atom and electron-molecule problems in mind, and the subsequent need to modify PFARM to account for these reduced mass terms.

The more involved instance of this was the need to change the basis sets used by DUO to account for the boundary condition problems caused by the default settings of DUO when applied to this new problem. This involved extensive work to research different Gaussian quadratures and their associated basis functions.

In solving the assorted numerical and computational issues that arose in this project, a number of interesting insights were obtained into the nature of the R-matrix method in general and RmatReact in particular. Some examples include the extreme dependence on the specific form of the potential energy curves that arise in certain scattering results, the often poorly understood artificial boundary conditions that are intrinsic to the R-matrix, and the wide implications of the choice of quadrature polynomial in the numerics of the methods they are used in.

The results obtained for analytic scattering off Morse potentials in Chapter 4 were the first successful examples of the implementation of the methods presented here. Most importantly, the results proved that the method was at all viable – something that was not guaranteed before the project began.

But another important insight obtained from the analytic Morse results was the quantification of the limits of the numerics of the method, as summarised in Figure 4.5. These insights were useful as the project moved onto more realistic potential energy curves. For instance, it was shown that the results from the method were only valid if the inner region average grid spacing was sufficiently small, and that the error did not decrease when the grid spacing was lowered after a certain threshold spacing was reached. This is in contrast to the grid spacing in the outer region when using the Light-Walker propagator, where there was a clear monotonic decrease in error was the grid spacing was lowered.

Similarly, when the R-matrix boundary a_0 and the asymptotic distance a_p were allowed to vary, the error decreased as the boundary was moved further out, but the effect was not as dramatic as the equivalent effect in the grid spacing. There was still a 'cutoff' value of a_0 after which the error did not vary as much, which is related to the 'capturing the bound states' problem discussed in Section 3.3.6.

The argon-argon elastic scattering results in Chapter 5 were the first accurate results obtained which were applicable to a real physical system. The resonance positions and the scattering length cited in the paper of Myatt *et al.* [136] had their values confirmed by the methods used in this work, as were most of the resonance widths. By corroborating the results obtained in other simulations of this system, it was shown that the methods developed here could potentially be used to obtain new results of physical significance in the future.

Additionally, by using two different resonance finding methods – the Breit-Wigner form and the S-matrix poles – to probe the resonances of the argon-argon system, a better understanding of the utility of the methods themselves was obtained. The limits of the S-matrix-pole-finding code reskit were also tested with the search for the narrow, low-energy poles thought to exist for the different potentials of the Ar_2 system.

Furthermore, additional insights were provided into some long-standing unresolved questions concerning the qualitative features of this particular system by confirming features found by other authors. In particular, the highly divergent scattering lengths and the 'ninth bound state' problem were studied, and results presented here were found to agree with those of other authors such as Barletta *et al.* [15].

It was found that the scattering observables obtained in the calculations were extremely sensitive to the specific potentials being used. This is consistent with a generally observed trend in ultracold physics and chemistry [44], and with low-temperature calculations performed for other deep-well systems such as the previously-mentioned RbCs [39].

The ninth state problem was also an example of another possible use for the RmatReact methods: as a bound state finding method. As with the resonances, by using several different methods, a better understanding of their limits was obtained.

In Chapter 6, the theory was developed to facilitate Hund's case conversions at the boundary between the inner and outer regions, and to parity-adapt results obtained from inner-region codes. This is important in its own right, but can also serve as a preliminary theoretical result on the path to a developed theory for changing scattering coordinates at the boundary. Preliminary results were also obtained for the intramultiplet mixing of oxygen due to collisions with helium. These results show that the methods produced in this work are applicable to multichannel systems, which greatly increases the potential applicability of the diatomic RmatReact code and method.

7.2 Future Work

The physical problems that the RmatReact method is being designed to simulate are in some cases close to the cutting edge of experimental physics. As discussed in Chapter 5, the argon-argon simulations were perfomed with a specific recent experimental result in mind [180].

Also as discussed in that chapter, there are still a large number of unanswered questions concerning that physical system. It is hoped that experimental physicists may be inspired by the theoretical work being done here to perform experiments on some of these systems. In particular, it would be insightful to see what experimental measurements of the argon-argon collision's scattering length would yield. Novel experimental techniques such as those by Beyer & Merkt [200] may help to resolve the dispute over the Ar_2 scattering length and the alleged ninth bound state.

On the computational side, the S-matrix pole results presented here were only preliminary explorations of the possibilities of that method. Seeing what could be yielded by further exploration of S-matrix pole methodology for the Ar_2 system would be a worthwhile endeavour. For instance, the convergence of the S-matrix pole positions was not considered in this work. In future work, it may be worthwhile to test how the position of the pole varies when the numerical parameters are varied. reskit also struggled to pinpoint the locations of low-energy poles along the imaginary axis that could correspond to bound and virtual states. Further explorations of the application of reskit to these ultracold systems may prove worthwhile.

With respect to the multichannel scattering methods derived in this work, one important extension will be to include the possibility of performing the calculations in space-fixed coordinates, and introducing the ability to transform between the two coordinates. This will be important for comparing the oxygen-helium scattering results with literature sources.

Interestingly, the oxygen-helium scattering problem also lends itself to a comparable atom-diatom extension. One of the reasons that oxygen-helium scattering was studied by some authors [198] was due to its similarity to the scattering of oxygen off of H_2. Unlike atomic hydrogen, both helium and molecular hydrogen are spin-zero, and they have similar electronic structure. This makes them fairly comparable, and also simplifies the problem of studying their scattering properties, as there are no hyperfine effects. A study of O-H_2 scattering may serve as a good test case of the atom-diatom version of RmatReact to compare against the atom-atom results of O-He scattering.

The RmatReact method itself is only just beginning with this work. With respect to the atom-atom scattering studied here, there are a number of additions that could be made to the methods developed here to accommodate more systems.

For instance, it is hoped that the RmatReact method may be used as a general bound state finder in the future. If it is ever used for this, then the problem of capturing the bound states, as discussed in Section 3.3.6 will be particularly pressing. How it interacts with the other bound state finding method, the S-matrix poles, is a potential avenue for future exploration of the method. Other successful bound state finding methods, such as Hutson's BOUND software which uses a coupled channel approach [201, 202] already exist in competition to this. Furthermore, diffuse bound states whose wavefunctions extend significantly beyond a_0 can be found rather efficiently within an R-matrix formalism by performing scattering calculations with negative energies [203, 204].

The choice of oxygen-helium scattering for the test case for multichannel scattering in this work was done to simplify the problem by making this same assumption: helium was assumed to have no internal structure, effectively. Future work on RmatReact may include PFARM being more extensively modified to accommodate collisions between a generic pair of atoms (and eventually generic pairs of molecules) which both have internal structure, which can be scattered off each other, and which can both enter and leave the interaction with arbitrary quantum numbers. This would also involve more theoretical work to adapt the relevant R-matrix theory presented here and in other sources to accommodate both reactants having structure – an issue that does not arise at all in electron-molecule interactions.

It could also be useful to modify the methods to account for collisions involving charged reactants and Coulomb potentials (notably one of the few pieces of classical physics that will be considered in this methodology). If both reactants are charged then asymptotic boundary conditions involving r^{-1} terms must be used, which can cause complications in the theory as many derivations assume that the highest power of r involved in the potentials is greater than -1.

Collisions involving external magnetic fields would also be a useful extension to the method, especially considering the connections between magnetic fields and Feshbach resonances discussed in Chapter 1. Adding this functionality would ideally involve modifying the theory and methods to work in the aforementioned space-fixed coordinates to simplify the matrix elements, and to allow for the total angular momentum to not be conserved, as an external, non-isotropic source of angular momentum would now be present.

Modifications to accommodate space-fixed coordinates could involve adding an option to PFARM to choose the frame one wishes to perform the calculations in. It would involve different sets of quantum numbers being considered, especially if external magnetic fields are also used, as these would require the magnetic quantum number M to be explicitly included and considered, as discussed in Section 6.2.

Another useful extension would be to include photoassociation reactions, which can also interact with Feshbach resonances [38]. These were discussed in Chapter 2 in relation to their relevance to propagator techniques. As mentioned in that chapter, simulating photoassociation reactions with propagator methods requires the wavefunction itself to be propagated. The theory required to extend the

Light-Walker and BBM R-matrix propagators to include wavefunction propagation does exist [30]. Like with R-matrix propagation, the theory of wavefunction propagation which has been developed for electron-atom and electron-molecule collisions would need to be adapted to the atom-atom case. As discussed in Section 2.2.2, this could then be compared to the well-established Numerov propagation technique [129].

Hyperfine effects were only briefly mentioned in this work, despite the fact that they are an important part of ultracold physics [59]. This is because nuclear hyperfine splitting of energy levels, whilst usually a small effect, is actually a significant effect when compared to ultracold energy scales. Hyperfine structures can be resolved far more clearly in ultracold systems [1]. In this work, systems that had no hyperfine splitting of energy levels were chosen. It would, of course, be advantageous for future work to examine systems where hyperfine splittings are present, and to optimise the effectiveness of the RmatReact methods for such systems.

As discussed in Section 3.1.3, several different quadrature schemes were considered for the inner region, for the purpose of finding a quadrature that had a more efficient distribution of points for integrating over a diatomic potential energy curve. Although no improvement was found to the Lobatto quadrature that fulfilled all of the requirements of the method, it is still hoped that a more efficient quadrature scheme, such as the Radau quadrature discussed in Section 3.1.4, will eventually be found if work on this problem persists.

Such a method would need to have an efficient numerical scheme for generating the grid points and weights, it would need to have at least one boundary point explicitly included in the quadrature, and it would need to be more efficiently distributed such that it had more points where the potential energy curve was steepest.

Although DUO and PFARM were used extensively in this work, they are not the only codes available that perform the tasks they were built for. The diatomic code LEVEL, which has similar but less general functionality to DUO, was also tested at various points, and other R-matrix propagation codes exist and can be modified for heavy-particle scattering, such as the ones used in UKRmol [67, 205].

Modifying LEVEL and UKRmol, and creating a new harness to interface between them, could be a worthwhile avenue of exploration for future work on atom-atom scattering.

Similarly, different outer region and asymptotic region methods were tested in this work that were not ultimately used in the 'final' version of RmatReact. These methods include different propagators and different asymptotic expansions. The Light-Walker propagator, for instance, was used to generate some of the results presented here as part of the development of the code, but was ultimately replaced with the BBM propagator implemented in PFARM. It is still possible that the Light-Walker propagator could be of use, even if only for comparison purposes, in future iterations of the RmatReact method. By contrast, the Burke-Schey asymptotic expansion – which was never properly implemented, and was ultimately replaced with the Gailitis expansion used in PFARM – would not be suitable for use in future versions of RmatReact. This is because it is already known that the Gailitis expansion is an improvement on it for the methods being considered here [94]. Instead, other propagators and asymptotic expansions that were not considered in this work could be included in future versions of RmatReact.

When closed channels *are* considered, they have exponentially decaying asymptotic boundary conditions (technically speaking closed channels are considered to have zero boundary conditions in this work), and an associated set of asymptotic expansions. The consequence is that the K-matrix must be replaced to account for these channels. Specifically, one must use a larger matrix that accounts for all open and closed channels, with the K-matrix as one sub-matrix, and another matrix being introduced to account for the closed channels. This affects the theory of the asymptotic region, and it affects the physics of the scattering observables by allowing the closed channels to influence the open ones somewhat. In order to be included in RmatReact, the established theory would then have to be adapted to the atom-atom case in order to be used.

This project was intended to lay the numerical groundwork for the application of RmatReact to more complicated physical systems. The atom-atom problem is simple because it only involves one reaction coordinate. A higher dimensional scattering problem is atom-diatom scattering.

This has three spatial dimensions, but also has an additional complication in addition to the reactants having more internal structure: it is the simplest system where chemical *reactions* can occur. As Equation 1.1 describes, the diatom BC can collide with the atom A to form the diatom AB, leaving the atom C. The additional complication is that now the coordinates before and after the collision are different.

Previous codes which perform heavy-particle scattering, such as Hutson's MOLSCAT [59], do not allow for reactions to occur, meaning that implementing reactions into atom-diatom scattering codes represents truly novel work. One collaborator, Dr. Eryn Spinlove, is currently researching this problem, expanding on work done by Dr. Laura McKemmish [31]. The triatomic code DVR3D [89] is being modified in a similar manner to the way DUO was modified in this work, with the intention of adding Lobatto functionality, and the ability to transform coordinates at the boundary.

Some examples of reactions that could be studied by future atom-diatom RmatReact methods are being explored by Dr. Spinlove and by Dr. Brianna Heazlewood: ultracold collisions between neutral species and ions, such as N_2^+ colliding with H, and both C^+ colliding with H_2 and CH^+ colliding with H [206]. It is hoped that the groundwork laid in this work will prove useful in the study of these systems.

The efficiency problems encountered in this work will be much more pressing in the multidimensional case. For instance, whilst the DVR methods discussed in Section 3.1.1 may offer some slight improvements in one-dimensional problems such as the one in this work, in multidimensional problems they potentially offer significant advantages to calculations [151].

As with much of the research conducted in this work, the use of DVRs was intended to lay the groundwork for efficiency improvements in future work in higher-dimensional systems. Another example was this was the brief study of variable step size propagators, as discussed in Section 3.2.3.1. It is still anticipated that in a multidimensional problem, where one must be more conservative with the number of iterations one uses in the propagation, the variable step size may introduce considerable efficiency boosts for a given accuracy, and so this side project may be revived at some stage.

A further example of efficiency improvements studied here that were not found to affect the one-dimensional problem, but may have a significant impact on the multidimensional problem, is the issue of removing states from the R-matrix sum [165]. In this work, only a few tests were performed on multichannel R-matrices with states removed from the sum, and they found non-trivial differences when states were removed. Removing states could be especially useful in multidimensional problems, however, and so would merit more experimentation.

If a precise relationship between the number of states excluded from the sum and the loss of accuracy as a result is known, then it may be possible to vary the number of states excluded on a channel-by-channel basis, and on a coordinate-by-coordinate basis. This would allow one to focus computational resources on the coordinates and channels where the most terms in the sum are needed for accuracy, at the expense of the less important ones.

On the other hand, the solution to the issues discussed in Section 3.3.1 required the addition of a function that slightly *decreased* the efficiency of the method; this was not a problem for the one-dimensional problem, but can be significant in the multidimensional case. Here, Dr. Spinlove has been working on resolving this issue in a way that does not decrease the efficiency as much.

One efficiency improvement that was not studied here was the Buttle correction. However, numerical issues such as the inability to delete terms from the R-matrix suggest that eventually it may be advantageous to add a Buttle-like correction to the RmatReact method. Further work on RmatReact will also include more sophisticated study of the nature of the boundary condition problems that the Buttle correction is often used to address. These boundary conditions are not especially well understood, but they will be important to understand to apply RmatReact to reactive collisions.

The ultimate goal of the next stage of the project is to be able to produce scattering observables such as the cross-section for atom-diatom reactions. But even in the non-reactive case, there is interesting physics that can be probed that is not present in the atom-atom case. Two examples include Feshbach resonances, which can be formed in many more ways in the atom-diatom case, and Efimov trimers, which do not exist at all in the atom-atom case.

After the method has been shown to work in multidimensional, reactive cases, it it possible that the RmatReact method could eventually be extended to obtain scattering observables for generic polyatom-polyatom collisions. The ExoMol project generates high-resolution molecular spectra [207] for different sized molecular systems using different codes: DUO [86] and LEVEL [88] are used for two-atom problems (such as the spectrum of sodium hydride [208]), DVR3D [89] is used for three-atom problems, and WAVR4 [90] and TROVE [91, 92] are used for larger systems. In analogy with the evolution of the ExoMol project, the adaptation of DUO to the scattering problems presented here could lead to these other codes also being adapted for scattering problems involving larger systems.

The possibility of studying chemical reactions at the state-to-state level is one of the most exciting implications of the RmatReact method: it can be considered the very foundation of chemistry itself. To the extent that a border between physics and chemistry exists, this is truly right on that edge.

Being able to control chemical reactions at this level in ultracold conditions is a tantalising prospect for future research in theoretical, computational, and experimental physics. The atom-diatom collisions are only the beginning. As the method is developed, it may become possible to simulate arbitrary polyatom-polyatom collisions at the same, fine-grained, state-to-state level of control presented here.

This thesis proved it was possible to combine the field of high-precision molecular spectroscopy with the field of electron-heavy particle collisions to produce a novel method that incorporates the strengths of each. Hopefully, future work will build on the successes presented here, learn from the failures, and change the way that the hazy borders between physics and chemistry are explored.

Bibliography

[1] Benjamin K. Stuhl, Matthew T. Hummon, and Jun Ye. Cold State-Selected Molecular Collisions and Reactions. *Ann. Rev. Phys. Chem.*, 65:501–518, 2014.

[2] Edward S Shuman, John F Barry, and David DeMille. Laser cooling of a diatomic molecule. *Nature*, 467:820–823, 2010.

[3] Valentina Zhelyazkova, Anne Cournol, Thomas E Wall, Aki Matsushima, Jonathan J Hudson, E A Hinds, M R Tarbutt, and B E Sauer. Laser cooling and slowing of CaF molecules. *Phys. Rev. A*, 89:053416, 2014.

[4] J D Weinstein, R deCarvalho, T Guillet, B Friedrich, and J M Doyle. Magnetic trapping of calcium monohydride molecules at millikelvin temperatures. *Nature*, 395:148–150, 1998.

[5] Vijay Singh, Kyle S. Hardman, Naima Tariq, Mei-Ju Lu, Aja Ellis, Muir J. Morrison, and Jonathan D. Weinstein. Chemical Reactions of Atomic Lithium and Molecular Calcium Monohydride at 1 K. *Phys. Rev. Lett.*, 108:203201, 2012.

[6] Michał Tomza, Krzysztof Jachymski, Rene Gerritsma, Antonio Negretti, Tommaso Calarco, Zbigniew Idziaszek, and Paul S Julienne. Cold hybrid ion-atom systems. *Reviews of Modern Physics*, 91(3):035001, 2019.

[7] Vladan Vuletić and Steven Chu. Laser cooling of atoms, ions, or molecules by coherent scattering. *Phys. Rev. Lett.*, 84:3787, 2000.

[8] R Horchani. Laser cooling of internal degrees of freedom of molecules. *Frontiers of Physics*, 11:113301, 2016.

[9] A Aspect, J Dalibard, A Heidmann, C Salomon, and C Cohen-Tannoudji. Cooling atoms with stimulated emission. *Phys. Rev. Lett.*, 57:1688, 1986.

[10] William D Phillips and Harold J Metcalf. Cooling and trapping atoms. *Scientific American*, 256:50–57, 1987.

[11] Jean Dalibard and Claude Cohen-Tannoudji. Laser cooling below the Doppler limit by polarization gradients: simple theoretical models. *JOSA B*, 6(11):2023–2045, 1989.

[12] M Anderlini, E Courtade, M Cristiani, D Cossart, D Ciampini, Carlo Sias, O Morsch, and E Arimondo. Sympathetic cooling and collisional properties of a Rb-Cs mixture. *Physical Review A*, 71(6):061401, 2005.

[13] P.F. Barker, S. M. Purcell, P. Douglas, P. Barletta, N. Coppendale, C. Maher-McWilliams, and J. Tennyson. Sympathetic cooling by collisions with ultra cold rare gas atoms and recent progress in optical Stark deceleration. *Faraday Discuss.*, 142:175–190, 2009.

[14] P. Barletta, J. Tennyson, and P. F. Barker. Towards sympathetic cooling of large molecules: Cold collisions between benzene and rare gas atoms. *New J. Phys*, 11:055029, 2009.

[15] P. Barletta, J. Tennyson, and P. F. Barker. Direct Monte Carlo Simulation of the sympathetic cooling of trapped molecules. *New J. Phys*, 12:113002, 2010.

[16] Benjamin K. Stuhl, Matthew T. Hummon, Mark Yeo, Goulven Quemener, John L. Bohn, and Jun Ye. Evaporative cooling of the dipolar hydroxyl radical. *Nature*, 492:396–400, 2012.

[17] Peter K. Molony, Philip D. Gregory, Zhonghua Ji, Bo Lu, Michael P. Köppinger, C. Ruth Le Sueur, Caroline L. Blackley, Jeremy M. Hutson, and

Simon L. Cornish. Creation of Ultracold ^{87}Rb^{133}Cs Molecules in the Rovibrational Ground State. *Phys. Rev. Lett.*, 113:255301, 2014.

[18] Anna Dawid, Maciej Lewenstein, and Michał Tomza. Two interacting ultracold molecules in a one-dimensional harmonic trap. *Phys. Rev. A*, 97:063618, 2018.

[19] John L Bohn. Inelastic collisions of ultracold polar molecules. *Phys. Rev. A*, 63:052714, 2001.

[20] Thorsten Köhler, Krzysztof Góral, and Paul S Julienne. Production of cold molecules via magnetically tunable Feshbach resonances. *Rev. Mod. Phys.*, 78:1311, 2006.

[21] Brianna R. Heazlewood and Timothy P. Softley. Low-Temperature Kinetics and Dynamics with Coulomb Crystals. *Ann. Rev. Phys. Chem.*, 66:475–495, 2015.

[22] Martin T Bell and Timothy P Softley. Ultracold molecules and ultracold chemistry. *Mol. Phys.*, 107:99–132, 2009.

[23] Martin T. Bell, Alexander D. Gingell, James M. Oldham, Timothy P. Softley, and Stefan Willitsch. Ion-molecule chemistry at very low temperatures: cold chemical reactions between Coulomb-crystallized ions and velocity-selected neutral molecules. *Faraday Disc.*, 142:73–91, 2009.

[24] Goulven Quemener and Paul S Julienne. Ultracold molecules under control! *Chem. Rev.*, 112:4949–5011, 2012.

[25] S Ospelkaus, K-K Ni, D Wang, M H G De Miranda, B Neyenhuis, G Quéméner, P S Julienne, J L Bohn, D S Jin, and J Ye. Quantum-state controlled chemical reactions of ultracold potassium-rubidium molecules. *Science*, 327:853–857, 2010.

[26] Deborah S Jin and Jun Ye. Introduction to ultracold molecules: new frontiers in quantum and chemical physics. *Chem. Rev.*, 112:4801–4802, 2012.

[27] Benjamin Bertsche, Justin Jankunas, and Andreas Osterwalder. Low-temperature collisions between neutral molecules in merged molecular beams. *CHIMIA Intern. J. Chem.*, 68:256–259, 2014.

[28] Chengdong He, Elnur Hajiyev, Zejian Ren, Bo Song, and Gyu-Boong Jo. Recent progresses of ultracold two-electron atoms. *J. Phys. B: At. Mol. Opt. Phys.*, 52:102001, 2019.

[29] J. Tennyson. Electron - molecule collision calculations using the R-matrix method. *Phys. Rep.*, 491:29–76, 2010.

[30] Philip George Burke. *R-Matrix Theory of Atomic Collisions: Application to Atomic, Molecular and Optical Processes*, volume 61. Springer Science & Business Media, 2011.

[31] Laura K. McKemmish and J. Tennyson. General Mathematical Formulation of Scattering Processes in Atom-Diatomic Collisions in the RmatReact Methodology. *Phil. Trans. Royal Soc. London A*, 377:20180409, 2019.

[32] Cheng Chin, Rudolf Grimm, Paul Julienne, and Eite Tiesinga. Feshbach resonances in ultracold gases. *Rev. Mod. Phys.*, 82:1225, 2010.

[33] Jeremy M Hutson, Musie Beyene, and Maykel Leonardo González-Martínez. Dramatic reductions in inelastic cross sections for ultracold collisions near Feshbach resonances. *Phys. Rev. Lett.*, 103:163201, 2009.

[34] Michael Mayle, Goulven Quemener, Brandon P. Ruzic, and John L. Bohn. Scattering of ultracold molecules in the highly resonant regime. *Phys. Rev. A*, 87:012709, 2013.

[35] Gregory Breit and Eugene Wigner. Capture of slow neutrons. *Phys. Rev.*, 49:519, 1936.

[36] J. Tennyson and C. J. Noble. RESON: for the automatic detection and fitting of breit-wigner resonances. *Comput. Phys. Commun.*, 33:421–424, 1984.

[37] Ugo Fano. Effects of configuration interaction on intensities and phase shifts. *Phys. Rev.*, 124:1866, 1961.

[38] Philippe Pellegrini, Marko Gacesa, and Robin Côté. Giant formation rates of ultracold molecules via Feshbach-optimized photoassociation. *Phys. Rev. Lett.*, 101:053201, 2008.

[39] MJ Jamieson, H Sarbazi-Azad, H Ouerdane, GH Jeung, Yoon Sup Lee, and WC Lee. Elastic scattering of cold caesium and rubidium atoms. *Journal of Physics B: Atomic, Molecular and Optical Physics*, 36(6):1085, 2003.

[40] Alan Carrington, Juliet Buttenshaw, and Richard Kennedy. Observation of the infrared spectrum of H3+ at its dissociation limit. *Mol. Phys.*, 45:753–758, 1982.

[41] J. R. Henderson and J. Tennyson. Calculated spectrum for near-dissociation H_3^+: a first attempt. *Mol. Phys.*, 89:953–963, 1996.

[42] Faye Kemp, C Euan Kirk, and Iain R McNab. The infrared predissociation spectrum of H3+. *Phil. Trans. A*, 358:2403–2418, 2000.

[43] J. Tennyson, O. L. Polyansky, N. F. Zobov, A. Alijah, and A. G. Császár. High accuracy calculations of the rotation-vibration spectrum of H_3^+. *J. Phys. B: At. Mol. Opt. Phys.*, 50:232001, 2017.

[44] Edvardas Narevicius and Mark G Raizen. Toward cold chemistry with magnetically decelerated supersonic beams. *Chemical reviews*, 112(9):4879–4889, 2012.

[45] Krzysztof Jachymski. Impact of overlapping resonances on magnetoassociation of cold molecules in tight traps. *J. Phys. B: At. Mol. Opt. Phys.*, 49:195204, 2016.

[46] José P D'Incao, Hiroya Suno, and Brett D Esry. Limits on universality in ultracold three-boson recombination. *Phys. Rev. Lett.*, 93:123201, 2004.

[47] Thomas Lompe, Timo B Ottenstein, Friedhelm Serwane, Andre N Wenz, Gerhard Zürn, and Selim Jochim. Radio-frequency association of Efimov trimers. *Science*, 330:940–944, 2010.

[48] F Ferlaino, A Zenesini, M Berninger, B Huang, H-C Nägerl, and R Grimm. Efimov resonances in ultracold quantum gases. *Few-Body Systems*, 51:113–133, 2011.

[49] Yujun Wang and B D Esry. Efimov trimer formation via ultracold four-body recombination. *Phys. Rev. Lett.*, 102:133201, 2009.

[50] J P D'Incao and B D Esry. Enhancing the observability of the Efimov effect in ultracold atomic gas mixtures. *Phys. Rev. A*, 73:030703, 2006.

[51] T Kraemer, M Mark, P Waldburger, J G Danzl, C Chin, B Engeser, A D Lange, K Pilch, A Jaakkola, H-C Nägerl, et al. Evidence for Efimov quantum states in an ultracold gas of caesium atoms. *Nature*, 440:315–318, 2006.

[52] S Knoop, F Ferlaino, M Mark, M Berninger, H Schöbel, H-C Nägerl, and R Grimm. Observation of an Efimov-like resonance in ultracold atom-dimer scattering. *Nature Phys.*, 5:227–230, 2009.

[53] Javier von Stecher, Jose P D'Incao, and Chris H Greene. Signatures of universal four-body phenomena and their relation to the Efimov effect. *Nat. Phys.*, 5:417–421, 2009.

[54] Francesca Ferlaino and Rudolf Grimm. Trend: Forty years of Efimov physics: How a bizarre prediction turned into a hot topic. *Physics*, 3:9, 2010.

[55] M Berninger, A Zenesini, B Huang, W Harm, H-C Nägerl, F Ferlaino, R Grimm, P S Julienne, and J M Hutson. Universality of the three-body parameter for Efimov states in ultracold cesium. *Phys. Rev. Lett.*, 107:120401, 2011.

[56] Mike H Anderson, Jason R Ensher, Michael R Matthews, Carl E Wieman, and Eric A Cornell. Observation of Bose-Einstein condensation in a dilute atomic vapor. *Science*, pages 198–201, 1995.

[57] Immanuel Bloch, Jean Dalibard, and Sylvain Nascimbene. Quantum simulations with ultracold quantum gases. *Nat Phys*, 8:267–276, 2012.

[58] Stuart C. Althorpe and David C. Clary. Quantum scattering calculations on chemical reactions. *Ann. Rev. Phys. Chem.*, 54:493–529, 2003.

[59] Jeremy M Hutson and C Ruth Le Sueur. MOLSCAT: a program for non-reactive quantum scattering calculations on atomic and molecular collisions. *Computer Physics Communications*, 241:9–18, 2019.

[60] Russell T Pack and Gregory A. Parker. Quantum reactive scattering in three dimensions using hyperspherical (aph) coordinates. theory. *J. Chem. Phys.*, 87:3888–3921, 1987.

[61] P. Honvault, M. Jorfi, T. González-Lezana, A. Faure, and L. Pagani. *Ortho-Para* H_2 Conversion by Proton Exchange at Low Temperature: An Accurate Quantum Mechanical Study. *Phys. Rev. Lett.*, 107:023201, 2011.

[62] G B Pradhan, N Balakrishnan, and Brian K Kendrick. Quantum dynamics of $O(^1D)+D_2$ reaction: isotope and vibrational excitation effects. *J. Phys. B: At. Mol. Opt. Phys.*, 47:135202, 2014.

[63] Brian K Kendrick. Non-adiabatic quantum reactive scattering in hyperspherical coordinates. *J. Chem. Phys.*, 148:044116, 2018.

[64] J M Launay and M Le Dourneuf. Hyperspherical close-coupling calculation of integral cross-sections for the reaction $h+h_2 \rightarrow h_2+h$. *Chem. Phys. Lett.*, 163:178–188, 1989.

[65] John William Strutt and Baron Rayleigh. *The theory of sound*. Dover, 1945.

[66] H Faxén and J Holtsmark. Beitrag zur Theorie des Durchganges langsamer Elektronen durch Gase. *Zeitschrift für Physik*, 45:307–324, 1927.

[67] J. M. Carr, P. G. Galiatsatos, J. D. Gorfinkiel, A. G. Harvey, M. A. Lysaght, D. Madden, Z. Mašín, M. Plummer, and J. Tennyson. The ukrmol program suite. *Eur. Phys. J. D*, 66:58, 2012.

[68] PG Burke and J Tennyson. R-matrix theory of electron molecule scattering. *Molecular Physics*, 103:2537–2548, 2005.

[69] C. J. Bocchetta and J. Gerratt. The application of the Wigner Rmatrix theory to molecular collisions. *J. Chem. Phys.*, 82:1351–1362, 1985.

[70] James P. Burke, Chris H. Greene, and John L. Bohn. Multichannel Cold Collisions: Simple Dependences on Energy and Magnetic Field. *Phys. Rev. Lett.*, 81:3355–3358, 1998.

[71] M. Raoult and F. H. Mies. Feshbach resonance in atomic binary collisions in the Wigner threshold law regime. *Phys. Rev. A*, 70:012710, 2004.

[72] Bo Gao, Eite Tiesinga, Carl J. Williams, and Paul S. Julienne. Multichannel quantum-defect theory for slow atomic collisions. *Phys. Rev. A*, 72:042719, 2005.

[73] Bo Gao, Eite Tiesinga, Carl J Williams, and Paul S Julienne. Multichannel quantum-defect theory for slow atomic collisions. *Phys. Rev. A*, 72:042719, 2005.

[74] James F. E. Croft, Alisdair O. G. Wallis, Jeremy M. Hutson, and Paul S. Julienne. Multichannel quantum defect theory for cold molecular collisions. *Phys. Rev. A*, 84:042703, 2011.

[75] James F. E. Croft, Jeremy M. Hutson, and Paul S. Julienne. Optimized multichannel quantum defect theory for cold molecular collisions. *Phys. Rev. A*, 86:022711, 2012.

[76] James FE Croft, Alisdair OG Wallis, Jeremy M Hutson, and Paul S Julienne. Multichannel quantum defect theory for cold molecular collisions. *Phys. Rev. A*, 84:042703, 2011.

[77] Eugene P Wigner. Resonance reactions and anomalous scattering. *Phys. Rev.*, 70:15, 1946.

[78] Eugene Paul Wigner and Leonard Eisenbud. Higher angular momenta and long range interaction in resonance reactions. *Phys. Rev.*, 72:29, 1947.

[79] Pierre Descouvemont and D Baye. The R-matrix theory. *Rep. Prog. Phys.*, 73:036301, 2010.

[80] Max Born and Robert Oppenheimer. Zur quantentheorie der molekeln. *Annalen der Physik*, 389:457–484, 1927.

[81] F H Mies. A scattering theory of diatomic molecules: General formalism using the channel state representation. *Mol. Phys.*, 41:953–972, 1980.

[82] H. Y. Mussa and J. Tennyson. Calculation of rotation-vibration states of water at dissociation. *J. Chem. Phys.*, 109:10885–10892, 1998.

[83] A. G. Császár, E. Mátyus, T Szidarovszky, L. Lodi, N. F. Zobov, S. V. Shirin, O. L. Polyansky, and J. Tennyson. Ab initio prediction and partial characterization of the vibrational states of water up to dissociation. *J. Quant. Spectrosc. Radiat. Transf.*, 111:1043–1064, 2010.

[84] N. F. Zobov, S. V. Shirin, L. Lodi, B. C. Silva, J. Tennyson, A. G. Császár, and O. L. Polyansky. First-principles rotation-vibration spectrum of water above dissociation. *Chem. Phys. Lett.*, 507:48–51, 2011.

[85] Tamás Szidarovszky and Attila G Császár. Low-lying quasibound rovibrational states of H2 16O. *Mol. Phys.*, 111:2131–2146, 2013.

[86] S. N. Yurchenko, L. Lodi, J. Tennyson, and A. V. Stolyarov. Duo: a general program for calculating spectra of diatomic molecules. *Comput. Phys. Commun.*, 202:262–275, 2016.

[87] Jonathan Tennyson, Lorenzo Lodi, Laura K McKemmish, and Sergei N Yurchenko. The ab initio calculation of spectra of open shell diatomic molecules. *J. Phys. B: At. Mol. Opt. Phys.*, 49:102001, 2016.

[88] Robert J Le Roy. LEVEL: A computer program for solving the radial Schrödinger equation for bound and quasibound levels. *J. Quant. Spectrosc. Radiat. Transf.*, 186:167–178, 2017.

[89] J. Tennyson, M. A. Kostin, P. Barletta, G. J. Harris, O. L. Polyansky, J. Ramanlal, and N. F. Zobov. DVR3D: a program suite for the calculation of rotation-vibration spectra of triatomic molecules. *Comput. Phys. Commun.*, 163:85–116, 2004.

[90] I. N. Kozin, M. M. Law, J. Tennyson, and J. M. Hutson. New vibration-rotation code for tetraatomic molecules WAVR4. *Comput. Phys. Commun.*, 163:117–131, 2004.

[91] Sergei N Yurchenko, Walter Thiel, and Per Jensen. Theoretical ROVibrational Energies (TROVE): A robust numerical approach to the calculation of rovibrational energies for polyatomic molecules. *J. Mol. Spectrosc.*, 245:126–140, 2007.

[92] Andrey Yachmenev and Sergei N Yurchenko. Automatic differentiation method for numerical construction of the rotational-vibrational Hamiltonian as a power series in the curvilinear internal coordinates using the Eckart frame. *J. Chem. Phys.*, 143:014105, 2015.

[93] Robert B Walker and John C Light. Reactive molecular collisions. *Ann. Rev. Phys. Chem.*, 31:401–433, 1980.

[94] A G Sunderland, C J Noble, V M Burke, and P G Burke. A parallel R-matrix program PRMAT for electron–atom and electron–ion scattering calculations. *Comput. Phys. Commun.*, 145:311–340, 2002.

[95] V M Burke and C J Noble. FarmA flexible asymptotic R-matrix package. *Comput. Phys. Commun.*, 85:471–500, 1995.

[96] John C Light and Robert B Walker. An R matrix approach to the solution of coupled equations for atom–molecule reactive scattering. *J. Chem. Phys.*, 65:4272–4282, 1976.

[97] Hong Zhang, Sean C Smith, Shinkoh Nanbu, and Hiroki Nakamura. Quantum mechanical study of atomic hydrogen interaction with a fluorinated boron-substituted coronene radical. *J. Phys.: Condensed Matter*, 21:144209, 2009.

[98] Pavel Soldán, Marko T Cvitaš, Jeremy M Hutson, Pascal Honvault, and Jean-Michel Launay. Quantum Dynamics of Ultracold Na+ Na_2 Collisions. *Phys. Rev. Lett.*, 89:153201, 2002.

[99] Alisdair O G Wallis and Jeremy M Hutson. Production of ultracold NH molecules by sympathetic cooling with Mg. *Phys. Rev. Lett.*, 103:183201, 2009.

[100] Daniel A Brue and Jeremy M Hutson. Magnetically tunable Feshbach resonances in ultracold Li-Yb mixtures. *Phys. Rev. Lett.*, 108:043201, 2012.

[101] Chris H Greene, A R P Rau, and U Fano. General form of the quantum-defect theory. II. *Phys. Rev. A*, 26:2441, 1982.

[102] C Greene, U Fano, and G Strinati. General form of the quantum-defect theory. *Phys. Rev. A*, 19:1485, 1979.

[103] M J Seaton. Quantum defect theory. *Rep. Prog. Phys.*, 46:167, 1983.

[104] Tom Rivlin, Laura K. McKemmish, and Jonathan Tennyson. Low-Temperature Scattering with the R-Matrix Method: The Morse Potential. In P. C. Deshmukh, E. Krishnakumar, Stephan Fritzsche, M. Krishnamurthy, and Sonjoy Majumder, editors, *Quantum Collisions and Confinement of*

Atomic and Molecular Species, and Photons, volume 230, pages 257–273, Singapore, 2019. Springer Singapore.

[105] T. Rivlin, L. K. McKemmish, K. E. Spinlove, and J. Tennyson. Low temperature scattering with the R-matrix method: argon-argon scattering. *Mol. Phys.*, 117(21):3158–3170, 2019.

[106] Philip M Morse. Diatomic molecules according to the wave mechanics. II. Vibrational levels. *Phys. Rev.*, 34:57, 1929.

[107] J. Tennyson. The calculation of vibration-rotation energies of triatomic molecules using scattering coordinates. *Comput. Phys. Rep.*, 4:1–36, 1986.

[108] Roman V Krems and Alexei A Buchachenko. Quantum and semiclassical study of the intramultiplet transitions in collisions of Cl (2P) and O (3P) with He, Ar and Xe. *Journal of Physics B: Atomic, Molecular and Optical Physics*, 33(21):4551, 2000.

[109] Milton Abramowitz and Irene A Stegun. *Handbook of mathematical functions: with formulas, graphs, and mathematical tables*, volume 55. Courier Corporation, 1964.

[110] Mark Sheard Child. *Molecular collision theory*. Courier Corporation, 1996.

[111] Roger G Newton. *Scattering theory of waves and particles*. Springer Science & Business Media, 2013.

[112] H A Bethe. Theory of the effective range in nuclear scattering. *Phys. Rev.*, 76:38, 1949.

[113] John M Blatt and J David Jackson. On the interpretation of neutron-proton scattering data by the Schwinger variational method. *Phys. Rev.*, 76:18, 1949.

[114] A M Arthurs and A Dalgarno. The theory of scattering by a rigid rotator. *Proc. Phys. Soc. London A*, 256:540–551, 1960.

[115] Roman V Krems. Cold controlled chemistry. *Phys. Chem. Chem. Phys.*, 10:4079–4092, 2008.

[116] H M Nussenzveig. The poles of the S-matrix of a rectangular potential well of barrier. *Nucl. Phys.*, 11:499–521, 1959.

[117] John R Taylor. *Scattering theory: the quantum theory of nonrelativistic collisions*. Courier Corporation, 2006.

[118] M Cízek and J Horácek. On shooting methods for calculation of potential resonances. *J. Phys. A: Math. Gen.*, 29:6325, 1996.

[119] P. G. Burke and J. Tennyson. R-matrix theory of electron molecule scattering. *Mol. Phys.*, 103:2537–2548, 2005.

[120] K Patkowski, G Murdachaew, C M Fou, and K Szalewicz. Accurate ab initio potential for argon dimer including highly repulsive region. *Mol. Phys.*, 103:2031–2045, 2005.

[121] Ronald A Aziz. A highly accurate interatomic potential for argon. *J. Chem. Phys.*, 99:4518–4525, 1993.

[122] Petr Slavíček, René Kalus, Petr Paška, Iva Odvárková, Pavel Hobza, and Anatol Malijevskẏ. State-of-the-art correlated ab initio potential energy curves for heavy rare gas dimers: Ar_2, Kr_2, and Xe_2. *J. Chem. Phys.*, 119:2102–2119, 2003.

[123] K T Tang and J P Toennies. The van der Waals potentials between all the rare gas atoms from He to Rn. *J. Chem. Phys.*, 118:4976–4983, 2003.

[124] Vincenzo Aquilanti, Roberto Candori, and Fernando Pirani. Molecular beam studies of weak interactions for open-shell systems: The ground and lowest excited states of rare gas oxides. *The Journal of chemical physics*, 89(10):6157–6164, 1988.

[125] B A Robson. The Bloch L-operator. *Nucl. Phys. A*, 132:5–8, 1969.

[126] Winifred M. Huo and David Brown. Finite-element Z-matrix method: Application to electron-molecule collisions. *Phys. Rev. A*, 60:295–305, 1999.

[127] Eric W. Weisstein. Green's Function From MathWorld—A Wolfram Web Resource. Last visited on 17/04/19.

[128] P J A Buttle. Solution of coupled equations by R-matrix techniques. *Phys. Rev.*, 160:719, 1967.

[129] B. V. Noumerov. A method of extrapolation of perturbations. *MNRAS*, 84:592–602, 1924.

[130] Jan Franz, Magnus Gustafsson, and Gunnar Nyman. Formation of carbon monoxide by radiative association: a quantum dynamical study. *MNRAS*, 414:3547–3550, 2011.

[131] K L Baluja, P G Burke, and L A Morgan. R-matrix propagation program for solving coupled second-order differential equations. *Comput. Phys. Commun.*, 27:299–307, 1982.

[132] Ellen B Stechel, Robert B Walker, and John C Light. R-matrix solution of coupled equations for inelastic scattering. *J. Chem. Phys.*, 69:3518–3531, 1978.

[133] Barry I Schneider and Robert B Walker. The coupled channel R-matrix propagation method. *J. Chem. Phys.*, 70:2466–2470, 1979.

[134] Philip G Burke and Harry M Schey. Elastic scattering of low-energy electrons by atomic hydrogen. *Phys. Rev.*, 126:147, 1962.

[135] M Gailitis. New forms of asymptotic expansions for wavefunctions of charged-particle scattering. *J. Phys.B: At. Mol. Phys.*, 9:843, 1976.

[136] Philip T Myatt, Ashok K Dham, Pragna Chandrasekhar, Frederick R W McCourt, and Robert J Le Roy. A new empirical potential energy function for Ar_2. *Mol. Phys.*, 116:1–26, 2018.

[137] Roman V Krems and Alexei A Buchachenko. Ultracold inelastic atomic collisions: Threshold relaxation of O (3 P 0) by He. *Physical Review A*, 64(2):024704, 2001.

[138] Robert J Le Roy and Robert DE Henderson. A new potential function form incorporating extended long-range behaviour: application to ground-state Ca2. *Molecular Physics*, 105(5-7):663–677, 2007.

[139] G Rawitscher, Cory Merow, Matthew Nguyen, and Ionel Simbotin. Resonances and quantum scattering for the Morse potential as a barrier. *Am. J. Phys.*, 70:935–944, 2002.

[140] Eric W. Weisstein. Confluent Hypergeometric Function of the First Kind From MathWorld—A Wolfram Web Resource. Last visited on 19/01/18.

[141] Matti Selg. Complete solution of the Marchenko equation for a simple model system. *Proc. Estonian Acad. Sci.*, 65:267–283, 2016.

[142] Matti Selg. Observable quasi-bound states of the H2 molecule. *J. Chem. Phys.*, 136:114113, 2012.

[143] Peter S Bingham and Jimena D Gorfinkiel. reskit: A toolkit to determine the poles of an S-matrix. *Computer Physics Communications*, 2019.

[144] Arthur H Stroud and Don Secrest. *Gaussian quadrature formulas*. Prentice-Hall, 1966.

[145] William H Press, Saul A Teukolsky, William T Vetterling, and Brian P Flannery. *Numerical recipes in C*, volume 2. Cambridge University Press Cambridge, 1996.

[146] CA Micchelli and T. J. Rivlin. Numerical integration rules near Gaussian quadrature. *Israel J. Math.*, 16:287–299, 1973.

[147] CA Micchelli and T. J. Rivlin. Turán formulae and highest precision quadrature rules for Chebyshev coefficients. *IBM J. Res. Dev/*, 16:372–379, 1972.

[148] D E Manolopoulos. Lobatto Shape Functions. In *Numerical Grid Methods and Their Application to Schrödingers Equation*, pages 57–68. Springer, 1993.

[149] David O Harris, Gail G Engerholm, and William D Gwinn. Calculation of Matrix Elements for One-Dimensional Quantum-Mechanical Problems and the Application to Anharmonic Oscillators. *The Journal of Chemical Physics*, 43(5):1515–1517, 1965.

[150] AS Dickinson and PR Certain. Calculation of Matrix Elements for One-Dimensional Quantum-Mechanical Problems. *The Journal of Chemical Physics*, 49(9):4209–4211, 1968.

[151] John C Light and Tucker Carrington Jr. Discrete-variable representations and their utilization. *Adv. Chem. Phys.*, 114:263–310, 2000.

[152] Vladimir Ivanovich Krylov and Arthur H Stroud. *Approximate calculation of integrals*. Courier Corporation, 2006.

[153] J C Light, I P Hamilton, and J V Lill. Generalized discrete variable approximation in quantum mechanics. *J. Chem. Phys.*, 82:1400–1409, 1985.

[154] Hua Wei and Tucker Carrington Jr. The discrete variable representation of a triatomic Hamiltonian in bond length–bond angle coordinates. *The Journal of chemical physics*, 97(5):3029–3037, 1992.

[155] Bill Poirier and JC Light. Phase space optimization of quantum representations: Direct-product basis sets. *The Journal of chemical physics*, 111(11):4869–4885, 1999.

[156] Bill Poirier and JC Light. Phase space optimization of quantum representations: Three-body systems and the bound states of HCO. *The Journal of Chemical Physics*, 114(15):6562–6571, 2001.

[157] Daniel T Colbert and William H Miller. A novel discrete variable representation for quantum mechanical reactive scattering via the S-matrix Kohn method. *J. Chem. Phys.*, 96:1982–1991, 1992.

[158] Eric W. Weisstein. Lobatto Quadrature From MathWorld—A Wolfram Web Resource. Last visited on 22/11/16.

[159] Eric W. Weisstein. Radau Quadrature From MathWorld—A Wolfram Web Resource. Last visited on 13/09/17.

[160] D E Manolopoulos and R E Wyatt. Quantum scattering via the log derivative version of the kohn variational principle. *Chem. Phys. Lett.*, 152:23–32, 1988.

[161] Edward Anderson, Zhaojun Bai, Christian Bischof, Susan Blackford, Jack Dongarra, Jeremy Du Croz, Anne Greenbaum, Sven Hammarling, A McKenney, and D Sorensen. *LAPACK Users' guide*, volume 9. Siam, 1999.

[162] A Hibbert. CIV3A general program to calculate configuration interaction wave functions and electric-dipole oscillator strengths. *Computer Physics Communications*, 9(3):141–172, 1975.

[163] W Eissner, M Jones, and H Nussbaumer. Techniques for the calculation of atomic structures and radiative data including relativistic corrections. *Computer Physics Communications*, 8(4):270–306, 1974.

[164] S A Rakityansky, S A Sofianos, and N Elander. Pade approximation of the S-matrix as a way of locating quantum resonances and bound states. *J. Phys. A: Math. Gen.*, 40:14857, 2007.

[165] J. Tennyson. Partitioned R-matrix theory for molecules. *J. Phys. B: At. Mol. Opt. Phys.*, 37:1061–1071, 2004.

[166] Zdeněk Mašín. Private communications. 2017.

[167] J. Tennyson, L. K. McKemmish, and T. Rivlin. Low temperature chemistry using the R-matrix method. *Faraday Discuss.*, 195:31–48, 2016.

[168] Beresford N Parlett. *The symmetric eigenvalue problem*, volume 20. siam, 1998.

[169] Per-Olov Löwdin. On the non-orthogonality problem connected with the use of atomic wave functions in the theory of molecules and crystals. *The Journal of Chemical Physics*, 18(3):365–375, 1950.

[170] Luc Lathouwers. A new approach to canonical orthonormalisation. *Intern. J. Quantum Chem.*, 10:413–418, 1976.

[171] Annavarapu Ramesh Naidu. Centrality of Lowdin orthogonalizations. *arXiv preprint arXiv:1105.3571*, 2011.

[172] Eric W. Weisstein. Gram-Schmidt Orthonormalization From MathWorld—A Wolfram Web Resource. Last visited on 03/08/19.

[173] Paul S Julienne. Ultracold molecules from ultracold atoms: a case study with the KRb molecule. *Faraday discussions*, 142:361–388, 2009.

[174] Matthew D Frye, Paul S Julienne, and Jeremy M Hutson. Cold atomic and molecular collisions: approaching the universal loss regime. *New J. Phys*, 17:045019, 2015.

[175] Peter J Mohr, Barry N Taylor, and David B Newell. CODATA recommended values of the fundamental physical constants: 2010. *Journal of Physical and Chemical Reference Data*, 84(4):1527, 2012.

[176] Wen-Chao Qiang and Shi-Hai Dong. Arbitrary l-state solutions of the rotating Morse potential through the exact quantization rule method. *Phys. Lett. A*, 363:169–176, 2007.

[177] Konrad Patkowski and Krzysztof Szalewicz. Argon pair potential at basis set and excitation limits. *J. Chem. Phys.*, 133:094304, 2010.

[178] R A Aziz and H H Chen. An accurate intermolecular potential for argon. *J. Chem. Phys.*, 67:5719–5726, 1977.

[179] Bo Song, Xiaopo Wang, Jiangtao Wu, and Zhigang Liu. Prediction of transport properties of pure noble gases and some of their binary mixtures by ab initio calculations. *Fluid Phase Equilibria*, 290:55–62, 2010.

[180] P. D. Edmunds and P. F. Barker. Trapping Cold Ground State Argon Atoms. *Phys. Rev. Lett.*, 113:183001, 2014.

[181] Taghi Sahraeian and M R Hadizadeh. Momentum space calculations of the binding energies of argon dimer. *Intern. J. Quantum Chem.*, page e25807, 2018.

[182] A Owens and V Špirko. Universal behavior of diatomic halo states and the mass sensitivity of their properties. *Journal of Physics B: Atomic, Molecular and Optical Physics*, 52(2):025102, 2018.

[183] N. Doss, J. Tennyson, A. Saenz, and S. Jonsell. Molecular effects in investigations of tritium molecule beta decay endpoint experiments. *Phys. Rev. C*, 73:025502, 2006.

[184] M Čížek and J Horáček. Resonances in low-energy rare-gas atom scattering. *Czech. J.Phys.*, 46:55–65, 1996.

[185] C J Noble, M Dorr, and P G Burke. Multichannel resonances in complex energy R-matrix theory. *J. Phys. B: At. Mol. Opt. Phys.*, 26:2983, 1993.

[186] S Faas, J H Van Lenthe, and J G Snijders. Regular approximated scalar relativistic correlated ab initio schemes: applications to rare gas dimers. *Mol. Phys.*, 98:1467–1472, 2000.

[187] Peter Bingham. Private communications. 2019.

[188] KA Berrington. Low-energy electron excitation of the 3Pe fine-structure levels in atomic oxygen. *Journal of Physics B: Atomic, Molecular and Optical Physics*, 21(6):1083, 1988.

[189] John M Brown and Alan Carrington. *Rotational spectroscopy of diatomic molecules*. Cambridge University Press, 2003.

[190] Jinchun Xie and Richard N Zare. Selection rules for the photoionization of diatomic molecules. *J. Chem. Phys.*, 93:3033–3038, 1990.

[191] E Nikitin and R N Zare. Correlation diagrams for Hund's coupling cases in diatomic molecules with high rotational angular momentum. *Mol. Phys.*, 82:85–100, 1994.

[192] Hajime Katô. Energy levels and line intensities of diatomic molecules. Application to alkali metal molecules. *Bulletin Chem. Soc. Japan*, 66:3203–3234, 1993.

[193] L Veseth. Hund's coupling case (c) in diatomic molecules. I. Theory. *J. Phys.B: At. Mol. Phys.*, 6:1473, 1973.

[194] JM Brown, JT Hougen, K-P Huber, JWC Johns, I Kopp, H Lefebvre-Brion, AJ Merer, DA Ramsay, J Rostas, and RN Zare. The labeling of parity doublet levels in linear molecules. *J. Mol. Spectrosc.*, 55:500–503, 1975.

[195] Mats Larsson. Phase conventions for rotating diatomic molecules. *Physica Scripta*, 23:835, 1981.

[196] Richard N Zare. *Angular momentum: understanding spatial aspects in chemistry and physics*. Wiley-Interscience, 2013.

[197] Manuel Lara, P. G. Jambrina, F. J. Aoiz, and J. M. Launay. Cold and ultracold dynamics of the barrierless D+ + H-2 reaction: Quantum reactive calculations for similar to R-4 long range interaction potentials. *J. Chem. Phys.*, 143:204305, 2015.

[198] TS Monteiro and DR Flower. Excitation of [O I] and [C I] fine structure transitions by He and H_2: a neglected selection rule. *MNRAS*, 228(1):101–107, 1987.

[199] GJ Stacey, SD Smyers, NT Kurtz, and M Harwit. Observations of the 145.5 micron (OI) emission line in the Orion nebula. (NASA-TM-84307), 1982.

[200] Maximilian Beyer and Frédéric Merkt. Half-Collision Approach to Cold Chemistry: Shape Resonances, Elastic Scattering, and Radiative Association in the H++ H and D++ D Collision Systems. *Physical Review X*, 8(3):031085, 2018.

[201] Jeremy M Hutson. Coupled channel methods for solving the bound-state Schrödinger equation. *Comput. Phys. Commun.*, 84:1–18, 1994.

[202] Jeremy M Hutson and C Ruth Le Sueur. BOUND and FIELD: programs for calculating bound states of interacting pairs of atoms and molecules. *Computer Physics Communications*, 241:1–8, 2019.

[203] B. K. Sarpal, S. E. Branchett, J. Tennyson, and L. A. Morgan. Bound states using the R-matrix method: Rydberg states of HeH. *J. Phys. B: At. Mol. Opt. Phys.*, 24:3685–3699, 1991.

[204] D. A. Little and J. Tennyson. Singlet and triplet *ab initio* Rydberg states of N_2. *J. Phys. B: At. Mol. Opt. Phys.*, 46:145102, 2013.

[205] Z. Mašín, J. Benda, J. D. Gorfinkiel, A. G. Harvey, and J. Tennyson. UKRmol+: a suite for modelling of electronic processes in molecules interacting with electrons, positrons and photons using the R-matrix method. *Comput. Phys. Commun.*, 2019.

[206] Brianna R Heazlewood. Cold ion chemistry within Coulomb crystals. *Mol. Phys.*, pages 1–8, 2019.

[207] J. Tennyson and S. N. Yurchenko. The ExoMol atlas of molecular opacities. *Atoms*, 6:26, 2018.

[208] T. Rivlin, L. Lodi, S. N. Yurchenko, J. Tennyson, and R J Le Roy. ExoMol line lists X: The spectrum of sodium hydride. *MNRAS*, 451:5153–5157, 2015.